

ABSTRACT

Title of dissertation: A MULTISCALE MODEL
 FOR AN ATOMIC LAYER
 DEPOSITION PROCESS

Vivek Hari Dwivedi, Doctor of Philosophy, 2010

Dissertation directed by: Professor Raymond A. Adomaitis
 Department of Chemical Engineering

Atomic layer deposition (ALD) is a deposition technique suitable for the controlled growth of thin films. During ALD, precursor gasses are supplied to the reactor in an alternating sequence producing individual atomic layers through self-limiting reactions. Thin films are grown conformally with atomic layer control over surfaces with topographical features.

A very promising material system for ALD growth is aluminum oxide. Aluminum oxide is highly desirable for both its physical and electronic characteristics. Aluminum oxide has a very high band gap (~ 9 eV) and a high dielectric constant ($k \sim 9$). The choice of precursors for aluminum oxide atomic layer deposition vary from aluminum halide, alkyl, and alkoxides for aluminum-containing molecules; for oxygen-containing molecules choices include oxygen, water, hydrogen peroxide and ozone.

For this work a multiscale simulation is presented where aluminum oxide is deposited inside anodic aluminum oxide (AAO) pores for the purposes of tuning the

pore diameter. Controlling the pore diameter is an import step in the conversion of AAO into nanostructured catalytic membranes (NCM). Shrinking the pore size to a desired radius allows for the control of the residence time for molecules entering the pore and a method for molecular filtration. Furthermore pore diameter control would allow for the optimization of precursor doses making this a green process. Inherently, the ALD of AAO is characterized by a slow and a faster time scale where film growth is on the order of minutes and hours and surface reactions are near instantaneous. Likewise there are two length scales: film thickness and composition on the order of nanometers and pore length on the order of microns. The surface growth is modeled in terms of a lattice Monte Carlo simulation while the diffusion of the precursor gas along the length of the pore is modeled as a Knudsen diffusion based transport model.

A Multiscale Model for an Atomic Layer Deposition Process

by

Vivek Hari Dwivedi

Dissertation submitted to the Faculty of the Graduate School of the
University of Maryland, College Park in partial fulfillment
of the requirements for the degree of
Doctor of Philosophy
2010

Advisory Committee:

Professor Raymond A. Adomaitis, Chair/Advisor

Professor Sheryl Ehrman

Professor Panagiotis Dimitrakopoulos

Professor Jeffery Klauda

Professor Gary Rubloff

© Copyright by
Vivek Hari Dwivedi
2010

Table of Contents

List of Figures	v
1 Introduction	1
1.1 Outline of Thesis	3
List of Abbreviations	1
2 A Review of Atomic Layer Deposition	4
2.1 Overview	4
2.2 Thin Film Deposition: CVD and ALD	4
2.3 CVD	5
2.4 ALD Overview	8
2.5 Fundamental ALD Process	8
2.5.1 Benefits of ALD	10
2.5.2 Limitations of ALD	10
2.6 Review of ALD Applications	12
2.6.1 Microelectronics	12
2.6.2 Magnetic Heads	13
2.6.3 Thin Film Electroluminescent Displays	13
2.6.4 Protective Coatings	14
2.6.5 Optics	15
2.6.6 Next Generation Catalysts	15
2.7 ALD Reactors	16
2.7.1 Flow Reactor - Figure [2.3 A.]	16
2.7.2 Singular Overhead Injector - Figure [2.3 B.]	16
2.7.3 Shower Head - Figure [2.3 C.]	17
2.7.4 Batch Array - Figure [2.3 D.]	17
2.8 ALD and Anodic Aluminum Oxide	17
2.8.1 Fabrication Process	19
2.8.2 AAO Applications	20
3 ALD Chemistries	22
3.1 Overview	22
3.2 ALD Precursors	22
3.3 TMA and Water ALD	25
3.4 Structure of TMA	28
3.5 Overview of Surface Reactions	32
3.6 Saturation Issues in ALD	33
3.7 Properties of Al_2O_3 Thin Films	36
3.8 Experimental Verification of Surface Reaction for TMA and Water . .	37
3.8.1 Thermal Studies	38
3.8.2 Water Exposure	38
3.8.3 TMA Exposure With Ligand Exchange Reactions	40

3.8.4	TMA Exposure With Dissociation Reactions	43
3.8.5	Methylated and Hydroxylated Half Reactions	44
3.9	Transition State Theory	44
3.10	Mass Balance Approach for Surface Species Statistics	50
3.11	Graph Based Data Structures	52
4	Modeling Surface Structures	54
4.1	Overview	54
4.2	Review of Atomistic Scale Simulations for Thin Film Processing	54
4.2.1	Density Functional Theory	55
4.2.2	Mean Field Approximations	56
4.2.3	Molecular Dynamics Simulations	56
4.2.4	Chapman-Kolmogorov Equation	57
4.3	Novel Computational Method for Surface Description	59
4.4	KMC Overview with Elementary Example	59
4.5	Poisson Distribution	61
4.6	Kinetic Monte Carlo Example	62
4.7	The Lattice	64
4.7.0.1	Species occupying the lattice sites	66
4.7.1	TMA reactions on the lattice	68
4.7.1.1	Ligand exchange reactions	68
4.7.1.2	Dissociation reactions	70
4.7.2	Water reaction	70
4.7.3	Monte Carlo simulation procedure	70
4.7.4	The MC algorithm	72
4.7.5	Initial film growth	74
4.7.5.1	Initial TMA exposure	76
4.7.5.2	Water exposure	78
4.8	Film growth under iterated cycles	79
4.8.1	GPC and other film growth measures	79
4.8.2	Representative film growth	82
4.8.3	Influence of ϕ	85
4.8.4	Sub-saturation experiments	87
4.8.5	Stability of the ALD growth process	89
5	Pore Transport	91
5.1	Overview	91
5.2	Knudsen Number	94
5.3	Wall Collision Number	96
5.4	Wall Collision Number of TMA and Water	102
5.5	Distribution of Molecules Post Collision	102
5.5.1	Macrostates and Microstates	103
5.5.2	Second Law of Thermodynamics	104
5.5.3	Detailed Balance	105
5.5.4	Second Derivation of Cosine Distribution	107

5.6	Flux Derivation	110
5.7	Knudsen Diffusion	113
5.8	Review of Knudsen Transport Models	115
5.8.1	Knudsen, Smoluchowski and Dushman	116
5.8.2	Clousing Integral	118
5.8.3	Random Billiard Model	119
5.8.4	KTRM	120
5.8.5	BTRM	120
5.8.6	Novel Approach for Determining Transmission Probability . .	121
5.9	Method of Weighted Residuals	122
6	Results and Conclusions	125
6.1	Overview	125
6.1.1	Recipe 1	127
6.1.2	Recipe 2	128
6.1.3	Recipe 3	130
6.1.4	Recipe 4	131
6.1.5	Recipe 5	132
6.1.6	Recipe 6	134
6.1.7	Collocation Points	135
7	Summery of Dissertation	144
7	Future Work	147
	Bibliography	148

List of Figures

2.1	CVD Reactor Schematic	7
2.2	ALD Process Steps	9
2.3	ALD Reactor Types	18
2.4	Formation of Nanotubes [1]	20
2.5	Nanostructured Catalytic Membranes	21
3.1	A. Structure of monomer TMA. B. Structure of dimer TMA where the dotted red line is the center of symmetry	29
3.2	Graph of Monomer Mole Fraction, x_M , as a function of temperature using simulation based value for monomer, dimer equilibrium constant, K_d . The green dot represents the reaction condition for this work, clearly showing the existence of only the monomeric structure.	31
3.3	Cartoon illustrating the three different ALD mechanisms: A. Ligand Exchange B. Dissociation C. Association	34
3.4	Factors that lead to less than a monolayer of growth per cycle.	36
3.5	Thermal studies from [22] showing infrared absorbances in the hydroxide and methyl stretching regions versus TMA and water exposures at two different temperatures, 300 and 500 K.	39
3.6	Water deposition studies from [22] showing A. absorbances of porous alumina versus 0.01 water exposure at 500 K. B. Normalized integrated absorbances of OH and CH ₃	40
3.7	TMA deposition studies from [22] showing A. absorbances of porous alumina versus 0.01 TAM exposure at 500 K. B. Normalized integrated absorbances of OH and CH ₃	41
3.8	A series of ligand exchange reactions resulting in tent-like structure	43
3.9	TMA and water deposition studies from [22] showing the teetering between hydroxylated surface and methylated surface	45
3.10	DFT studies by [100] showing the progression of either A. TMA and hydroxide group forming methane and surface methyl group via transition state theory and B. Water and surface methyl group forming methane and surface hydroxyl group via transition state theory.	48
4.1	Simple KMC Flow Process	63
4.2	The 2-dimensional lattice structure developed to represent the structure of ALD Al ₂ O ₃ films.	66
4.3	<i>Initial growth surface (top), after TMA exposure (middle), and then water (bottom).</i>	67
4.4	<i>TMA (R1-R4) and water (R5) reactions and their representations on the lattice.</i>	71
4.5	<i>Sequence of surface reactions taking place during the TMA exposure leading to the surface shown in Fig. 4.3, middle. Index j indicates the iteration number in the Monte Carlo simulation procedure.</i>	76

4.6	<i>Our simulation results compared to data taken from Figs. 5 and 7 of [22].</i>	77
4.7	<i>Extent of reaction at 0.5 Torr exposure of TMA and water.</i>	80
4.8	<i>Representative film after 250 full ALD cycles; in both the full-scale and magnified portion, the cyan line indicates the mean film thickness T^{250} and the red lines indicate the surface roughness as $T^{250} \pm \sigma$.</i>	82
4.9	<i>ALD film properties as a function of exposure cycle number.</i>	83
4.10	<i>Histogram of the frequency of each reaction in the overall deposition process.</i>	86
4.11	<i>A section of highly porous film that results for $\phi = 0.05$ (R2 favored over R1) and after 250 ALD cycles.</i>	87
4.12	<i>Surface roughness as a function of cycle number illustrating the dependence on M. For all cases $\delta_A = 5$ and $\delta_W = 2.5$, and each curve is the average of 100 simulations.</i>	90
5.1	Early observation of distribution of filament vaporization	93
5.2	Modeling approach for different Knudsen Numbers [78]	96
5.3	Detailed balance using Knudsen argument [99]	106
5.4	Second argument for Cosine Distribution	109
5.5	Differential Volume	111
5.6	Constituent nanopore with dimensionless axial coordinates	114
5.7	Random Billiard Description	120
5.8	Schematic for Determining $q(s, s')$	122
6.1	The Initial Pore	126
6.2	Right pore mouth exposed	127
6.3	Left pore mouth exposed	129
6.4	Left pore mouth exposed	130
6.5	TMA exposed to right and water left	131
6.6	TMA exposed to right and water left	133
6.7	Sequential exposure	134
6.8	Recipe 6 at 5 collocation points	136
6.9	Recipe 6 at 10 collocation points	137
6.10	Recipe 6 at 15 collocation points	138
6.11	Recipe 3 at 5 collocation points and 10 runs	139
6.12	Recipe 3 at 10 collocation points and 10 runs	140
6.13	Recipe 3 at 20 collocation points and 10 runs	141
6.14	TMA exposure over 5 collocation points after 10 runs.	142
6.15	TMA exposure over 10 collocation points after 10 runs.	142
6.16	TMA exposure over 15 collocation points after 10 runs.	143

Chapter 1

Introduction

For many thin film applications, the method of deposition is important in determining the quality and property of the film. The deposition process must be cost-efficient and be capable of shifting from bench-scale production to industrial large-scale production. Two particular methods for thin film production, Chemical Vapor Deposition (CVD) and Atomic Layer Deposition (ALD), have been applied in various thin film fabrication processes with success. In chemical vapor deposition, dense films with excellent uniformity over large areas and over complex geometries can be deposited over broad temperature and pressure ranges. In atomic layer deposition, thickness and composition can be controlled down to the atomic level. Atomic Layer Deposition (ALD) was invented in 1977 by [91], and is a modified version of the chemical vapor deposition technique. Unlike the CVD process where deposition is done in a steady-state flow situation, ALD uses discrete steps to control the surface reaction and film thickness.

A novel application in the use of ALD is for the control of pore diameters in high aspect ratio nanopores. Aluminum forms a porous oxide called anodic aluminum oxide (AAO) when anodized in an acidic electrolyte. The property of AAO that is the most relevant is that the pores are very uniform in both pore length and pore diameter and are arranged in an hexagonal pattern. The pores are al-

most parallel and can either be open at one end or opened at both ends [20]. AAO has many applications ranging from energy storage, filtration and as next generation catalysts where AAO is used as a scaffold for the creation of nanostructured catalytic membranes (NCM). Nanostructured catalytic membranes (NCM) has garnered much academic research due to its advantages over typical reactor designs. The NCM combines two processes, chemical reaction and the separation of the resulting product simultaneously thus reducing the overall size of the typical catalytic reactor and the cost of operations [15].

Modeling ALD gas surface reactions range from *ab initio* quantum dynamic simulations to molecular dynamics simulations typically preferred by theoretical chemists. From a modeling point of view, considerable effort has been put into understanding high-*k* materials. There are several methods available that model surface morphologies including: first principle approach in calculating reaction pathways, mean field approximations in describing thin film morphologies based on nucleation theory, molecular dynamics simulations to describe the diffusion of molecules on a substrate, Chapman-Kolmogorov equation and Monte Carlo methods describing thin film properties per cycle. The main computational contribution of this paper is to define a numerical representation of ALD films by approximating the film's true molecular structure on a 2D lattice. We see our approach as a method of *coarse graining* the potentially complex nature of the films, limiting the number of degrees of freedom to a more manageable level of computational complexity. While our lattice representation only approximates the spatial relationships of atoms in the film, it will give useful information about the film structure and will rigorously

keep track of bonds between atoms. Because this lattice-based representation of film structure will be capable of describing crystalline through amorphous films, we will examine the evolution of ALD film characteristics, grown on a crystalline Al_2O_3 substrate, to examine how the film structure and composition evolve with ALD cycle number.

In addition to conformal films interesting pore shapes can be created by novel methods of separating the precursors by introducing the first precursor at one opening and the other precursor at the other opening.

1.1 Outline of Thesis

This work begins by reviewing the atomic layer deposition process its advantages and limitations and the current industrial uses and types of reactors. The next chapter is dedicated to a review of ALD chemistries from reaction theory to precursor choices followed by the ALD chemistries of TMA and water and their structures. Saturation issues as function of steric effects is reviewed followed by the properties of aluminum oxide films. A review of experimental literature data and density functional theory and a overall mass balance approach to garner surface statistics is discussed. The next chapter focuses on the methods for the modeling of gas surface reactions which is followed by a novel lattice based Monte Carlo modeling technique. The next chapter discusses the pore transport model and its derivation followed by a review of other modeling methods. The last chapter discusses the multiscale results.

Chapter 2

A Review of Atomic Layer Deposition

2.1 Overview

This chapter provides the two fundamental processes for thin film deposition that are used in industry and academia chemical vapor deposition, CVD, and atomic layer deposition, ALD. An overview of advantages and disadvantages of ALD is given followed by industrial applications for ALD. The final section is dedicated to the formation of anodic aluminum oxide nanopores that are used as templates and scaffolds specifically for the formation of nanotubes and nanostructured catalytic membranes which utilize ALD for their modifications.

2.2 Thin Film Deposition: CVD and ALD

Thin film deposition is a manufacturing process where precursor materials are delivered to a substrate surface, attach and form a solid material layer [40]. The thickness of this layer can range from a few atomic layers to several micrometers. Thin film deposition is important in many applications including integrated circuits, microfluidic devices, coating applications and solar cells [85].

For many thin film applications, the method of deposition is important in determining the quality and property of the film. The deposition process must be

cost-efficient and be capable of shifting from bench-scale production to industrial large-scale production. Two particular methods for thin film production, Chemical Vapor Deposition (CVD) and Atomic Layer Deposition (ALD), have been applied in various thin film fabrication processes with success. In chemical vapor deposition, dense films with excellent uniformity over large areas and over complex geometries can be deposited over broad temperature and pressure ranges. In atomic layer deposition, thickness and composition can be controlled down to the atomic level. ALD was invented in 1977 by [91], and is a modified version of the chemical vapor deposition technique. Unlike the CVD process where deposition is done in a steady-state flow situation, ALD uses discrete steps to control the surface reaction and film thickness.

2.3 CVD

Chemical Vapor Deposition is the predecessor for ALD. It is therefore important to discuss the CVD process in order to gain a better understanding of the advantages of ALD. CVD is widely used as a means of depositing films for applications ranging from superconductors to ferroelectric films to hard coatings [10]. The name itself implies the formation of solid material from the gas state by way of a chemical reaction [90]. A CVD reactor typically consists of the following parts: feed and source lines for precursor gasses, mass flow controllers, the reaction chamber (reactor), heat source for the substrate, and temperature sensors Figure 2.1. The deposition for chemical vapor deposition can be described through the following

steps [38]

1. Reactant transport to substrate surface
2. Reactant adsorption on surface
3. Reactant surface diffusion
4. Incorporation of adsorbed species into the growing film
5. Chemical reaction product desorption
6. Diffusion of reaction products away from surface
7. Removal of reaction product and unreacted reactant

The variables which affect the film properties and deposition rate, are a function of the following experimental parameters:

1. Reactor geometry
2. Surface properties
3. Pressure
4. Substrate temperature
5. Gas flow rates
6. Reactant ratios
7. Purity of reactants

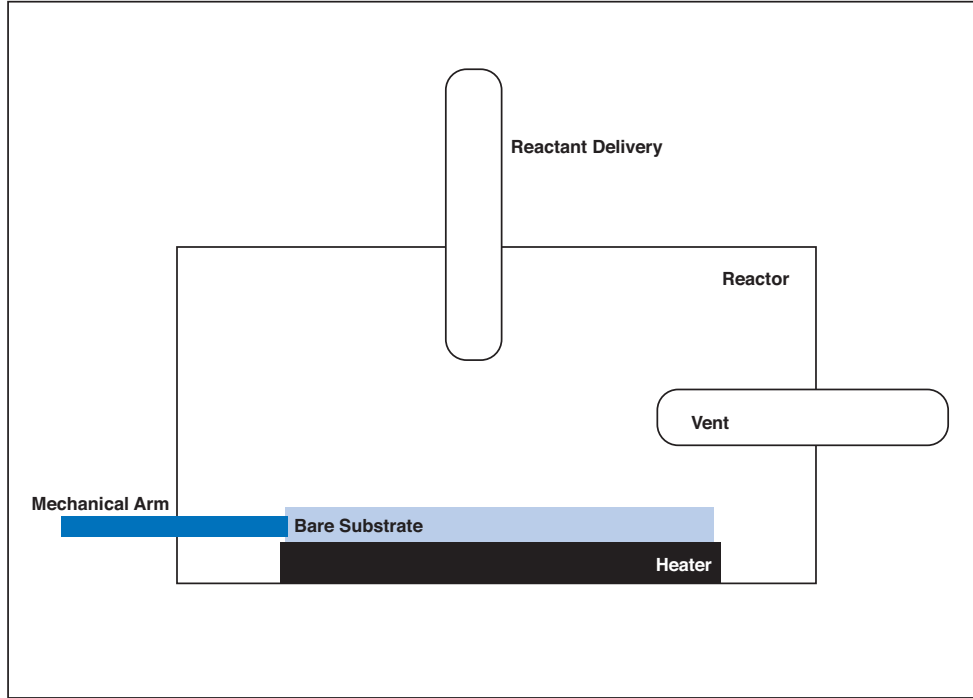


Figure 2.1: CVD Reactor Schematic

In general, CVD results in high deposition rates and is suitable for industrial scale production. However, if the experimental parameters have not been optimized, undesirable reactions can take place in the gas phase. These gas phase reactions are known as homogeneous reactions as compared to heterogeneous reactions which occur on the surface. These homogenous reactions result in the formation of particles that precipitate onto the substrate or growing film. Particle formation may result in poor adhesion of the film or the destruction of microelectronic devices [88]. Other problems with CVD type of reactors is that a constant flux of gasses is required making the use of solid sources difficult [70].

2.4 ALD Overview

Atomic Layer Deposition (ALD) is a thin film deposition process in which the growth surface is exposed to reactive precursor gases in an alternating fashion. A characteristic of the surface adsorption and reaction mechanisms is that they are normally self-limiting, allowing for atomically accurate control of film thickness and uniform deposition over complex surface topographies.

2.5 Fundamental ALD Process

The ALD process has the following steps Figure [2.2] [79, 58, 88]:

1. Figure [2.2 A] Precursor gas is pumped into a chamber containing a substrate.
2. Figure [2.2 B] Precursor gas chemisorbs on a substrate active site.
3. Figure [2.2 C] After a certain residence time the excess of the reactant precursor, which is in the gas phase or has been physisorbed on the reactor chamber walls or on the substrate, is pumped out the chamber with the aid of an inert gas.
4. Figure [2.2 D] A distinct second precursor then is pumped into the reactor chamber where it chemisorbs and undergoes an exchange reaction with the first reactant on the substrate.
5. Figure [2.2 E] This second reactant pulse results in the formation of a solid thin film and a second inert gas purge removes any excess gas from the chamber.

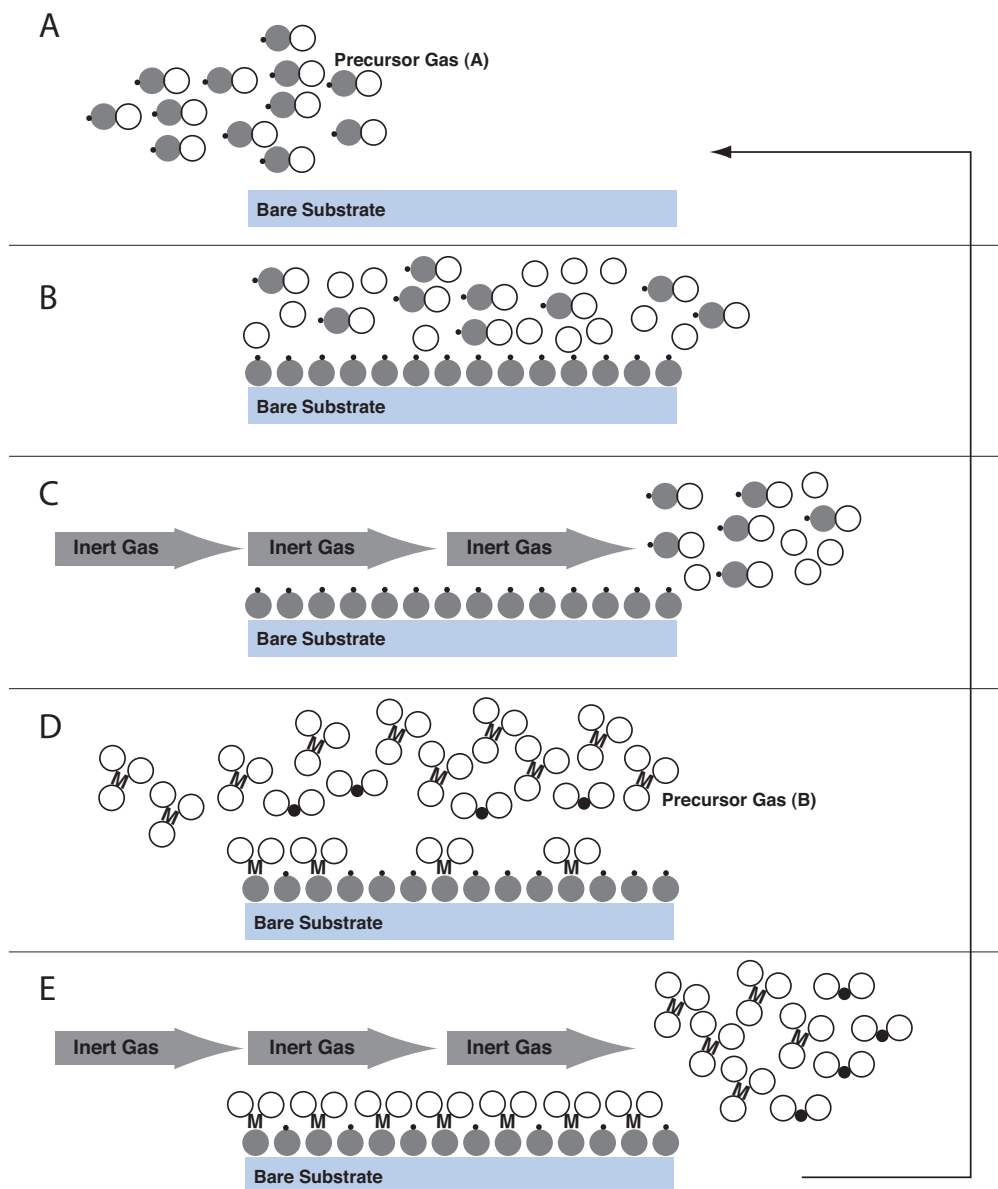


Figure 2.2: ALD Process Steps

By repeating this cycle, a controlled layer-by-layer growth is achieved. The inert gas that is pumped into the reactor between the precursor materials not only provides a separation between the precursors but also acts as a cleaning agent. This cleaning agent is important because gas-phase reactions between source materials are undesired [88].

2.5.1 Benefits of ALD

The self-limiting nature of ALD is a function of the precursor dose. Surface reactions will proceed if there is a high enough precursor concentration to saturate the substrate, once this saturation is achieved the gas surface reaction terminates. Thus at this saturation limit or beyond a homogenous film is deposited on all surfaces leading to some practical advantages:[81]

1. Excellent conformality and uniformity over large areas and batches
2. Accurate film thickness control as a function of the number of repeated deposition cycles.
3. Film composition can be changed by replacing the precursors dosed into the reactor thus allowing for the creation of multilayer or multicomponent films

2.5.2 Limitations of ALD

Though ALD may seem like an ideal process for thin film development several disadvantages exist [81]:

1. The separation of precursors and the introduction of the purge steps results in low deposition rates around the order of $100nm/h$.
2. There are limited material selections for ALD precursors and processes for important materials as related to the semiconductor industry and beyond such as silicon, germanium, metal silicides and multicomponent oxide ferroelectrics.
3. ALD's chemical nature can result in impurities left in the film, typically from unreacted surface oxides, on the order of a few percentages.

However; in spite of these limitations, the ALD process allows for large batch processing capabilities to offset the low deposition rate, an increase in effort has been underway for several years in conducting research in new precursor systems and the films created still show good material properties regardless of the increase in film impurities.

ALD is an inherently dynamic process characterized by multiple time scales: a faster time scale corresponding to the molecular events taking place during each exposure cycle, and the slower changes that take place in overall deposition rate from cycle to cycle [44]. Likewise, multiple length scales are found in these systems where macroscopic length scales (100s of μm) correspond to gas phase transport effects, and microscopic scales characterize the atomistic nature of the lm growth.

Reaction chemistry, stoichiometry, and kinetics all factor into successful saturation coverage in ALD processes [43]. In ALD, both reactions must be fast and irreversible, homogenous reactions must not occur, and both reactants must undergo a self-limiting reaction with the product of the previous reactant on the surface of

the substrate. Physisorption is not allowed and the reactants and by-products must be sufficiently volatile at the deposition temperature. Regarding ALD stoichiometry, a proper amount of reactant must be supplied so that a stoichmetric amount of material is available for deposition over the entire surface. Transport phenomena in ALD processes is important for complex geometries. For example, if ALD is used in holes or cavities, a long enough exposure of reactant must be present at the entrance of the cavity to saturate the entire surface area of the geometry.

2.6 Review of ALD Applications

The industrial applications of ALD can be classified into the following categories: microelectronics, magnetic heads, thin film electroluminescent displays, protective coatings, optics and next generation catalysts. We provide a few brief examples below:

2.6.1 Microelectronics

ALD microelectronics product applications include gate stacks, capacitors, interconnects and non-semiconductor applications. A gate stack is a transistor element in which a circuit can be turned on or off by applying a voltage. Traditional gate stack materials include silicon dioxide and silicon nitride. These materials no longer meet the challenge of advanced ultra large-scale integrated circuits and new promising materials include zirconium oxide and hafnium oxide, which can be made small enough to fit on the large-scale integrated circuit by ALD. The function of

a capacitor is store charge and memory chip manufacturers continue to strive for reducing the size of capacitors while ensuring that capacitors and nearby transistors are adequately isolated from each other. As chip real estate decreases smaller capacitors with high dielectric constants must be created. To create smaller and smaller capacitors, ALD of aluminum oxide is promising. ALD, is the key enabling technology in Intels current 45nm transistor manufacturing process to deposit the HfO₂ gate oxide [12]. Furthermore, research is underway in the deposition of gate dielectrics for carbon nanotube transistors [49].

2.6.2 Magnetic Heads

Magnetic heads are used to read and write data onto hard disks [81], they move above a disc platter transforming the platters magnetic field into an electrical current to read the disc or they transform the electrical current into a magnetic field to write to the disk. Due to aggressive downsizing the deposition process of choice in head creation had been sputtering methods which had its limitations, currently new technology allows for the ALD of nanolaminating and mixing aluminum oxide and silicon oxide to create the head.

2.6.3 Thin Film Electroluminescent Displays

Thin film electroluminescent displays (TFEL) are high operating voltage and rugged displays where a material emits light in response to an electric current or a strong electric field. Electroluminescent displays are similar to the operation of a

laser where a photon is emitted by the return of an excited substance to its ground state [2]. An example of a electroluminescent device is a light emitting diode LED. Layers of specialized materials are used in constructing the TFEL [81]. Starting from the bottom these layers include:

1. A rigid insulating baseplate such as glass
2. A protective layer
3. Transparent electrodes
4. Insulating layer
5. Luminescent layer
6. Metal electrodes
7. Passivation layer
8. Black or transparent background

ALD is typically used for the construction of the luminescent layer, the insulators, the passivation and protective layers where each layer has a thickness on the order of $200nm$. These devices are typically used in the medical industry and in military operations.

2.6.4 Protective Coatings

The high uniformity of ALD provides an efficient technique in sealing substrates of random three dimensional topographies. An example of utilizing this

technique has been the use of aluminum oxide as an effective barrier in preventing the tarnish of silver [87]. By utilizing the efficient batch processing capabilities of ALD entire collections of silver based materials can be coated at the same time.

2.6.5 Optics

High uniformity and precise thickness control make ALD an attractive process for the creation of novel optical devices [59]. As an example, infrared cutfilters were created by using ALD to manufacture multilayer stacks.

2.6.6 Next Generation Catalysts

The focus of this thesis is centered on the use of ALD to control the pore sizes of anodic aluminum oxide membranes, AAO. ALD's atomic layer growth allows the control of pore sizes of high aspect ratio pore where typically the pore diameter is in range of 20 to 100nm's

Other applications for ALD include next generation solar cells of germanium deposited onto nanostructured silicon substrate. Nano glue, where ALD can be used to glue small wires, particles and micron sized objects together and coating medical instruments with biocompatible coatings pacemakers and stents. ALD has even greater potential in future manufacturing and research applications, such as, nanoelectrodes for studying single molecules [45], and other nanoparticle [53] and nanolaminate [50] applications.

2.7 ALD Reactors

In general there are 4 types of ALD reactor configurations that are used in industry and academia Figure [2.3]: cross flow reactors, singular overhead injector, shower head and batch array [44].

2.7.1 Flow Reactor - Figure [2.3 A.]

Cross flow reactors are single-wafer systems where precursor gas flows across the substrate of choice. These types of reactors are also called wave-type reactors. The dynamics of the reactor exposes the substrate separately where the leading edge is exposed first and the trailing edge is exposed last. Problems with this type of reactor are based on the concentration of precursor gas. If the gas concentration is low and as the deposition is transversing across the substrate the trailing edge may not undergo a gas surface reaction due to a lack of gas phase species. This type of reactor is useful during ALD of cylindrical pores as the "precursor wave" transverses through the pore.

2.7.2 Singular Overhead Injector - Figure [2.3 B.]

A single overhead reactor has a gas inlet above the deposition substrate where the substrate is uniformly exposed to precursor. Issues with this type of reactor include areas of stagnant gas within the chamber where purge times may be longer to remove all the gas.

2.7.3 Shower Head - Figure [2.3 C.]

A shower head style reactor is where there are multiple inlet gas streams above the deposition chamber. The advantages of this type of reactor is that all parts of the substrate are concurrently and constantly exposed to virginal gas. Disadvantages of this type of reactor are the same as the singular overhead injector.

2.7.4 Batch Array - Figure [2.3 D.]

ALD is inherently a slow process in order to create multiple deposition substrates a batch array ALD reactor is used. Gas is introduced through a single point above the reactor and purged below the reactor. Multiple substrates are plated one on top of each other with a minimal spacing allowing precursor species to react through diffusion.

2.8 ALD and Anodic Aluminum Oxide

A novel application in the use of ALD is for the control of pore diameters in high aspect ratio nanopores. Aluminum forms a porous oxide called anodic aluminum oxide (AAO) when anodized in an acidic electrolyte. The most relevant property of AAO is that the pores are very uniform in both pore length and pore diameter and are arranged in an hexagonal pattern. The pores are almost parallel and can either be open at one end or opened at both ends [20].

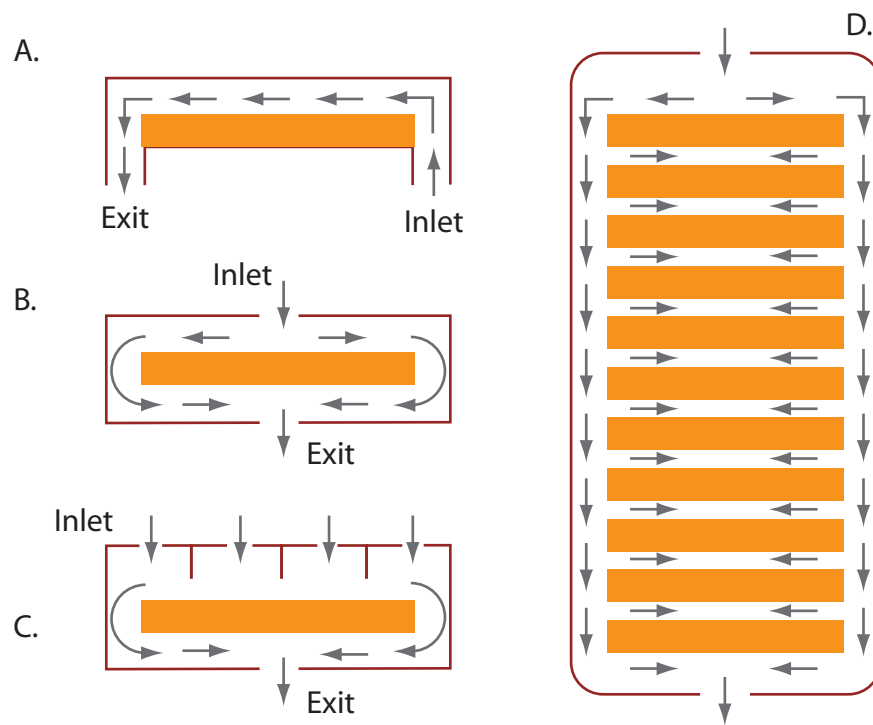


Figure 2.3: ALD Reactor Types

2.8.1 Fabrication Process

The fabrication process for creating AAO with $15nm$ diameters as described by [3], [4] include the following steps:

1. 99.99% Al foil substrate is degreased in acetone and then polished in a solution consisting of perchloric acid:EtOH.
2. The foil is anodically oxidized in a $0.3M$ oxalic acid solution at a $40V$ potential for 15 hours.
3. The film is removed by immersing the substrate in phosphoric and chromic acid.
4. A second anodization is carried out at the same conditions as the first for 24 hours.
5. The unreacted Al foil is removed and the membrane is released using a copper chloride hydrochloric acid solution.

The above process creates a single opening pore where the bottom of the pore is covered by a thin oxide film. To create a pore open at both ends the membrane is immersed in phosphoric acid resulting in membranes on the order of 70 microns thick. The pore diameter, D_{pore} , and density, ρ_{pore} , is a function of the anodizing voltage, V and can be determined as:

$$\rho_{pore} = \frac{\alpha}{(D_{pore} + \beta V)^2} \quad (2.1)$$

2.8.2 AAO Applications

There are many industrial applications that use AAO [4], these include scaffold platform for nanofabrications, nanomasks, information storage, catalysis and template structures for the fabrication of nanowires, nanotubes etc. The use of atomic layer deposition as a process to modify the AAO structures can be readily seen in the last two industrial applications mentioned, template structures and catalysis. The process of creating nanotubes, Figure [2.4], begins by creating a single mouth AAO membrane using the steps mentioned above Figure [2.4 A]. Applying the ALD process, material is deposited inside the membrane until the desired thickness is achieved Figure [2.4 B]. If desired the AAO membrane is etched away to release the ALD nanotube Figure [2.4 C]. An example of a material system is the fabrication of hafnium oxide high- κ dielectrics in the size range of $20 - 300nm$ in diameter [1]. The use of AAO as a scaffold for the creation of nanostructured catalytic mem-

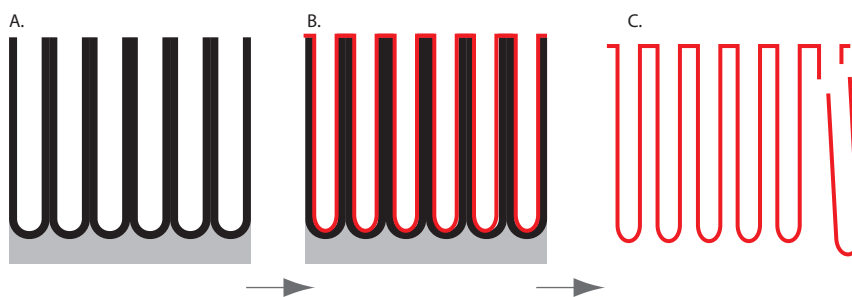


Figure 2.4: Formation of Nanotubes [1]

branes (NCM) has garnered much academic research due to its advantages over typical reactor designs. The NCM combines two processes, chemical reaction and the separation of the resulting product simultaneously thus reducing the overall size

of the typical catalytic reactor and the cost of operations [15]. The NCM is created by first producing a two mouth AAO where atomic layer deposition is utilized to tune the pore diameter in order to control the residence time for the reactant and to provide filtration capabilities this is followed by the deposition of the catalytic support and the deposition of the catalyst layer. A typical NCM material map can be considered as follows: the pore size is reduced by the ALD of aluminum oxide, the catalytic support is created by the ALD of titanium oxide and the catalyst layer is formed by the ALD of vanadium oxide. The process is summarized in Figure [2.5] [5].

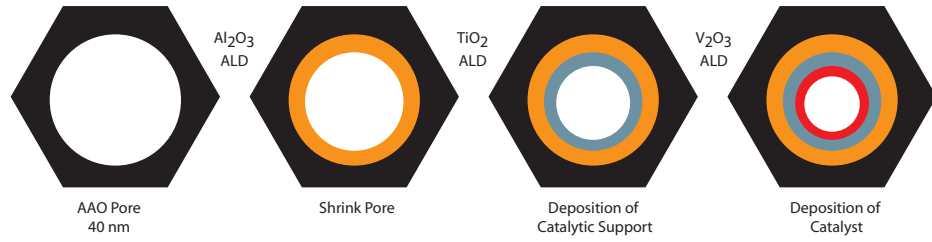


Figure 2.5: Nanostructured Catalytic Membranes

Chapter 3

ALD Chemistries

3.1 Overview

In this chapter we present a review of atomic layer deposition growth chemistries with a specific interest in the chemistries of aluminum oxide. This chapter is arranged by first giving an overview of the different properties of a successful ALD precursor followed by a discussion of the Al_2O_3 precursor pair, trimethyl aluminum, TMA, and water. We then discuss the structure of TMA as it exists as both a dimer and monomer in equilibrium. The different surface reaction mechanisms is reviewed followed by non-ideality issues that lead to percentage monolayer growth. The characterization of Al_2O_3 and the justifications for surface reactions are given through experimental work as cited in literature followed by a review of transition state theory. A mass balance approach is then used to determine surface specie statistics which is followed by discussing graph based data structures which allows for book keeping of the various surface reactions and species.

3.2 ALD Precursors

As mentioned ALD possesses many important properties that make it a desirable application for achieving highly conformal films on varying topographies and

high aspect ratio geometries. Its application is based on separating precursor gases to achieve precise thickness control by gas surface reactions. It is therefore important to discuss the specific properties of precursors to achieve suitable deposition [68].

For the deposition of metal oxides such as Al_2O_3 , the precursors are distinguished as either metal sources or oxygen sources. The metal precursor can be grouped into inorganic sources and metalorganic sources. Metalorganics reactants can be further subdivided into two groups, the first are called organometalics, where the metal atoms is directly bounded to a carbon atom. The second metalorganic group consists of species where there is no direct metal carbon bond.

The typical nomenclature for metal precursors is, ML_n where the metal atom, M is bounded to n number of ligands, L . The characterization of the ligand can determine many important properties of the ALD system being studied including the quality of the deposited film. As an example let us consider a ligand halide such as chlorine in the growth of hafnium oxide, HfO_2 thin films. When growing hafnium oxide the hafnium contributing precursor is $HfCl_4$ and the oxygen contributing precursor is water. This ALD precursor system has a particularly negative property, the metal chloride bond is a strong bond resulting in a high activation barrier and high ALD operating temperature. High ALD temperatures typically result in low growth rates per cycle due to the reduction of active hydroxide surface sites. Furthermore, the by product of the hafnium chloride/hydroxylated surface reaction is hydrochloric acid, that when released impacts the quality of the deposited film by etching it. In addition to film degradation, hydrochloric acid impacts the ALD re-

actor by corroding the substrate chamber. Other ligands that are typically used for metal oxide ALD include alkoxides, β -diketonates, alkylamides, amidinates, alykyls and cyclopentadienyls.

In general, there are several important and ideal attributes for ALD precursors:

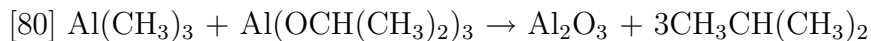
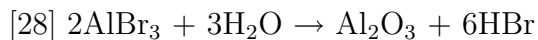
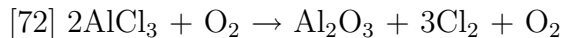
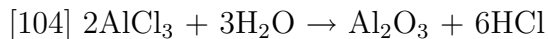
1. Sufficient volatility.
2. Rapid vaporization at a reproducible rate.
3. Self-reactions between volatile byproducts and unreacted gas phase precursor species do not occur.
4. No molecular decomposition in the gas phase or on the surface.
5. Precursors must have a high reactivity towards the precursor attached to the surface. Resulting in fast kinetics which leads to lower operating temperatures.
6. Resulting byproducts from precursor surface reactions must be sufficiently volatile allowing for purging.
7. Byproducts must be benign to the deposited film and reactor. Corrosive byproducts result in film etching and corrosion of the reactor giving nonuniform films.
8. Precursors must react with their associated precursor surface products exothermically. A large thermodynamic driving force allows for a low deposition temperature producing smooth amorphous films.
9. Metal ligand bonds must be sufficiently strong for precursor stability.

10. Ligands should not be too bulky or too big. Bulky ligands lower precursor volatility and shield the center metal atom from bonding to surface sites. We shall see that this particular condition though ideal is most likely unavoidable.

3.3 TMA and Water ALD

The focus of this work is the study of aluminum oxide there are many precursors that can be used for Al_2O_3 ALD. We give a brief review of different aluminum sources and oxygen sources through several full reactions and a table describing other aluminum and oxygen source below [75]. A description of the TMA/water process that is the precursor of choice for this work is also provided.

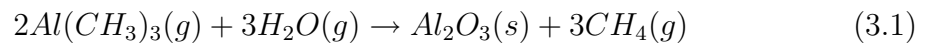
Full reactions that produce aluminum oxide films include:



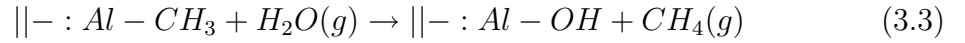
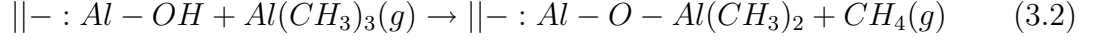
Other precursor combinations that produce aluminum oxide films include:

Al Source	O ₂ Source	Ref.
AlCl ₃	CH ₃ OH	[33]
AlCl ₃	Al(OCH ₂ CH ₃) ₃	[73]
Al(CH ₃) ₃	H ₂ O ₂	[56]
Al(CH ₃) ₃	O ₃	[29]
Al(CH ₃) ₃	O ₂	[61]
Al(CH ₃) ₃	N ₂ O	[46]
Al(CH ₃) ₃	NO ₂	[95]
Al(CH ₃) ₃	N ₂ O ₄	[36]
Al(CH ₃) ₃	OHC ₃ H ₇	[101]
Al(CH ₃) ₃	Al(OCH ₂ CH ₃) ₃	[80]
Al(CH ₃) ₂ OCH ₂ CH ₃	H ₂ O	[102]
Al(C ₂ H ₅) ₃	H ₂ O	[48]
Al(OC ₂ H ₅) ₃	H ₂ O	[48]
Al(OC ₂ H ₅) ₃	O ₂	[31]
Al(OCH ₂ CH ₃) ₃	H ₂ O	[31]
Al(OCH ₂ CH ₃) ₃	O ₂	[31]

The overall TMA and water process follows the following stoichiometry:



The above equation can be written as two successive half reactions representing the aluminum source gas-solid chemistries and the oxygen source gas-solid chemistries:



In the above reactions, the $||- :$ species represent active surface sites that have a potential to react with a complementary gas phase molecule. In the first half reaction the surface hydroxide group reacts with a single TMA molecule to produce a new surface group comprising of two methyl ligands and methane gas. The second half reaction describes the reaction of a single water molecule that reacts with a single surface methyl group to create the original hydroxide surface group. Therefore, each of the half reactions represent the surface state of the substrate as it teeters between a hydroxide state and a methylated state. For the study of aluminum oxide films there are many paired precursors that can be used as mentioned in the above table, however the $Al(CH_3)_3$ and H_2O pair represent an ALD system that is close to ideal due to the following reasons [75]:

- A vast amount of research has been conducted and published on the TMA and water ALD system see for example [30, 83, 103, 32, 47]. This allows for a complete library of results based on system conditions and output descriptions.
- TMA as the metal source:

1. TMA is highly reactive and the production of other types of aluminum based films can be produced, i.e. nitrides and elemental
 2. The methane byproducts produced during surface reactions are inert and thus film etching or chamber reactions can be neglected unlike the use of AlCl and water where the byproduct of the surface hydroxide group and AlCl is hydrochloric acid which will etch the film and cause damage to the reactor.
 3. The size of the methyl ligand is not too bulky resulting in better surface coverage.
- The use of water as the oxygen contributing precursor allows the system to be heated externally to reach the ideal reaction temperature. If however, the oxygen contributing precursor is ozone or plasma it may lead to film degradation because of precursor decomposition due to the nature of the gas being introduced into the reactor at high temperature[75]. Furthermore, the reactor may be forced to cool down due to the introduction of the high temperature ozone or plasma.
 - TMA is an extremely stable molecule having a strong metal ligand bond.

3.4 Structure of TMA

TMA exists both as a monomer (TMA_M) and a dimer (TMA_D) in the gas phase. Monomeric TMA has six electrons in its valence shell and is thus electron deficient driving it to dimerize [82]. Structurally, based on X-ray diffraction data

[97], TMA_D has two aluminum atoms bridged by methyl groups and each aluminum atom is bonded to two terminal methyl groups. We denote M_B and M_T as the bridged methyl group and terminal methyl group respectively. Based on the structural data the following determinations can be made: The monomer structure has D_{3h} symmetry with the bond angles between the methyl group and aluminum, $\angle \text{MAlM}$, measuring approximately 120° . For the dimer structure the angle formed between the terminal methyl groups and aluminum, $\angle M_T\text{Al}M_T$, is measured approximately 117° representing sp^2 hybridization while the angle formed between the the bridged methyl groups and aluminum, $\angle M_B\text{Al}M_B$, is measured approximately 105° representing sp^3 hybridization. Thus the dimer structure has characteristics of both types of hybridization [82]. Geometrically the dimer structure represents two monomer structures as related by a center of symmetry Figure [3.1]. Thus at

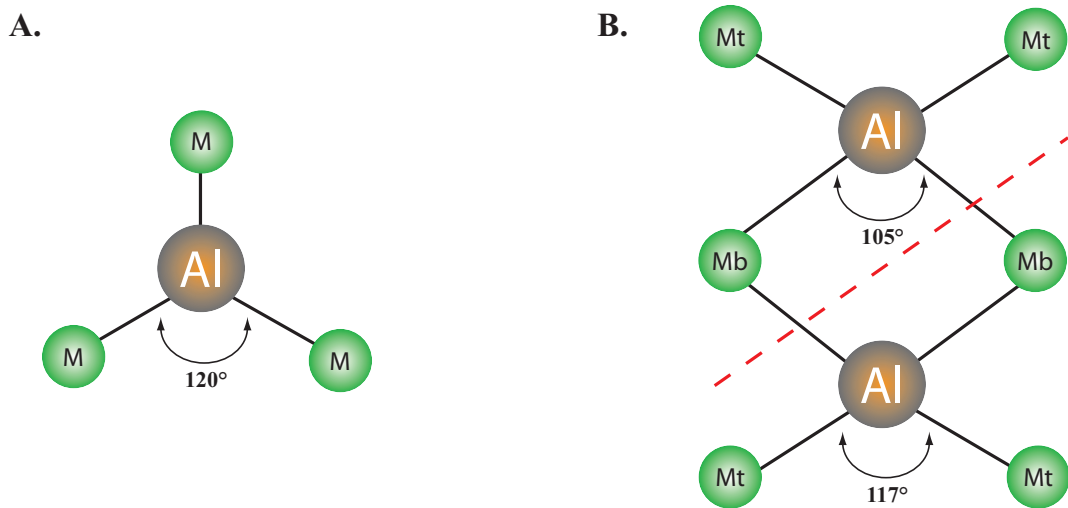


Figure 3.1: A. Structure of monomer TMA. B. Structure of dimer TMA where the dotted red line is the center of symmetry

equilibrium the distinct structures of TMA can be written as:



The equilibrium constant for the above reaction, K_d , can be expressed as:

$$\frac{[TMA_M]^2}{[TMA_D]} = K_d \quad (3.5)$$

If we define x_M as the mole fraction of monomer TMA and x_D as the mole fraction of dimer TMA the equilibrium constant becomes:

$$\frac{\left[\frac{Px_M}{P_o}\right]^2}{\left[\frac{Px_D}{P_o}\right]} = K_d \quad (3.6)$$

with $P_o = 760$ Torr. Since the sum of the mole fractions equal unity:

$$x_M + x_D = 1 \quad (3.7)$$

The equilibrium constant written exclusively in terms of monomer mole fractions is:

$$\frac{x_M^2}{x_D} = \frac{P_o}{P} K_d = \frac{x_M^2}{1 - x_M} \quad (3.8)$$

Solving for x_M , we arrive at:

$$x_M = \frac{-\frac{P_o}{P} K_d \pm \sqrt{\frac{P_o^2}{P^2} K_d^2 + 4\frac{P_o}{P} K_d}}{2} \quad (3.9)$$

In [92] the equilibrium constant is calculated by simulation in the pressure range, 1.01×10^5 Pa and in the temperature range of 300 - 500 k:

$$K_d = \exp\left(\frac{-9624.4363}{T} + 20.2303\right) \quad (3.10)$$

If we solve for the positive value of x_M with typical ALD conditions, $T = 500$ K and $P = .01$ Torr we find that virtually none of the TMA dimer is found and so it is the monomer that interacts with the growth surface Figure [3.2].

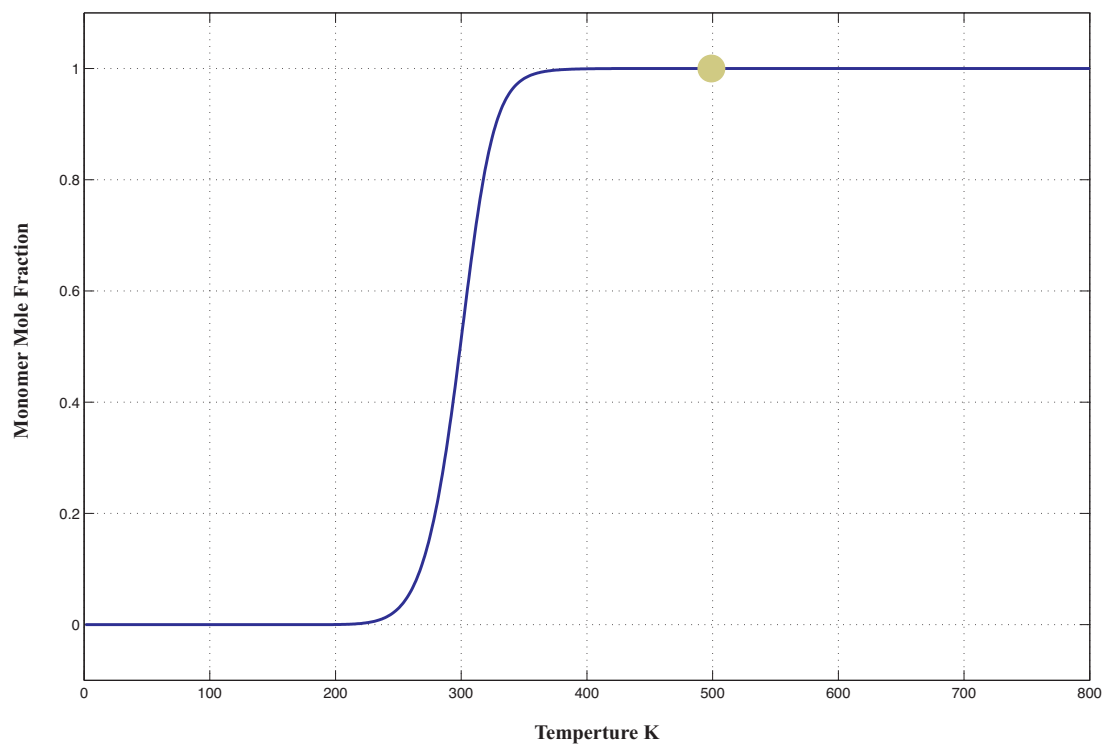
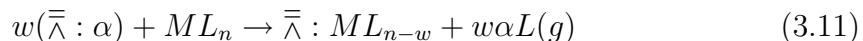


Figure 3.2: Graph of Monomer Mole Fraction, x_M , as a function of temperature using simulation based value for monomer, dimer equilibrium constant, K_d . The green dot represents the reaction condition for this work, clearly showing the existence of only the monomeric structure.

3.5 Overview of Surface Reactions

The adsorption mechanisms involved during ALD deposition can be divided into two branches: Molecules that adsorb anemically and molecules that adsorb strongly. Anemic adsorption results in a weak interaction with the adsorbing gas phase precursor and the substrate. This anemic adsorption is called physisorption and is characterized by the adsorbing molecule retaining its structure where the ligands of the molecule do not react with the surface active site. Physisorption reactions are reversible. Mechanistically physisorption are also known as association reactions. Molecules that adsorb strongly adsorb via chemisorption. Chemisorption reactions are irreversible. During chemisorption chemical bonds are broken and formed between the adsorbing molecule and adsorbent substrate. Mechanistically chemisorption reactions include ligand exchange reactions and dissociation reactions.

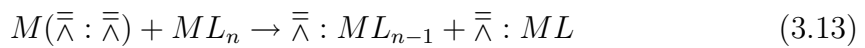
We have defined an active surface site as a potential location for a gas surface reaction. We also define a neighborhood as a cluster of adjacent active sites. In ligand exchange reactions, reactions occur in a one to one ratio of ligands and available active surface sites. As the reaction proceeds the ligand combines with the surface active site to produce a volatile reaction byproduct, while the metal atom and remaining ligands are adsorbed on the substrate Figure [3.3]. If we consider a ML_n metalorganic precursor where a metal atom, M is bounded to n number of ligands, L and this precursor has the potential to react with w number active surface sites which we define as $\bar{\bar{\lambda}}:\alpha$, the ligand exchange reactions can be written:



We define a surface bridged bond as a central metal atom that is bonded to multiple neighborhood sites where its structure is either tent like or resembles an inversed v . In dissociation reactions, the incoming molecule breaks a surface bridged bond and dichotomizes where a ligand reacts with the free electron surface site and the remaining metal atom and ligand combination reacts with with the other adjacent surface site Figure [3.3 B]. If we consider a ML_n metalorganic precursor, and two adjacent surface sites, $2(\bar{\bar{\lambda}} :)$, that are bridged with a metal atom M then the bridged site can be written as:



And the overall all dissociation reaction can be written as:



In association reactions the incoming metalorganic precursor weekly bonds with a surface site coordinatively with out the release of a ligand Figure [3.3 C]. If we define $\bar{\bar{\lambda}}:\alpha$ as an active site and, \longleftrightarrow as a coordinate bond the associative reaction can be written as:



3.6 Saturation Issues in ALD

An important property in ALD is that the gas surface reactions are self terminating. Self termination is important in the atomic layer control of a monolayer.

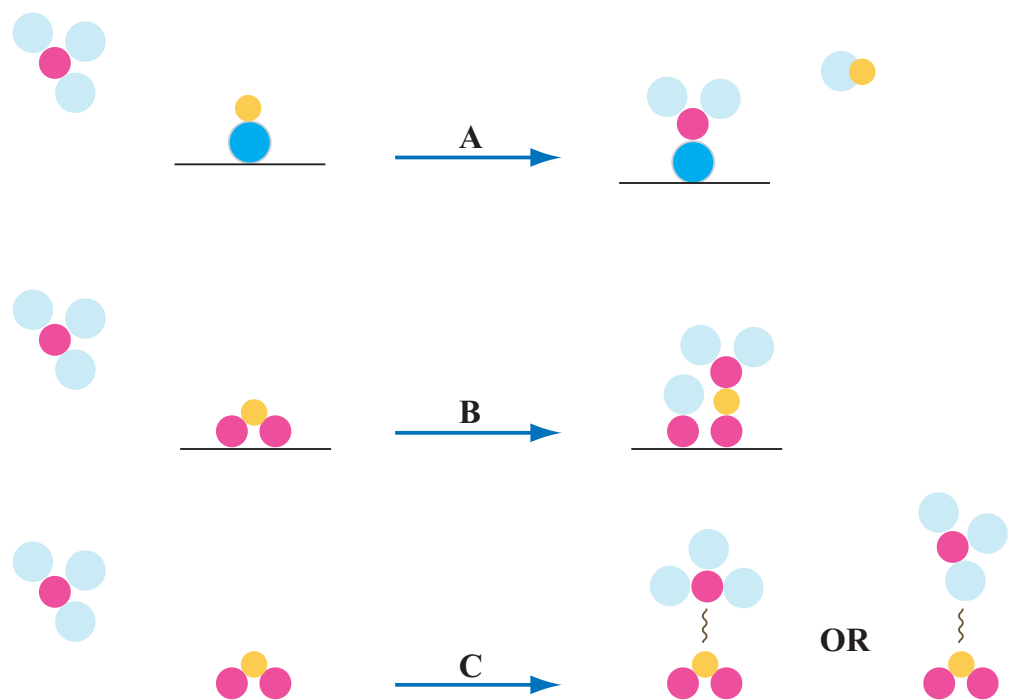


Figure 3.3: Cartoon illustrating the three different ALD mechanisms: A. Ligand Exchange B. Dissociation C. Association

Self termination is inherently chemisorption a irreversible gas surface reaction. We can define a monolayer [76] through the following analogy: Let us assume that the substrate has a surface akin to a checkerboard where every square of the board is capable of adsorbing a gaseous molecule. We define a red checker chip as a single gas phase precursor molecule, for arguments sake let's consider this chip as the first precursor gas. The total capacity of the checkerboard is total number of chips necessary to fill each square of the checkerboard. This total capacity is a monolayer of red chips for chemisorption, or a monolayer of red chips has been produced or grown. If we take this analogy further and introduce a black checker chip as the second precursor gas phase molecule, and allow this black chip to react with the red chips underneath by stacking the chips on top of one another the total capacity of the checkerboard is the total number of black checker chips necessary to occupy all the squares of the checkerboard. This total capacity is a monolayer of black chips for chemisorption, or a monolayer of black chips has been produced or grown. Once the total capacity of the checkerboard has been reached the surface is considered saturated and further reactions are not possible. Self terminating reactions can be considered as reactions that are either "on" or reactions that are "off". If the surface is not saturated the reaction is in the "on" position and surface sites will be occupied until saturation. Once saturation has been reached no further reactions are possible and the reaction can be considered in the "off" position.

There are many factors that can cause non idealities in monolayer growth. Non idealities lead to less than a monolayer of growth per half cycle. During non ideal growth, saturation is reached when gas surface reactions are no longer possible. The

three main causes of premature gas surface reaction termination is steric hindrance, limited number of bonding sites and insufficient precursor dosage. In the case of Al_2O_3 ALD steric hindrance is the limiting case. During steric hindrance the ligand in the ML_n molecule can block or shield a neighboring active site from an incoming gas phase molecule resulting in a pseudocapacity surface. In limited number of bonding sites, premature saturation is reached where an active site that should go through a reaction for true saturation is no longer active and that the total number of active sites is less than ideal for complete saturation Figure [3.4] . During instances of insufficient precursor dosage, the number of active sites are more than the number of incoming gas phase molecules resulting in unreacted active sites.

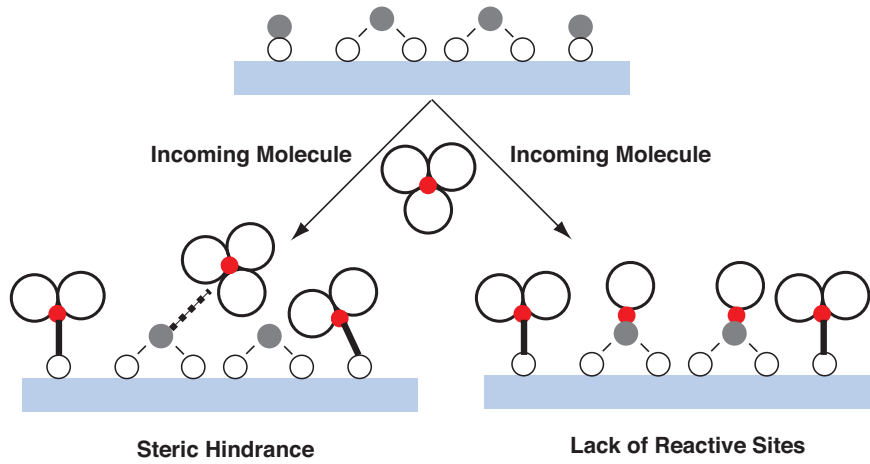


Figure 3.4: Factors that lead to less than a monolayer of growth per cycle.

3.7 Properties of Al_2O_3 Thin Films

In the semiconductor industry, the research for alternative materials to replace SiO_2 as a high k dielectric material has been ongoing in recent years [41]. Among

these, aluminum oxide is highly desirable from both physical and electronic characteristics. Aluminum oxide has a very high band gap (~ 8.8 eV) [27] and a high dielectric constant ($k \sim 9$) [34]. Grazing X-ray diffraction measurements (XRD) [83] show that Al_2O_3 films are amorphous. Ellipsometry measurements [71] determined that the index of refraction of Al_2O_3 films was $n = 1.65$, consistent with a film density $\rho = 3.50$ g/cm³. Electron spectroscopy for chemical analysis measurements [95] showed that the aluminum to oxygen ratio of 0.7 which is indicative of the formation of the layers having a stoichiometry close to Al_2O_3 .

3.8 Experimental Verification of Surface Reaction for TMA and Water

The above TMA and water half reactions describe a very simplistic view of the surface reactions which occur, when in fact the reactions are a bit more complicated. The products of the gas surface reactions are dependent on reaction temperatures, precursor exposure and surface hydroxide densities. It is therefore important to determine the surface morphology *in situ* as the gas surface reaction is progressing. In [22, 71] a series of experiments are carried out to determine the progression of the TMA/water surface reaction as a function of temperature and precursor exposure using Fourier transform infrared (FTIR) spectroscopy using a high surface area alumina membrane as the deposition substrate.

The experiments are conducted in a ultra high vacuum reactor as described in [23] where the initial substrate is mounted on a silicon wafer and placed in a

chamber where a turbomolecular pump enables an operating pressure of $(5 - 6) \times 10^{-5}$ Torr at constant temperature. A Nicolet 740 FTIR spectrometer is used to pass an infrared beam through a pair of 0.5 inch thick CsI windows between pre and post precursor exposures. A difference method is applied where the initial preexposure FTIR measurements is subtracted from the postexposure FTIR measurement to gain insight on the surface species products after each precursor exposure.

3.8.1 Thermal Studies

Initially porous aluminum membrane is exposed to a 2 Torr 5 minute exposure to water producing a hydroxylated surface. This initial surface is then exposed to TMA at 2 Torr for 5 minutes at 300 K. FTIR measurements show a decrease in the Al-OH stretching vibration and an increase in the C-H₃ vibration. A second identical TMA exposure does not result in any changes to the surface. A third TMA exposure at 2 Torr for 5 minutes but at 500 K is followed which results in an almost complete disappearance of the Al-OH stretching vibration and a pronounced increase in the C-H₃ vibration Figure [3.5]. These results indicate that the higher temperature, 500 K, is necessary for converting the hydroxylated surface into a methylated surface.

3.8.2 Water Exposure

To examine the surface species following water exposure, the methylated surface is exposed to a 0.01 Torr water exposure at 500 K and FTIR measurements are carried out as a function of time Figure [3.6 A]. The time dependent change

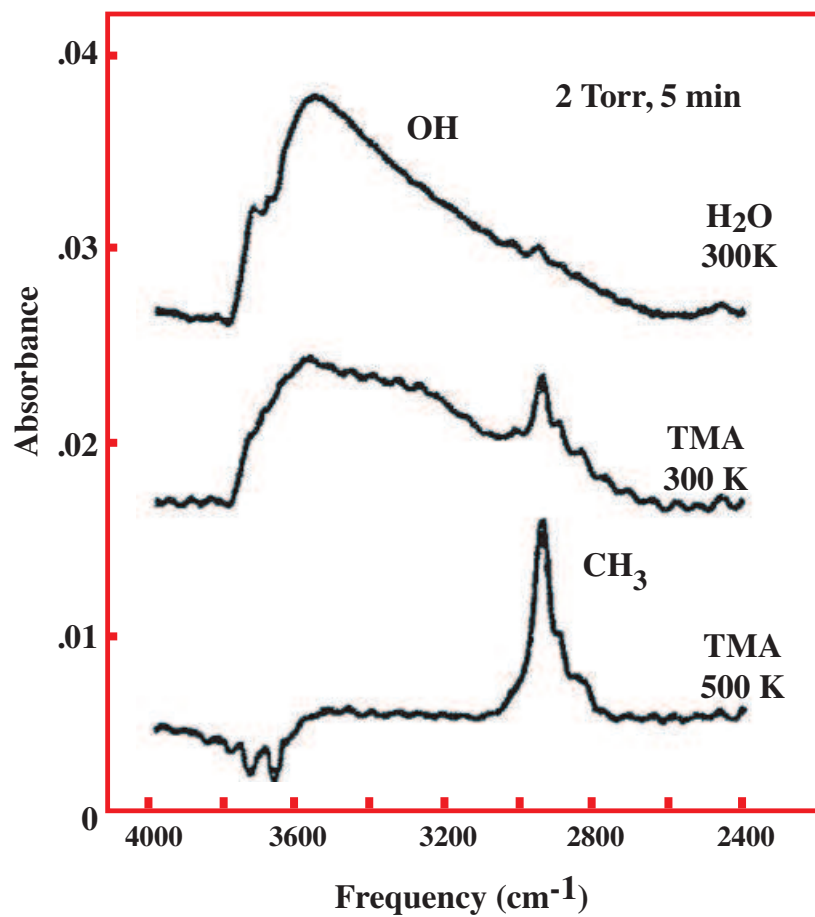


Figure 3.5: Thermal studies from [22] showing infrared absorbances in the hydroxide and methyl stretching regions versus TMA and water exposures at two different temperatures, 300 and 500 K.

to the infrared spectrum clearly shows an increase in the OH absorbance with a pronounced decrease in the C-H₃ absorbance. Normalized integrated absorbances Figure [3.6 B] of C-H₃ and O-H absorbances clearly show a one to one ratio of OH gain and CH₃ loss. Based on these results, it takes exactly one water molecule to

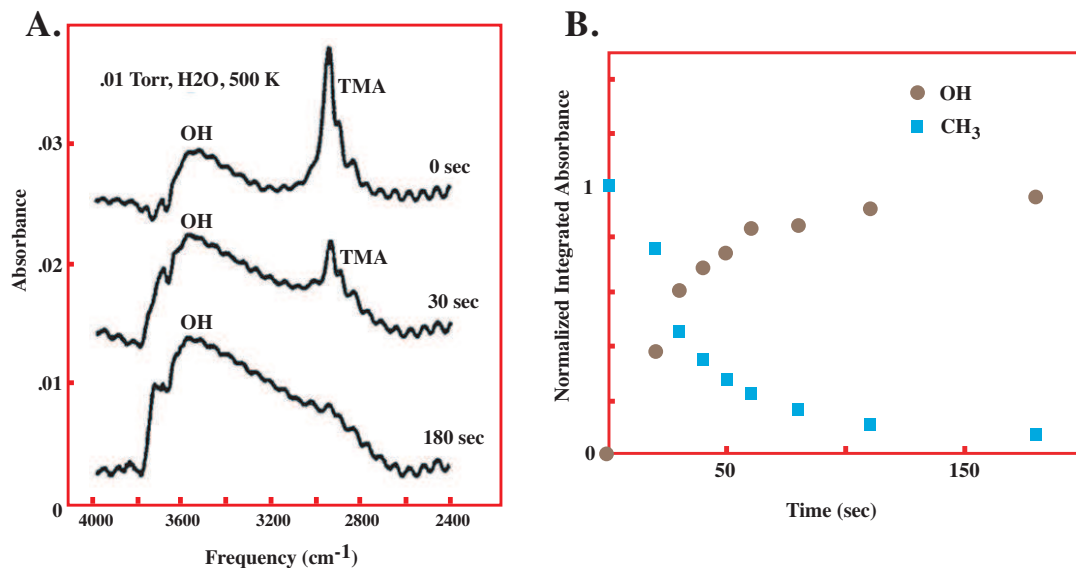
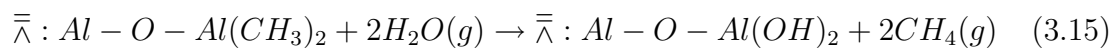


Figure 3.6: Water deposition studies from [22] showing A. absorbances of porous alumina versus 0.01 water exposure at 500 K. B. Normalized integrated absorbances of OH and CH₃.

convert one surface methyl group into a surface hydroxide group:



3.8.3 TMA Exposure With Ligand Exchange Reactions

To examine the surface species following TMA exposure, the hydroxylated surface is exposed to a 0.01 Torr TMA exposure at 500 K and FTIR measurements

are carried out as a function of time Figure [3.7 A]. The time dependent change to the infrared spectrum clearly shows an increase in the C-H₃ absorbance with a pronounced decrease in the O-H absorbance. However, even after a fairly long exposure of 210 seconds a slight O-H absorbance is still seen. This slight absorbance is attributed to steric hindrance where the hydroxide site is shielded by the methyl ligand as explained in the ALD non-idealities. Normalized integrated absorbances Figure [3.7 B] of C-H₃ and O-H absorbances clearly show that the TMA and hydroxylated surface reaction proceeds via a series of ligand exchange reaction dependent on hydroxide surface density. Initially the C-H₃ absorbance is zero and after some

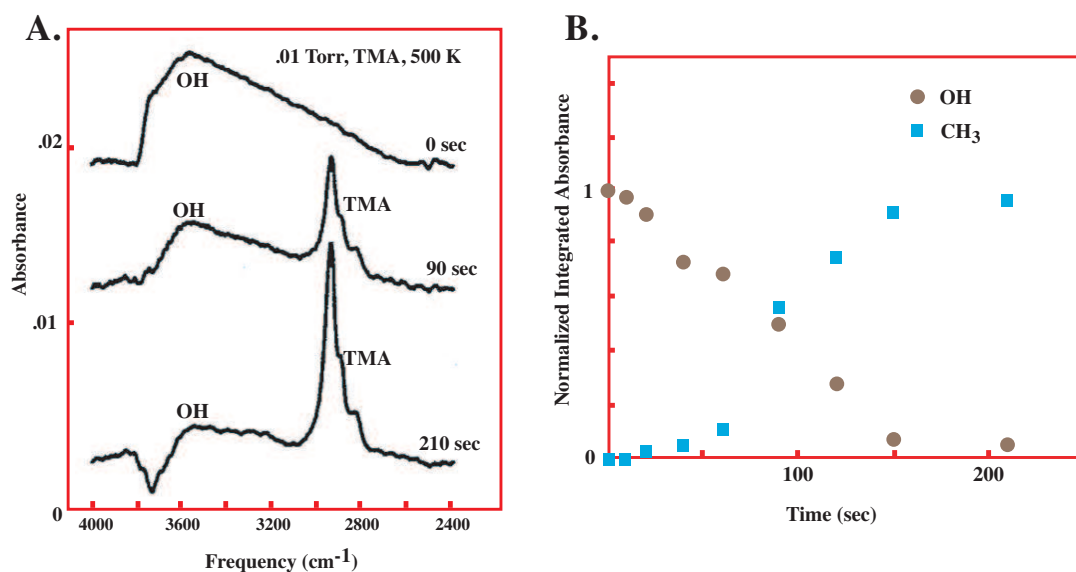
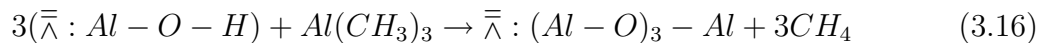


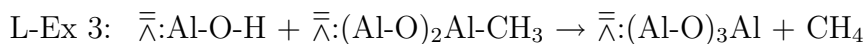
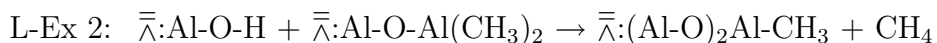
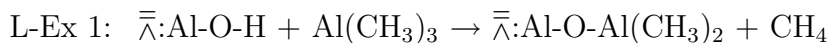
Figure 3.7: TMA deposition studies from [22] showing A. absorbances of porous alumina versus 0.01 TAM exposure at 500 K. B. Normalized integrated absorbances of OH and CH₃.

time an exponential increase is seen followed by a constant saturation trend after 150 seconds. The OH absorbance has a linear decrease followed by a constant satu-

ration trend after 150 seconds. Here the the ratio of OH loss and CH₃ gain is not one to one. Based on these results the following reaction mechanism can be proposed. Initially, as the substrate is saturated with hydroxide groups and a TMA molecule approaches the surface for a potential reaction, a single methyl ligand reacts with with a single hydroxylated active site releasing methane as the remaining dimethyl aluminum molecule chemisorbs in the substrate. If in the neighborhood a second active hydroxylated site is available then one of the two remaining methyl ligands will react with that active site releasing methane leaving behind a monomethyl aluminum surface specie. If within this cluster a third active site is available, then the final methyl ligand will react with the hydroxide specie releasing methane and producing a tent like aluminum specie:



The series of ligand exchange reactions can be written as and visualized as Figure [3.8]:



Furthermore, the FTIR results dictate that during a TMA exposure there is a preferential reaction mechanism based on the hydroxide surface density. If there exists a sufficient OH surface density for the formation of the tent like aluminum surface specie then that reaction mechanism, L-Ex 1 -3, will have priority. If there exists

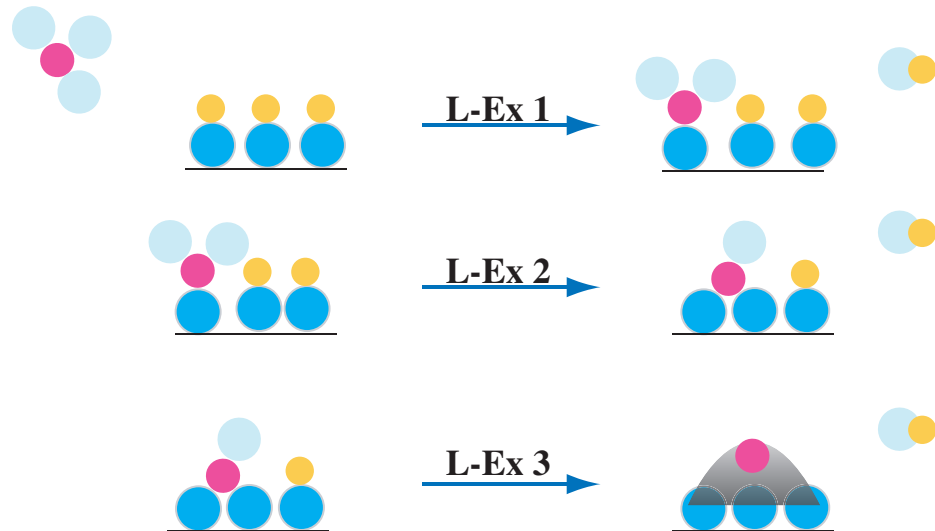


Figure 3.8: A series of ligand exchange reactions resulting in tent-like structure

two neighboring surface hydroxide active sites forming a 'v' like aluminum surface specie, $\overline{\overline{\lambda}}:\text{Al}-\text{O}-\text{Al}(\text{CH}_3)_2$, then the reaction mechanism, L-Ex 1- 2, will have priority. If a lone surface hydroxide site exists then the reaction L-Ex 1 with two surface methyl groups will most likely occur.

3.8.4 TMA Exposure With Dissociation Reactions

TMA surface reactions with singular hydroxide active sites results in the L-Ex 1 reaction. However, if a hydroxide site is not available and the aluminum tent-like surface specie exists, then TMA may react with this structure via a dissociation reaction also called a methyl transfer reaction [22]. In this new reaction, the gas phase TMA molecule binds to the lone electron pair of one of the surface oxygen species, and subsequently undergoes a dissociation reaction [75, 76, 26] where a CH_3 group is transferred from the TMA to the surface aluminum atom the remaining

dimethylaluminium component binds to the oxygen atom previously bonded to the surface aluminum.



3.8.5 Methylated and Hydroxylated Half Reactions

Figure [3.9] confirms that the substrate surface changes from a hydroxylated surface to a methylated surface back to a hydroxylated surface and back to a methylated surface based on the precursor exposure. The plot also clearly states that the reactions are self terminating. However, slight absorbances of hydroxylated species are still present after TMA exposure. This slight hydroxylated feature can be attributed to two sources: 1) The hydroxylated group is being shielded by the methyl ligand prevent a TMA molecule from accessing the site. 2) The hydroxide group is buried within the film.

3.9 Transition State Theory

The gas surface reaction between the precursor gasses and the surface is explored atomistically utilizing transition state theory (TST) where the formation energies of the byproducts are determined using density functional theory, DFT [35, 100]. In density functional theory, DFT is a quantum mechanical method to investigate the electronic structure of many-body system [14]. The energies and geometries of reactants and products are predicted by DFT making possible the prediction of surface reactions. Transition state theory provides a reaction path

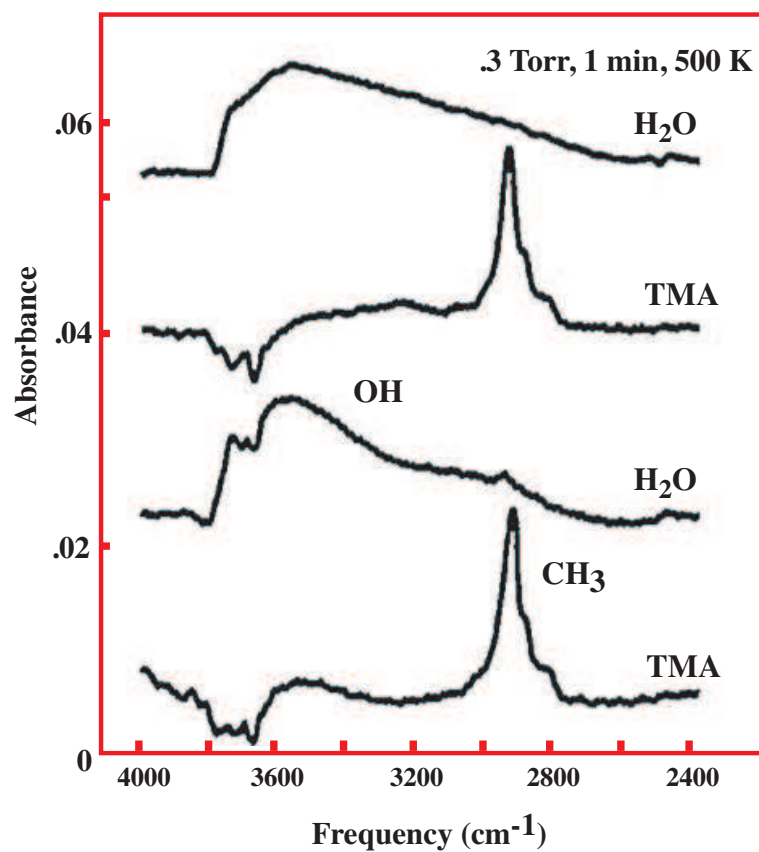


Figure 3.9: TMA and water deposition studies from [22] showing the teetering between hydroxylated surface and methylated surface

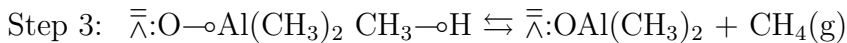
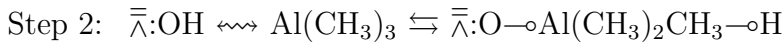
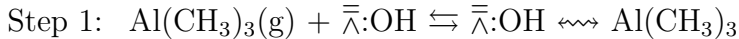
from the initial reactants to the final products. The reaction path consists of three basic steps starting with the introduction of the reactant molecules:

Step 1: The adsorption of a gas phase molecule to a potential reaction site resulting in the formation of a *precursor-site complex*.

Step 2: The formation of a *transition state structure* where bonds are broken and created to create the gas by-product.

Step 3: Final creation of byproduct and new surface site.

As described by [41, 100] the TMA half reaction proceeds by first adsorbing on a hydroxide surface site via a Lewis acid-base interaction forming a precursor-site complex. In the case of Al_2O_3 ALD and the metal producing half reaction, precursor TMA acts as a Lewis acid and the hydroxide surface group acts as a lewis base. After the adsorption step one of methyl ligands reacts with a hydrogen atom on the surface site forming a transition state structure. This is followed by the desorption of methane and the creation of the final surface product. Written in terms of TST steps the TMA/active site reaction can be represented as follows:

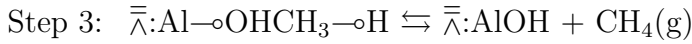
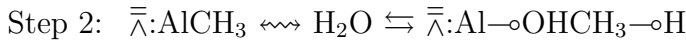


where $-\text{o}$ is the formation of a bond.

Based on DFT the adsorption step is exothermic with a formation energy of 0.61 eV the transition state is activated with an activation barrier of 0.52 eV and

the desorption step and final surface reaction product proceeds exothermically with an activation barrier of 1.09 eV Figure [3.10 A].

Similarly, the water half reaction proceeds by forming a precursor/active site Lewis acid Lewis base complex with a surface methyl group. A hydrogen atom then reacts with the surface methyl ligand forming a transition state complex. This is followed by methane desorption and the creation of a new complimentary hydroxide surface site. Written in terms of TST steps the water/active site reaction can be represented as follows



Based on DFT calculations the adsorption step is exothermic by 0.57 eV the transition state is activated with an activation barrier of 0.70 eV and the desorption step and final surface reaction product proceeds with an activation barrier of 0.91 eV Figure [3.10 B]. Looking at the reaction paths of the TMA and water half reactions several conclusions can be ascertained. During TMA deposition the activation barrier needed to be crossed to reach the transition state from the adsorbed state has a delta of -9 eV. While the the activation barrier needed to be crossed to reach the transition state from the adsorbed state during water deposition is +13 eV. These values show that it is much easier to react TMA with a surface hydroxide group, while it is much more difficult for water to react with a surface methyl group. The reason for the disparity between the two numbers is due to the fact that physically

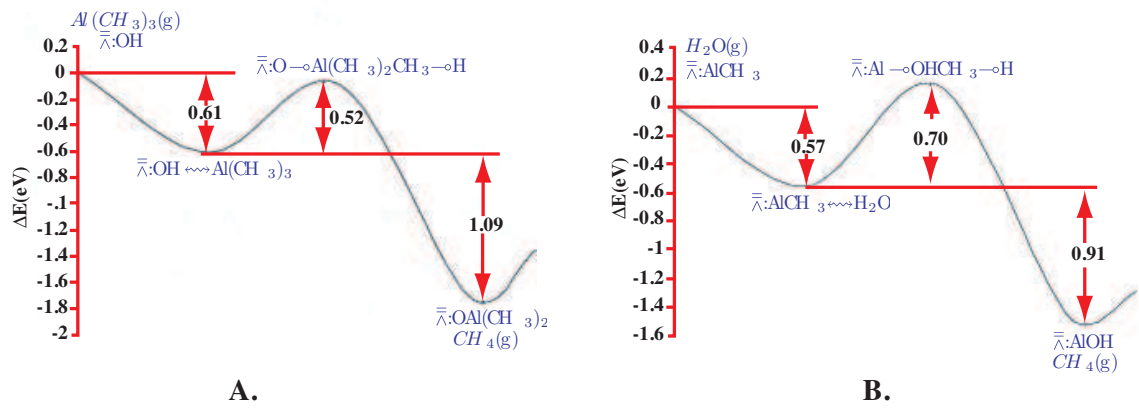


Figure 3.10: DFT studies by [100] showing the progression of either A. TMA and hydroxide group forming methane and surface methyl group via transition state theory and B. Water and surface methyl group forming methane and surface hydroxyl group via transition state theory.

the methyl ligand is much bigger than the hydroxide group and is much easier for the reaction to occur. The opposite is true for the water reaction the water molecule is much smaller than the methyl surface group and is therefore more difficult for the reaction to proceed. These results can be quantified by determining a probability of a reaction using the Arrhenius equation:

$$k_{rxn} = Ae^{\frac{-E_a}{kT}} \quad (3.18)$$

where k_{rxn} is the number of gas phase molecule/surface active site collisions per second. In the equation, A is the pre-exponential factor and is the attempt frequency of the reaction while the second term is a probability term that for any given collision a reaction will occur. Within in this term k is Boltzmann's constant, 8.617×10^{-5} eV K⁻¹, and T is the temperature in kelvin. We can use the reaction probability term to gauge the likely hood of a reaction by utilizing the following relationship:

$$RxnProbability = \frac{e^{forward}}{e^{reverse}} \quad (3.19)$$

Using TST and the activations energies from [100] we arrive at:

$$RxnProbability = \frac{e^{\frac{-E_{AS}}{kT}}}{e^{\frac{-E_{AS}}{kT}} + e^{\frac{-E_{TS}}{kT}} + e^{\frac{-E_P}{kT}}} \quad (3.20)$$

where AS is the adsorbed state, TS is the transition state and P is the final product. Using 500 K as our operating temperature the reaction probability for the TMA exposure is $\sim 90\%$ while the reaction probability for the water exposure is $\sim 5\%$

3.10 Mass Balance Approach for Surface Species Statistics

In [75, 76] a method is presented that relates the growth per cycle of aluminum oxide to the chemistry of its growth. This method based on mass balance allows for the calculation of the total number of ligands attached to the growth surface, a theoretical upper limit for ligand packing, ligand coverage, and the thickness increment per cycle. This method provides a numerical means for gathering surface statistics necessary for our method for aluminum oxide growth via ALD.

During the TMA deposition process the chemisorption of the organometallic precursor is depending on the hydroxide surface density. The hydroxide surface density dictates the number of ligands that are bonded to the chemisorbed aluminum atom. These reactions can be modeled by counting the number of ligands that are attached per unit area. The number of ligands that are attached is a function of the number of initial ligands attached in the gas phase of the organometallic the number of reacted surface sites per unit area and the number of chemisorbed metal atoms per unit area. If we define the following:

n: The number of initial ligands attached to the organometallic gas phase precursor.

ΣM : The number of metal atoms attached per unit area.

Σa : The number of reacted surface sites per unit area.

ΣL : The number of ligands attached to the surface per unit area.

According to mass balance ΣL is then proportional to n , ΣM , Σa through:

$$\Sigma L = n\Sigma M - \Sigma a \quad (3.21)$$

The mass balance can be verified by applying the model to the ligand exchange reactions and the dissociation reaction. Practically saturation of the substrate after TMA exposure results in a percentage of the monolayer. Typically the growth per cycle or GPC is defined as the thickness increment per ALD cycle which is related to the total number of metal atoms chemisorbed on the substrate. Total adsorption is dictated by the saturation issues described above. In aluminum oxide ALD, the dominant factor that retards saturation is steric hindrance. It is therefore valuable to determine the maximum number of ligands that can be chemisorbed per unit area.

If we assume the methyl ligands have a spherical shape with radius, r_L we can calculate the filling area of one methyl group assuming hexagonal packing through the relationship:

$$a_L = 2\sqrt{3}r_L^2 \quad (3.22)$$

The maximum theoretical upper limit for ligand packing is then defined as:

$$\Sigma L^{Theoretical} = \frac{1}{a_L} = \frac{1}{2\sqrt{3}r_L^2} \quad (3.23)$$

For TMA the van der Waals radius of the methyl ligand is $0.20nm$ [19] the maximum theoretical number of methyl groups that can be chemisorbed per unit area is thus $7.2nm^{-2}$. For a full monolayer saturated growth the thickness per cycle, water and TMA exposure, is equivalent to the height of a row of atoms of the aluminum oxide bulk material. The average value of the thickness is calculated from the height of a cube containing one aluminum oxide atom:

$$h = \left(\frac{M}{\rho N_A}\right)^{\frac{1}{3}} \quad (3.24)$$

It will be shown that a cube is chosen as the representative geometry for the application of the lattice based Monte Carlo simulator. Furthermore, the number of metal atoms per unit surface area can be expressed as:

$$N_{Al} = \left(\frac{\rho N_A}{M}\right)^{\frac{2}{3}} \quad (3.25)$$

For aluminum oxide the theoretical total number of aluminum atoms per nm^{-2} is 12.0 where the overall growth per cycle is 30-40 %.

3.11 Graph Based Data Structures

As discussed there are many different reactions that are possible during the TMA ALD half reaction based on the surface structure. We present a framework that organizes these reaction tabularly and a method for visualizing the different reactions and the pathways for these reactions via a graphical representation. We define a state as a static structure that represents a possible surface configuration following either a TMA interaction or a water interaction. For the TMA water chemistries described above the surface states can be visualized as a series of individual post reactions. The surface states can be combined to show visually the progression of the gas surface reaction through reaction tree, directed graph and adjacency matrix data structures. The reaction tree represents the various reactions that each state can go through. The arrows represent the direction of the reaction. Each reaction represents a single molecule reacting with that state: a single water molecule, a single TMA molecule or a surface reconstruction. By following the reaction tree, the evolution of the Al_2O_3 film can be visualized. The reaction tree can

be translated into a directed graph or digraph where each surface state is a node in the graph. The ordered pair of nodes or the direction of the reaction from the two surface states forms an edge of this graph where the “from state/node” is called the source node and the “to state/node” is called the sink node. By connecting all of the states we form the digraph. A path within the digraph is a sequence of nodes where each node is connected via an edge to the next node in the sequence. The first node in the sequence is called the start node and the last node in the sequence is called the end node. When the start node and end node are the same then the path is called a cycle or circuit. Digraphs can also be represented as a $n \times n$ matrix A where n is the total number of nodes in which $A_{ij} = 1$ if an edge exists from node _{i} to node _{j} and $A_{ij} = 0$ otherwise. A weighted digraph is a directed graph where each edge has an associated numeric value or weight. The shortest path in a directed graph is determined by the least number of hops from the start node to the end node. In the weighted directed graph the shortest path is determined by the minimum cost associated by summing the numeric values of the edges in the sequence from the start node to the end node.

Chapter 4

Modeling Surface Structures

4.1 Overview

This chapter focuses on the methods for modeling the gas surface reactions between the pore wall and the precursor species. The gas surface reaction is considered a fast process at the atomistic scale. This chapter begins by reviewing available techniques to model surface morphologies followed by a discussion of the Markovian master equation and the Poisson distribution. The film evolution lattice based Monte Carlo method is reviewed by first describing the lattice data structure which is followed by the lattice representation of the precursor/surface chemistries. The algorithm is discussed as well as simulation results.

4.2 Review of Atomistic Scale Simulations for Thin Film Processing

Atomic-scale models range from *ab initio* quantum dynamic simulations to molecular dynamics simulations typically preferred by theoretical chemists. From a modeling point of view, considerable effort has been put into understanding high-k materials. There are several methods available that model surface morphologies including:

1. First principle approach in calculating reaction pathways

2. Mean field approximations in describing film morphologies based on nucleation theory
3. Molecular dynamics simulations to describe the diffusion of molecules on a substrate
4. Chapman-Kolmogorov equation
5. Monte Carlo methods describing thin film properties per cycle

4.2.1 Density Functional Theory

The second method of choice is the *ab-initio* DFT methods. In density functional theory, DFT is a quantum mechanical method to investigate the electronic structure of a many-body system. The energies and geometries of reactants and products are predicted by DFT making it possible to predict surface reactions. Many investigations have been done in modeling ALD surface reactions [67, 100]. Elliot and Greer [26] focused on the TMA exposure step of fully hydroxylated and bare alumina surfaces, showing that both are highly reactive and that the reaction extent is limited only by the steric hindrance of the methyl groups. Some lattice Monte Carlo (MC) simulations exist (e.g., [63]), but are mostly limited the initial phase of film growth when the film structure is most influenced by the crystalline nature of the substrate. One exception is the MC simulation paper by [74] which focuses on the structure of amorphous Al_2O_3 and not the reaction processes generating the film.

4.2.2 Mean Field Approximations

Mean field approximations are based on the idea that a many-body system can be replaced with a one body average. For film growth, mean field approximations are introduced in 1971 [96] for epitaxial growth where surface coverage evolution is a measurement of the coalescence of epitaxial islands. In epitaxial growth, clustered deposition sites, islands, grow and combine to uniformly cover the substrate where the islands have a distribution of sizes, locations and shapes. The mean field concept is introduced by an average island [93] where at any time τ all of the islands have the same shape, size and are spatial distributed evenly. Coalescence is achieved by calculating the growth rate of the average island based on a predetermined mechanism and applying that growth rate to all of the islands until a maximum coverage is reached. This maximum coverage is thus based on an average quantity and this average quantity leads to an average kinetic rate equation.

4.2.3 Molecular Dynamics Simulations

Molecular dynamics simulations, MDS, have been carried out in describing the surface diffusion of large clusters of atoms on substrates [21]. Nano-islands are clustered aggregates of atoms that are created one atom at a time on a substrate [51]. These nano-islands when organized as a periodic array of a set size can be used for quantum dots [8] or as catalysts [11]. The draw back of creating these structures is that the cluster deposition is dependent on the substrate where uniformity may be hindered due to energy barriers for diffusion, or atomic exchange between the

deposited atom and the substrate [51]. An alternative to this approach is to create the cluster nano-island first and then deposit the entire island on the substrate. However, this approach can lead to the island diffusing along the substrate. This is a consequence of the diffusion coefficient increasing as the diameter of the island increases [9] due to the mismatch in the lattice parameters between the cluster and the substrate. In MDS, molecular movement is calculated by integrating Newtons equation of motion [66]. There are three ingredients for a molecular dynamics simulation:

1. A model for the interaction between atoms, molecules, and surfaces.
2. An integrator that propagates particle positions and velocities at each time step.
3. A statistical ensemble where pressure, temperature and the number of particles are controlled.

The atoms of the cluster and the substrate are modeled as Lennard-Jones atoms where the interaction occurs through a Lennard-Jones potential. The substrate is modeled as a lattice connected by harmonic springs where the center of mass of the cluster is centered on a substrate atom. The diffusion coefficient is then determined based on the movement of the entire cluster.

4.2.4 Chapman-Kolmogorov Equation

The Chapman-Kolmogorov equation provides a method for generating a complete probability distribution of a surface instead of an average quantity as computed

by mean field approximations. This method allows for the calculation of measurements based on the configuration of atoms such as the surface step density [69]. A state of a lattice is defined by a matrix H where the matrix elements h_{ij} is the height of the lattice at site i, j . Initially H has a value of 0 and after m atoms have been deposited the probability for a certain configuration, $P(H; m)$ is [69]:

$$P(H; m) = P(h_{ij}H; m) \quad (4.1)$$

The growth of the lattice is a Markov process where the configuration of the lattice differs during each discrete deposition step. Therefore the probability for a lattice to have a particular configuration H is based on a transition probability between a configuration at H_i and configuration H in one deposition step:

$$W(H|H_i; m - 1) \quad (4.2)$$

where the probability of a given configuration is the sum of all possible configurations H_i that may give rise to H [69];

$$P(H, m) = \sum_i W(H|H_i; m - 1)P(H_i; m - 1) \quad (4.3)$$

Using this complete probability, surface configuration can be determined for two extreme cases [69]:

1. **Random deposition:** Atoms react to random sites and the diffusion of atoms across the lattice is forbidden. In this case the growth of higher layers can begin prior to the completion of one layer.
2. **Perfect layer growth:** Impinging atoms diffuse to the highest unfilled layer, growth proceeds as the sequential filling of monolayers. In this situation there

are two distinct heights, the height of the incomplete layer and the height of the complete monolayer.

4.3 Novel Computational Method for Surface Description

The main computational contribution of this paper is to define a numerical representation of ALD films by approximating the film’s true molecular structure on a 2D lattice. We see our approach as a method of *coarse graining* the potentially complex nature of the films, limiting the number of degrees of freedom to a more manageable level of computational complexity. While our lattice representation only approximates the spatial relationships of atoms in the film, it will give useful information about the film structure and will rigorously keep track of bonds between atoms. We will examine the evolution of ALD film characteristics, grown on a crystalline Al_2O_3 substrate and examine how the film structure and composition evolve with ALD cycle number.

4.4 KMC Overview with Elementary Example

Kinetic Monte Carlo or KMC is a method for modeling the dynamic behaviors of molecules by comparing the rates of individual steps with random numbers. Kinetic Monte Carlo is a dynamic form of the MC methods and is a widely used class of computational algorithms for simulating the behavior of various physical and mathematical systems. KMC is distinguished from other simulation methods (such as molecular dynamics) by being stochastic, that is, nondeterministic in some man-

ner usually by using random numbers (or, more often, pseudo-random numbers) as opposed to deterministic algorithms. Because of the repetition of algorithms and the large number of calculations involved, Monte Carlo is a method suited to calculation using a computer, utilizing many techniques of computer simulation. KMC does not tell you what a particular surface looks like but it will tell you information about the surface coverage and the time needed for saturation.

The predecessor to KMC is Monte Carlo simulation. MC simulations are a quasi-random approach to time evolution. MC methods evolve according to a stochastic algorithm, which allow the exploration of the entire space of the system [52]. The MC methods follow a Markov process to evolve a system towards equilibrium, regardless of the pathway. Monte Carlo methods cannot be interpreted dynamically as a process that simulates random motion in time. The general algorithm for KMC methods is to solve numerically the master equation:

$$\frac{dP_i}{dt} = \sum_j \sigma_{ij} P_j \quad (4.4)$$

where P is the probability that the system is in some particular state i at some time t . The matrix σ contains transition rate elements where $\sigma_{i,j}$ denotes the rate for the transition from state i to state j . The master equation follows a Markov process, where each transition is not dependent on any other transition that has occurred or will occur, each transition is independent from each other therefore the master equation can then be written as:

$$\frac{dP_i}{dt} = \sum_{j \neq i} (\sigma_{ij} P_j - \sigma_{ji} P_i) \quad (4.5)$$

Thus at equilibrium the master equation follows detailed balance, where π_i and π_j are the equilibrium probabilities for states i and j and thus follows:

$$\sigma_{ij}\pi_j = \sigma_{ji}\pi_i \quad (4.6)$$

Generally, dynamic Monte Carlo can be regarded as algorithms that numerically solve the Master Equation by choosing randomly among various possible transitions and accepting or rejecting particular transitions with appropriate probability [52]. After each transition, time is incremented. Furthermore if a transition is probable at some time t that same process can again be probable at some time $t + \Delta t$.

4.5 Poisson Distribution

The independence of the transitions and the dynamical interpretation of the dynamic Monte Carlo method is by definition a Poisson process. The Poisson process is a stochastic process that is defined in terms of the probability of the occurrences of events at a certain time t with some average transition rate. If we define n as the total number of occurrences of a state $i \oplus j$ in some time interval $t + \Delta t$:

$$\frac{dP_n}{dt} = \sigma(P_{n-1}(t) - P_n(t)) \quad (4.7)$$

When $n = 0$ a transition has not occurred and:

$$\frac{dP_0}{dt} = \sigma(P_0(t)) \quad (4.8)$$

solving for P_0 :

$$P_0 = e^{-\sigma t} \quad (4.9)$$

substituting into 4:

$$P_1 = \sigma t e^{-\sigma t} \quad (4.10)$$

Applying further substitutions for $P_2(t), P_3(t), P_4(t), \dots, P_n(t)$ we arrive at the Poisson distribution:

$$P_n = \frac{(\sigma t)^n}{n!} e^{-\sigma t} \quad (4.11)$$

4.6 Kinetic Monte Carlo Example

An elementary example of a KMC method is to simulate gas phase deposition on a lattice substrate utilizing the CVD technique. In chemical vapor deposition there are three possible surface events:

1. adsorption
2. desorption
3. surface diffusion.

Each of these surface events can be described by three rates: a rate of adsorption, a rate of desorption and a rate of surface diffusion. Therefore, in the Poisson process the expected number of occurrences that occur is equal to a total rate: $\sigma = \sigma_A + \sigma_D + \sigma_{SD}$. Thus, if there are three types of events the total number of occurrences of an event of three types is, $n = n_A + n_D + n_{SD}$. And the Poisson distribution follows:

$$P(\sigma) = \frac{\sigma^n}{n!} e^{-\sigma} \quad (4.12)$$

An important aspect of this distribution is that an average time between events can be calculated. The probability density of time between successive events becomes:

$$P(t) = \sigma e^{-\sigma t} \quad (4.13)$$

and the mean time between successive events beomcomes:

$$\langle t \rangle = \frac{1}{\sigma} \quad (4.14)$$

This relationship allows us to obtain a real time rather than a simulation time. In this CVD process, standard Langmuir kinetics are followed. The simulation begins by generating a symmetrical lattice where each point on the lattice represents a deposition site and a flowchart for events is followed Figure (4.1). For simplicity,

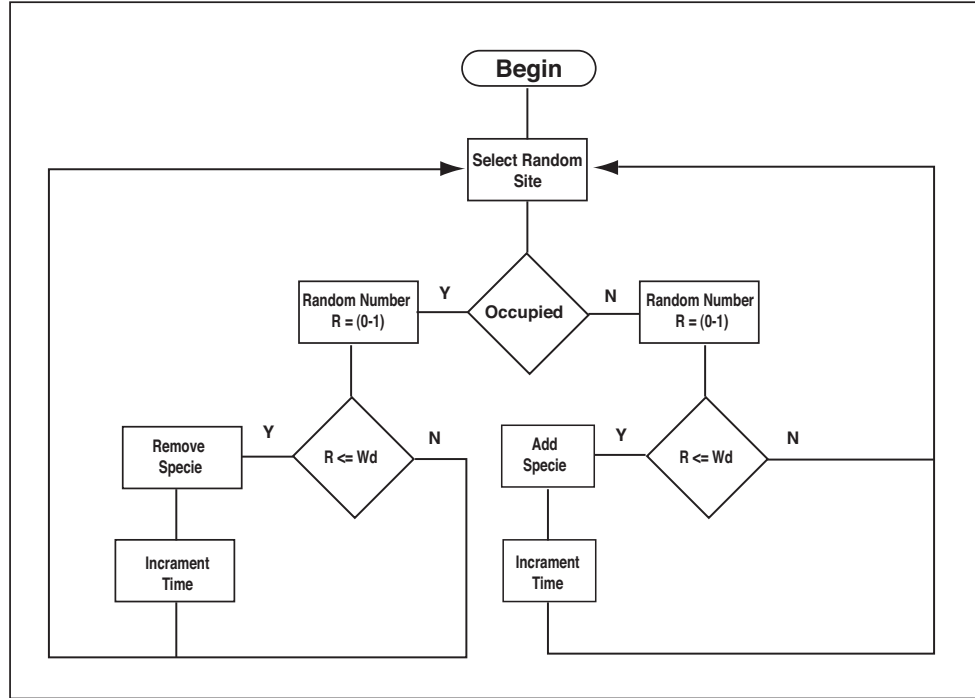


Figure 4.1: Simple KMC Flow Process

surface diffusion effects are ignored. First a random site is chosen from the lattice. If

the site is occupied, a random number is generated between 0 and 1, and is compared to a transition probability. For CVD the transition probability is equivalent to the individual rate divided by the total rate. If the random number is less than the transition probability surface desorption is executed by removing the surface specie and time is incremented using the Poisson distribution. If the random number is above the transition probability an event does not occur and another random site is chosen. If the random site is empty, a random number between 0 and 1 is chosen and compared to another transition probability. If the random number is less than the transition probability a specie is added to the site and time is incremented, otherwise another random site is chosen. This procedure is repeated until saturation is achieved or a desired coverage is reached.

4.7 The Lattice

As a first step to understanding how local deposition surface chemical characteristics determine the reactions that can take place, we limit our modeling to a two-dimensional approximation of the film structure [25, 7]; this is partly inspired by the reactions shown in Figure 4 of [76]. In this work, we introduce the lattice shown in Figure (4.2); the brick-pattern structure represents a microscopic region of the (transverse) growth surface, discretized in one dimension representing spatial position along the growth surface (with periodic boundary conditions), and the other (the vertical direction) the depth of the deposited film. The film depth index is n , with $n = 1$ being the lowest level of substrate considered, and m being the

index along the film surface. Because of the periodic boundary conditions, lattice sites in column $M + 1$ are equivalent to those in column 1.

Each lattice site will contain a surface group or bond structure potentially capable of undergoing a reaction, a bulk film species, or will be empty. The next concept we introduce is that the vertices where three lattice sites meet are the only locations where Al atoms can be found. It is this lattice-vertex structure that is key to guaranteeing correct film stoichiometry and bond configurations. The notation used to index Al horizontal site locations is $k = 1, \dots, 2M$; the Al atoms associated with each lattice site are located at the bottom (left, center, or right) of each site (see Figure (4.2 right), and so the vertical position index of the Al atoms also is $n = 1, \dots, N$.

Computationally, two arrays must be defined. The first corresponds to $s(n, m)$ and contains all ligands and surface bonds involved in the ALD reactions, as well as the O and OH species making up the bulk film. The second array $a(n, k)$ contains the locations of the Al atoms. Note that while the a array contains twice the number of elements of s , most of these elements normally will be empty.

The crystalline density of Al_2O_3 is 4 g/cm^3 ; given its molecular weight of 101.98 g/mol , we can compute an aluminum atom number density of approximately 41 Al atoms/nm^3 and 62 O atoms/nm^3 . If we consider the basic molecular unit of an alumina film to be $\text{Al}_{2/3}\text{O}$, the volume of this unit is 0.016 nm^3 or a cubic box with sides approximately 0.25 nm in length.

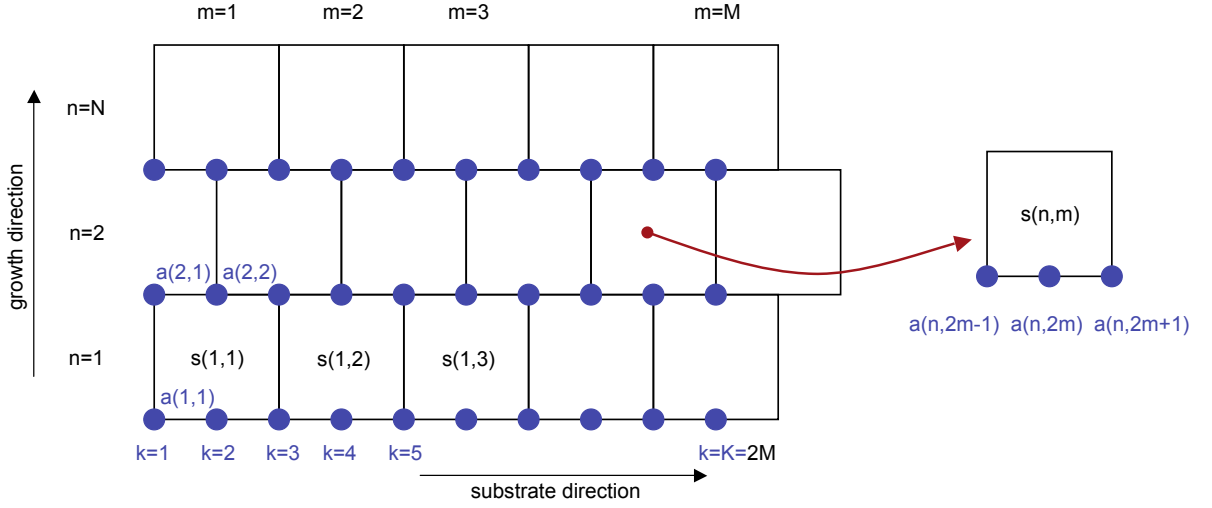


Figure 4.2: The 2-dimensional lattice structure developed to represent the structure of ALD Al_2O_3 films.

4.7.0.1 Species occupying the lattice sites

Given the lattice box edge length of 0.25 nm , we now consider the chemical species that occupy the sites. As computed, each site can contain one $\text{Al}_{2/3}\text{O}$, and so an Al_2O_3 molecule occupies three adjacent sites. The van der Waals radius of the methyl group CH_3 is 0.2 nm [77]; this corresponds to a cross-sectional area of 0.1257 nm^2 meaning the CH_3 ligand is larger than our lattice box size. This will limit the methyl group density on the growth surface and so the steric hindrance effects must be accounted for in the TMA surface reactions. The hydroxyl group OH fits within each lattice site; sites on the growth surface may also contain the Al-O bonds corresponding to oxygen bridges that may undergo a dissociation reaction with TMA.

In Figure (4.3), we see in the top-most diagram a fully hydroxylated growth

surface above a substrate consisting of a dense Al_2O_3 film; note the regular structure of the substrate, how it has the correct Al/O ratio, and that the density of the substrate is found to be 4 gm/cm^3 . The surface OH groups occupy the light blue lattice sites while the dark gray sites above are empty. The Al atoms are denoted by the filled dark blue circles below the hydroxyl groups and bulk O atoms; note that an Al atom is bound to a single O or OH group above and two below when the Al is centered below a lattice site, and it is bound to two above and one below when it is located between two lattice sites. Given the lattice size calculations

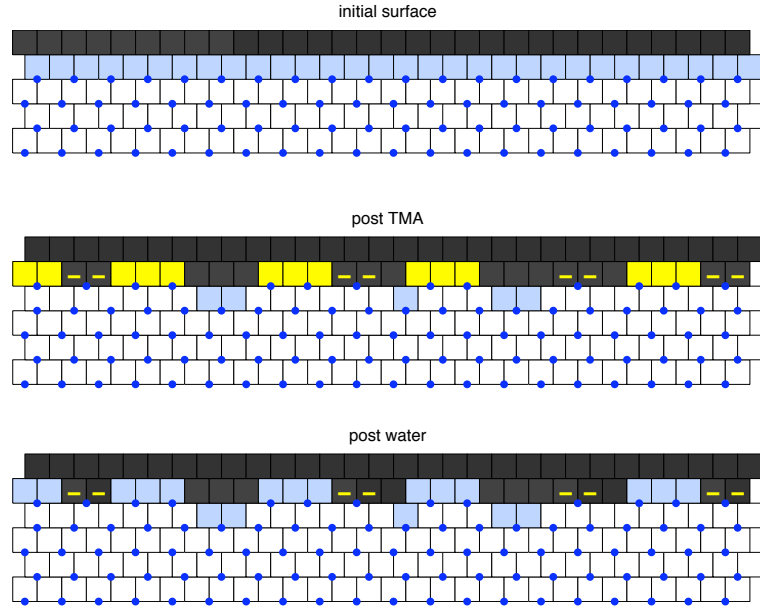


Figure 4.3: *Initial growth surface (top), after TMA exposure (middle), and then water (bottom).*

discussed previously, such a surface would correspond to an OH surface density of $16 \text{ OH groups/nm}^2$. While this appears high relative to reported values (with the exception of Elliott and Greer [26]), we will see that during ALD growth, this

value drops to a level more consistent with reported values. For example, [75] states that the greatest density with which methyl groups can pack the growth surface is 7.2 Me/nm^2 and typical saturation conditions are 70-80% of that.

4.7.1 TMA reactions on the lattice

As discussed, all cases involving TMA reactions with reactive species present on the alumina growth surface, the TMA molecule interacts with the lone electron pair of an exposed surface O or OH group to form a Lewis acid-base pair [100, 26]. Having adsorbed onto the surface in this manner, a number of subsequent reactions can take place. In the discussion that follows we will refer to sites adjacent to a reactive lattice site by the compass directions E, W, NE, NW, SE, and SW.

4.7.1.1 Ligand exchange reactions

In the first reaction R1 of Figure (4.4), a TMA molecule reacts with a single surface OH group, releasing one methane molecule and leaving two CH_3 ligands (yellow sites containing the letter L) bound to the newly deposited Al atom. Note that the hydroxyl group loses an H atom in the process, changing the site color from blue to white. The Al atom added by this reaction is represented as the filled blue circle; its position indicates it is covalently bonded to the O atom below and the two CH_3 ligands above in the NE, NW lattice positions for reaction R1a (and similarly for the other reactions). If there are additional vacant sites surrounding the OH group, each potential reaction is assigned equal probability of occurring.

The chemisorbed surface $\text{Al}(\text{CH}_3)_2$ species left by reaction R1 can undergo a second reaction with a neighboring surface OH leaving one surface CH_3 . The overall reaction is represented in Figure (4.4) as R2. Note that the two OH groups can be located on different lattice levels. After this reaction takes place, the Al atom deposited from the TMA molecule is bonded to the oxygen atoms from the two OH groups and the remaining methyl ligand. Again, if more than one reaction in R2 is possible, each reaction is assigned an equal reaction probability.

The single methyl group left by R2 can undergo yet another reaction with an available surface OH, leaving a surface Al bound to three O atoms. Likewise, one can view this reaction as one between a single TMA molecule and three neighboring surface OH groups. The oxygen bridge structures that result are denoted by the (-) symbols in reaction R3 of Figure (4.4). Note how a surface Al atom (represented by the filled blue circle) is produced by this reaction; it is bonded to the three O atoms located in the three lattice sites below the surface. It is argued in [22] that the reaction of TMA with three neighboring OH groups is thermodynamically favored over the other two partial reactions, and so our reaction model will assume this *irreversible* reaction sequence goes to completion whenever sufficient surface OH groups are present ¹. Additional details regarding the relative rates of the TMA reactions in sets R1 and R2 will be provided in the following section on the Monte Carlo simulation procedure.

¹The computations in [26] show reactions R2 and R3 to be energetically equivalent; however, the reactions can be considered irreversible because the product methane is swept away during the purge cycle, and so we conclude R3 will be favored over R2.

4.7.1.2 Dissociation reactions

The ligand exchange reaction R3 results in three oxygen bridges on the growth surface, each of which can participate in a reaction with an additional TMA molecule. The methyl transfer reactions are indicated as R4 of Figure (4.4). In our lattice-based reaction description, only one of the three Al-O bonds produced by R3 participate in this reaction because the remaining reaction sites are shielded from further reaction by the three CH_3 groups left by this reaction.

4.7.2 Water reaction

As described in [100], the water precursor molecules adsorb onto the growth surface by forming a Lewis acid-base complex with the Al atoms to which the surface CH_3 ligands are bound. The water then can dissociate, transferring an H atom to the CH_3 to release a methane molecule, leaving a surface OH group in its place. This simple reaction is the only water reaction considered in this study; we represent it in Figure (4.4) as R5, where a yellow methyl ligand cell is converted to a blue OH cell. We see that the Al atom involved remains unchanged in this reaction.

4.7.3 Monte Carlo simulation procedure

Having defined the lattice in which bulk and surface species are located and having enumerated the reactions that can take place between the gaseous precursor and surface species, we now complete the ALD model by “connecting” the gas phase to the growth surface processes. An important characteristic of this ALD

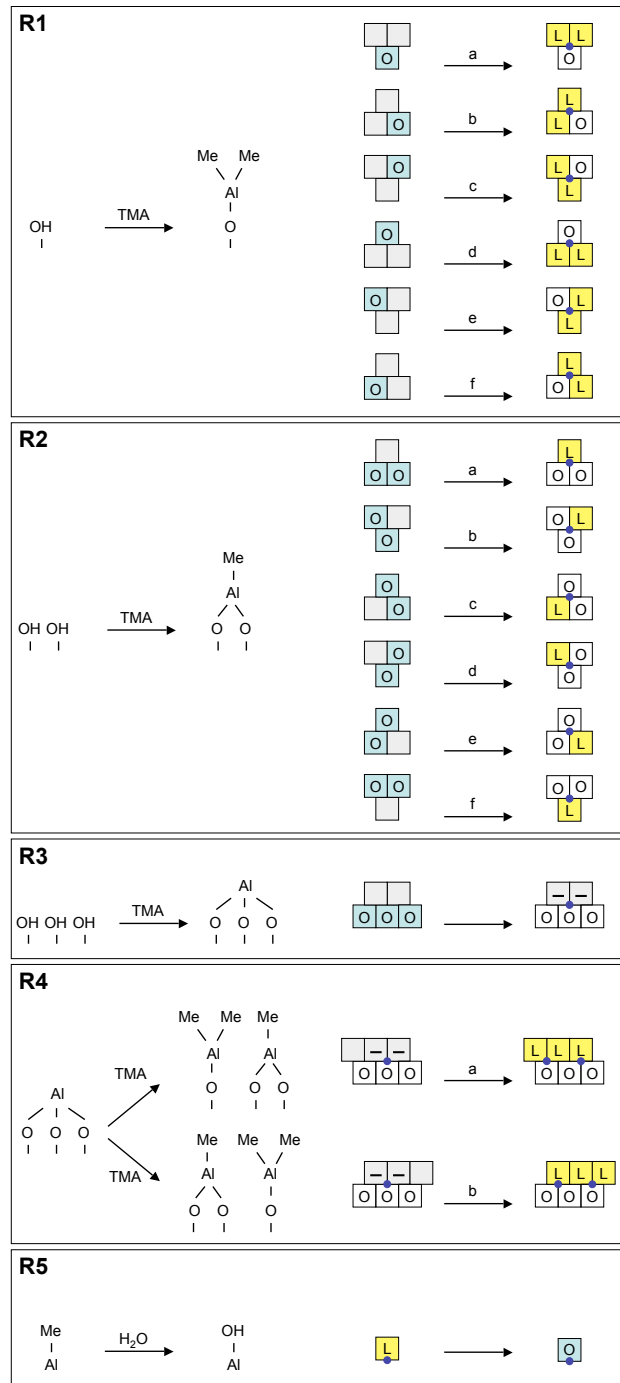


Figure 4.4: TMA (R1-R4) and water (R5) reactions and their representations on the lattice.

growth process is that other than the methyl transfer reaction (R4), no other surface diffusion processes take place [26]. Likewise, following [26] and consistent with the experimental observations of [22], we will assume that a fraction of TMA or water molecules bound to the growth surface as a Lewis acid-base adduct will always proceed to the reaction equilibrium state according to all feasible reactions at that site, and that the remainder desorb from the surface. Under these assumptions, we can define the total exposure of the alumina film to TMA (δ_A) and water (δ_W) as

$$\delta_A = \int_0^{\tau_A} p_A(t)dt \quad \text{and} \quad \delta_W = \int_0^{\tau_W} p_W(t)dt$$

where p_A and p_W are the partial pressure of the TMA and water, respectively, during each half-reaction exposure step, and τ_A and τ_W are the lengths of each exposure. This means that a surface exposed to 0.1 *Torr* TMA for 5 *sec* is equivalent to a 1 second exposure at 0.5 *Torr*.

4.7.4 The MC algorithm

Given the small number of collision events that actually result in a reaction, we will simulate only those events that either result in a reaction or that interact with the growth surface in such a way that no reaction is possible. Time, therefore, is scaled so as to eliminate all collision events between a precursor molecule and feasible reaction sites that do not result in a reaction. Though we call this procedure MC the kinetic aspect is inherent through our definition of, δ_A and δ_W were time τ_A, W is the total exposure time. We now define a Monte Carlo procedure consisting of the following steps:

1. During each exposure period, a total of J_A or J_W collision events are simulated, where the J_A and J_W are proportional to δ_A and δ_W , respectively. How this constant of proportionality is determined will be discussed in the following section.
2. During each event, a lattice column $m_{rxn} \in [1, \dots, M]$ is chosen using a uniformly distributed random number. In the chosen column m_{rxn} and starting at the top lattice site $s(N, m_{rxn})$, we proceed downwards through the lattice along column m_{rxn} until a potential reaction site is reached.
3. If the potential reaction site contains a hydroxyl group, the feasibility of reactions R1 to R3 are checked during TMA exposure. In this study, we will assume reaction R3 always takes place when it is feasible, a result consistent with the experimental observations of [22]. If more than one reaction from the combined sets of R1 and R2 is possible, each feasible reaction is identified and assigned probability ϕ if it is from set R1, $1 - \phi$ if from set R2. The sum of the probabilities of feasible reactions is normalized, and one reaction then is randomly selected from the weighted list. We set $\phi = 0.5$ for this study, unless otherwise noted.

If the reaction site contains a surface Al atom with three oxygen bridges, reaction R4 takes place. During the water exposure, a reaction between the water precursor and a surface methyl group takes place if the latter is found at the reaction site.

For the TMA reactions that leave one or more surface Me groups, we specify

the reaction only takes place if the local surface Me concentration is less than or equal to 7 Me groups per nm^2 after the reaction. This constraint is set by the steric hindrance effects of the Me at the growth surface and is enforced by limiting the local Me density ρ_{Me} . For this study, ρ_{Me} was computed by counting the total number of Me groups in a 7×7 box about the reaction site.

4. If a reaction takes place, the collision event index is increased by $j = j + 1$ and we continue the iteration process from step 2 until J_A or J_W events take place. If no reaction takes place, we continue down the same column m_{rxn} searching for potential reaction sites until the substrate is reached. Once it is reached, the iteration index j is increased and we proceed with step 2. Regardless of whether a reaction takes place, time is incremented with each iteration j . The time step size is determined from the experimentally measured reaction rates.

4.7.5 Initial film growth

In [22], an alumina nanoporous membrane was annealed at a temperature sufficiently high to promote crystallization of the substrate. The annealed alumina then was exposed to water for a period sufficient to generate a fully hydroxylated surface. We will model this substrate and initial growth surface with the lattice structure shown in Fig. 4.3, top.

In the ALD experiments of [22], the growth surface was subjected to low-pressure exposures of TMA and water. The low pressure resulted in film growth sufficiently slow that it could be observed with FTIR spectroscopy over the course

of several hundred seconds. We simulate the two experiments of the cited study, in which the fully hydroxylated growth surface was exposed first to TMA. In [22], the authors note that the FTIR signal corresponding to OH groups begins to drop immediately at the start of the TMA exposure cycle, while the CH₃ signal change is delayed. The authors attribute this observation to the initial reactions being those involving three OH groups (R3). As the surface OH groups are consumed, the CH₃ signal appears as a result of the R1, R2, and R4 reactions. Eventually, the reactions proceed to completion and no additional changes were observed in the experimental system after $t = 210$ s.

At the end of our simulated TMA exposure, we find the growth surface depicted in the middle of Fig. 4.3. A means of viewing the sequence of TMA reactions that lead to this surface is depicted in Fig 4.5. The perspective in this diagram is of looking down at snapshots of the growth surface, starting with the fully hydroxylated surface at $j = 1$ at the top, and then proceeding with the first three TMA reaction events, each involving three OH groups and leaving no surface Me, at MC iterations $j = 2, 3$, and 4. The first surface Me appear at $j = 11$ as a result of reaction R1; after that point, only reactions R1, R2, and R4 take place, all of which leave surface Me. Overall, this picture is consistent with the mechanism postulated by [22].

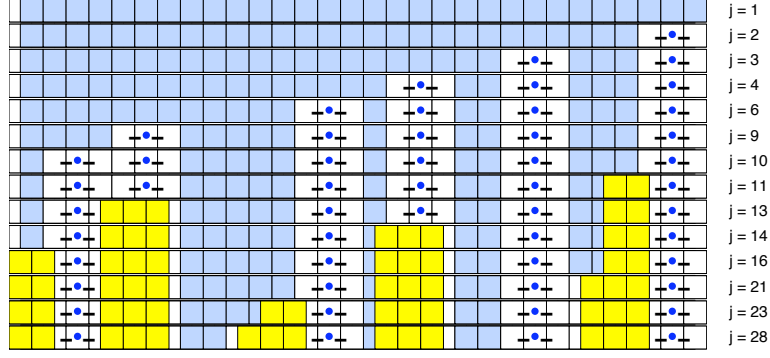


Figure 4.5: *Sequence of surface reactions taking place during the TMA exposure leading to the surface shown in Fig. 4.3, middle. Index j indicates the iteration number in the Monte Carlo simulation procedure.*

4.7.5.1 Initial TMA exposure

Given the fully hydroxylated surface shown in Fig. 4.3, top, we wish to determine the time interval Δt_A corresponding to each MC iteration and thus determine the total number of steps J_A required to span the $\tau_A = 210\text{ s}$ TMA exposure described in [22]. We note the time step size will be inversely proportional to the lattice size M . The most direct approach to determining the time step size Δt_A would be to estimate the **initial** dx_{OH}/dt from experimental data, where x_{OH} denotes the degree of normalized OH surface coverage (see the OH data of Fig. 4.6). At the outset of TMA exposure, the collision events corresponding to each MC iteration will take place at lattice locations containing contiguous OH groups and will occur with probability approaching unity. At this pace, it would take $J_A = M/3$ iterations to saturate the surface, and so we can compute

$$\Delta t_A = -\frac{3}{M[dx_A/dt]_{t=0}}. \quad (4.15)$$

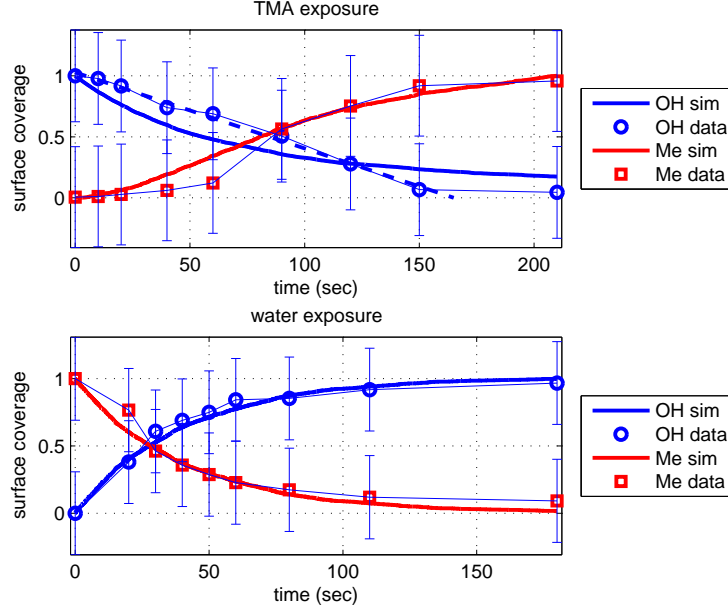


Figure 4.6: *Our simulation results compared to data taken from Figs. 5 and 7 of [22].*

As we have seen in Fig. 4.5, soon after the TMA reactions begin the other reactions (R1, R2, and R4) come into play, and so the depletion rate of surface OH groups slows, leading to a long exponential tail as the surface reactions approach saturation. As these other reactions take place, the surface Me concentration begins to grow, and then also approaches its equilibrium value. Both of these effects are seen in the simulation results plotted in Fig. 4.6. What is also apparent in these plots is an unusual behavior in the OH data during TMA exposure: the decrease in OH signal is virtually linear through the entire exposure cycle, suddenly stopping its downward trend at $t = 150$ s. This trend is shown by the dashed line fitted by regression to the first eight data points. Because this dynamic behavior cannot be described by the known surface reactions, we will choose our Δt_A based on a

reasonable fit to the Me data, rather than (4.15), resulting in the Δt_A we use in this paper as corresponding to $J_A = M$.

4.7.5.2 Water exposure

The single reaction (R5) that takes place during exposure of the growth surface to water suggests first-order reaction kinetics may be valid. Given the OH and Me surface coverages x_{OH} and x_{Me} , respectively, we can write

$$\frac{dx_{OH}}{dt} = \lambda_{OH}x_{OH} \quad \text{and} \quad \frac{dx_{Me}}{dt} = \lambda_{Me}x_{Me}. \quad (4.16)$$

At the start of the deposition cycle, a good approximation to (4.16) is

$$\frac{\Delta x_{OH}}{\Delta t_W} = \lambda_{OH}x_{OH} \quad \text{and} \quad \frac{\Delta x_{Me}}{\Delta t_W} = \lambda_{Me}x_{Me}$$

and so if $x_{OH} = m_{OH}/m_{OH}^o$ where m is the total number of surface OH groups at any time during the water exposure and the superscript o refers to the number at the start of the exposure cycle, the very first reaction corresponds to $\Delta m = 1$ giving

$$\Delta t_W = \frac{1}{\lambda m^o} \left(\frac{m^o}{M} \right) = \frac{1}{\lambda M}.$$

Note that we omit the Me and OH subscripts from the equation above to simplify notation. Using linear regression and the data from [22] we find

$$\lambda_{Me} = 0.021075s^{-1} \quad \lambda_{OH} = 0.026104s^{-1}$$

and so because they are close in magnitude, we average to find $\lambda = 0.023589s^{-1}$.

Using this eigenvalue to compute the step size and applying it in our simulation

gives the results shown in the bottom plot of Fig. 4.6. As can be seen in this Figure, the simulator does an excellent job of matching the observed dynamic behavior during the water exposure. A view of a section of the growth surface following 1 full TMA/water cycle can be seen in Fig. 4.3, bottom.

4.8 Film growth under iterated cycles

We now turn to the problem of simulating a long sequence of TMA and water exposure cycles². As a specific case we consider the experiments of [71], where nanoporous alumina membranes were exposed to 250 ALD cycles. In the cited study, both reactants were dosed at 0.5 Torr for 60 s , giving $\delta_A = \delta_W = 30\text{ Torr} \cdot \text{s}$ (c.f. the $\delta_A = 2.1\text{ Torr} \cdot \text{s}$ and $\delta_W = 1.8\text{ Torr} \cdot \text{s}$ used in the previous section). Given the relatively high exposure levels that we will now use, it is not surprising that our simulator shows that the growth surfaces quickly become saturated under the current growth conditions - as seen in Fig. 4.7, the TMA reaction is complete after approximately 20 s , while the water reaction takes only about 5 s to reach 100% conversion of all surface Me ligands.

4.8.1 GPC and other film growth measures

An important consideration at this point is how one extracts film properties such as thickness, surface roughness, and surface concentration from the lattice-based representation of the growing and potentially amorphous films. Film thick-

²We define a full ALD cycle as consisting of 1) exposure to TMA, 2) purge, 3) water exposure, and 4) purge.

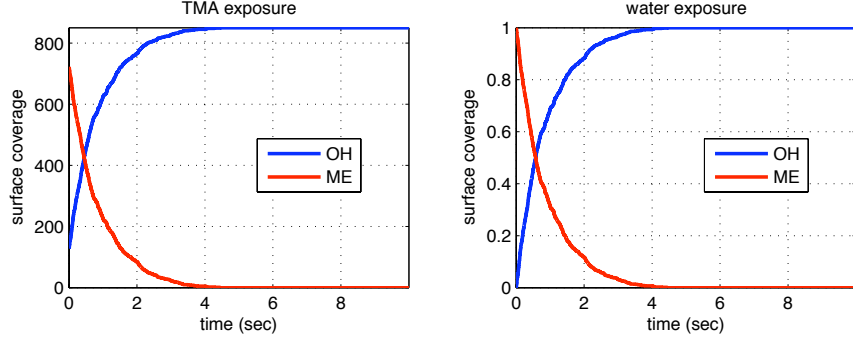


Figure 4.7: *Extent of reaction at 0.5 Torr exposure of TMA and water.*

ness can be measured directly with ellipsometry [71] or by the mass accumulation rate measured by a quartz crystal microbalance [57]. Translated into our simulation framework, these two thickness measurements result in two potentially different methods for calculating the growth per cycle (GPC) which we will refer to as GPC_T (GPC by direct thickness measurement) and GPC_M (GPC computed by mass accumulation). To start, we compute the local film thickness by scanning each column $m = 1, \dots, M$ of the lattice for the top-most location of a lattice site filled with an oxygen-containing component (either a bound oxygen atom or surface hydroxyl group); if the corresponding lattice location index is I_m , then the local film thickness is

$$T_m = (0.25nm)I_m \quad m = 1, \dots, M. \quad (4.17)$$

Surface roughness in [71] is defined by the root-mean-squared film thickness (we denote as σ). This quantity can be computed from the variance σ^2 of the vector defining the film thickness profile:

$$\sigma^2 = var(\mathbf{T}) \quad (4.18)$$

giving a measure of surface roughness consistent with that defined in [16].

The GPC is computed using the difference of the surface characteristics between the start of the k^{th} and $k+1^{th}$ (full) cycles. Denoting T^k and T^{k+1} as the mean of (4.17) at the start of two consecutive cycles gives the straightforward definition for GPC_T :

$$GPC_T = T^{k+1} - T^k. \quad (4.19)$$

Counting the total number of Al atoms n_A in the a lattice at the same points in time gives

$$GPC_M = (0.25 \text{ nm}) \frac{3(n_A^{k+1} - n_A^k)}{2M}. \quad (4.20)$$

Likewise, counting all the lattice sites occupied by O atoms and OH groups (n_O and n_{OH} , respectively), gives the film density at the start of cycle k as

$$\rho = (0.25 \text{ nm})(4 \text{ g/nm}^3) \frac{(n_O + n_{OH})}{MT^k}. \quad (4.21)$$

Finally, counting all the Me groups present in the s lattice after the TMA exposure and defining this value as n_L gives the surface Me density:

$$\rho_{Me} = \frac{n_L}{(0.25 \text{ nm})^2 M}. \quad (4.22)$$

Of course, this definition assumes all Me groups in the lattice are on the growth surface; in our simulation results we will find that this is a perfectly valid assumption under most conditions studied. A second issue with (4.22) is that it assumes a growth surface area that does not change from that of the perfectly flat substrate; this assumption will lead simulated surface Me concentrations that are higher than experimental observations when surface roughness becomes significant. Still, we

retain the definition (4.22) for this study because of its simplicity and clarity of meaning.

4.8.2 Representative film growth

As a simulation representative of the experiments of [71] we consider the case of 250 ALD cycles, each consisting of 20 s exposure to TMA followed by 10 s exposure to water, both at 0.5 Torr resulting in $\delta_A = 10$ and $\delta_W = 5$. We note that these exposure levels are consistent with [71] because in both cases, the half reactions go to completion (see Fig. 4.7). The simulation begins with the fully hydroxylated surface discussed in the previous section.

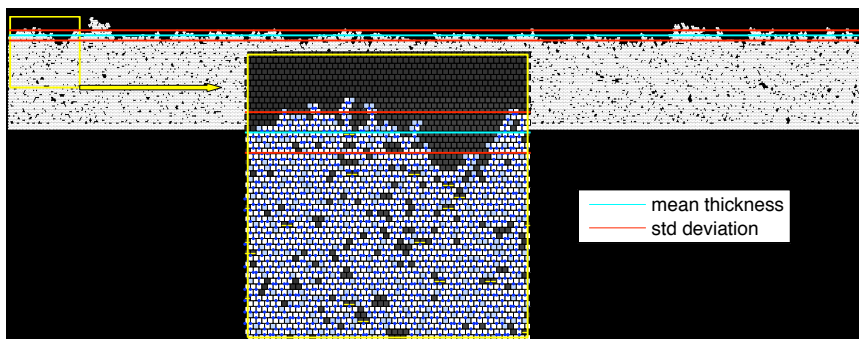


Figure 4.8: *Representative film after 250 full ALD cycles; in both the full-scale and magnified portion, the cyan line indicates the mean film thickness T^{250} and the red lines indicate the surface roughness as $T^{250} \pm \sigma$.*

The results of this simulation can be found in Figs. 4.8 through 4.10 and in Table 4.1. A portion of the film is shown in Fig. 4.8 where we clearly see an irregular structure with trapped OH groups and oxygen bridges, vacancies, and a complete lack of trapped Me, results that are all consistent with the observations of [22]. The

average film thickness is over 150 lattice elements (the average thickness is shown as the cyan line in Fig. 4.8) and because $M = 1500$, only a portion of the film is shown for clarity. The existence of voids within the film structure can be attributed to the two-dimensional nature of the lattice and the MC algorithm, expanding the lattice to three-dimensions will eliminate the voids.

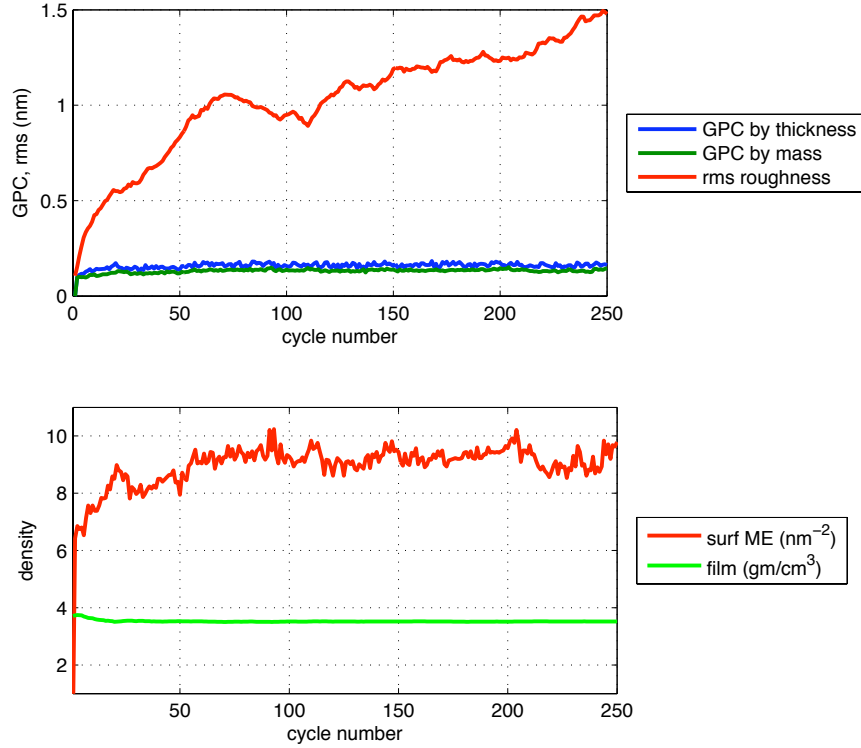


Figure 4.9: *ALD film properties as a function of exposure cycle number.*

Film properties as a function of cycle number are shown in Fig. 4.9. What is most striking about the evolution of surface properties is the range of rates: both GPC and film density equilibrate after only a few ALD cycles, while the surface Me and roughness σ feature much slower dynamics - it appears, in fact, that σ does not reach a steady mean value before the end of the 250 cycles simulated. It is not hard to understand that the dynamics of surface Me concentration are tied to the

changing roughness σ because of the increasing surface area that becomes available as σ increases (thus increasing the value n_L in eqn 4.22). The physical mechanism responsible for the growth of σ over these long time scales will be discussed later in this paper.

In Table 4.1, we summarize the film properties found after 250 ALD cycles: the model predictions of film density are exactly as expected, and ρ_{Me} is high, but that also is expected given the conservative estimate for surface area used in (4.22). Both GPC_T and GPC_M are higher than the expected value of $0.11nm/cycle$, leading to a total film thickness of $38.4nm$ as compared to the measured value of $27.0nm$ in [71]. While high, we argue that the simulator prediction is reasonable, given the lack of adjustable parameters in the model³.

Finally, it is interesting to observe the histogram of Fig. 4.10. In this figure, we see the domination of R1 and R2 relative to reactions R3 and R4. Within R1, we can observe a clear pattern of reaction frequency, where those reactions in which the vacant lattice sites are found above the reacting OH site (e.g., R1a, R1b, and R1f) are favored over those where the vacancies lie below the reactive OH lattice site. The same pattern emerges for R2, where reactions R2a, R2b, and R2d are favored over the remainder due to the vacant lattice site lying above the lowest reactive OH site. Finally, it is interesting to observe that R3 takes place with greater frequency than R4, an observation consistent with the buried surface oxygen bridges seen in Fig. 4.8.

³Because of the very high exposure levels, these simulations are effectively independent of J_A and J_W , the main adjustable parameters of the ALD model.

ϕ	T^{250} (nm)	σ (nm)	GPC_T (nm/cycle)	GPC_M (nm/cycle)	ρ_{Me} (nm ⁻²)	density (g/cm ³)
0.01	10.4	5.17	0.002	0.001	0.1	2.12
0.05	24.4	5.28	0.094	0.042	2.76	2.25
0.25	38.5	1.39	0.156	0.124	8.35	3.29
0.50	38.4	1.30	0.162	0.134	9.13	3.52
0.75	39.1	1.16	0.163	0.139	9.58	3.60
0.99	39.1	1.39	0.162	0.138	9.54	3.62

Table 4.1: *Effect of ϕ on film properties. All cases correspond to $\delta_A = 10$, $\delta_W = 5$, and 250 ALD cycles.*

4.8.3 Influence of ϕ

We recall that ϕ is the probability associated with each reaction of R1 and $1 - \phi$ corresponds to reactions in class R2. It is important to point out that ϕ only has an effect in situations where reactions from both sets R1 and R2 are possible - if feasible reactions consist solely of those from either R1 or R2, $0 < \phi < 1$ will have no effect because all of the reactions will have equal probability of taking place. If we first consider the limiting behavior of $0 < \phi \ll 1$, stronger preference will be given to reactions in R2 over R1 when reactions from both classes are possible. Under these circumstances, films with unusual morphology result: the films tend to develop a columnar nature, where the columns bend and intersect to form a highly porous film (see Fig. 4.11 for an example). Additionally, the film growth rate diminishes

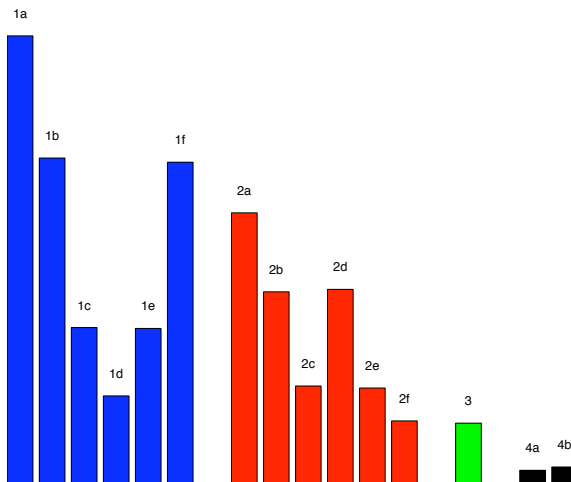


Figure 4.10: *Histogram of the frequency of each reaction in the overall deposition process.*

rapidly for small values of ϕ . The mechanism responsible for this behavior is simple: because $\phi \neq 0$, it is possible for an isolated OH group to react with TMA, leaving two free Me which are subsequently converted to two neighboring OH groups during the water exposure. Given the strong preference to reaction R2 in the subsequent TMA exposure, the overall pattern repeats because of the formation of an isolated Me group that is subsequently converted to OH during the water exposure.

Interestingly, data in Table 4.1 indicate little effect of ϕ in the range $0.25 < \phi < 1$. Furthermore, the structure of the film even at $\phi = 0.99$ is visually indistinguishable from the sample shown in Fig. 4.8. An immediate conclusion that can be drawn from these simulations is that if the true value of ϕ lies in this range, its exact value is unimportant and so the default choice of $\phi = 0.5$ is justified. A second conclusion worthy of further research is that the choice of $\phi \in (0, 0.25)$ may be used to tune the (currently high) GPC value to the commonly observed value of

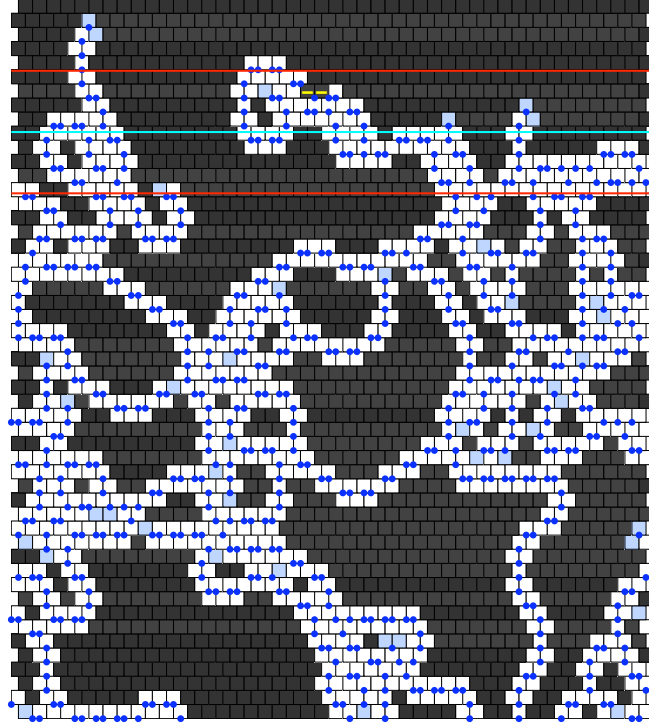


Figure 4.11: *A section of highly porous film that results for $\phi = 0.05$ ($R2$ favored over $R1$) and after 250 ALD cycles.*

0.11 nm/cycle. Given that $R2$ is thermodynamically favored over $R1$ (see Fig. 2 of [26]), this approach to improving the simulator's accuracy may be justified.

4.8.4 Sub-saturation experiments

We now examine the properties of films deposited during under-dosing conditions, where the growth surface is starved for one or both of the precursors. To establish the dose levels to be tested, consider the plots of Fig. 4.7; it can be observed in the left-side plot that during the TMA exposure period, half of the Me groups that are ultimately left on the growth surface after the system comes to equilibrium are deposited before $\tau = 2s$. Likewise, from the right plot we see that the half-way

point of full conversion of Me groups to OH during the water exposure cycle is found at the point in time when the Me and OH concentration curves cross - for this case at $\tau = 0.6s$. If we stop each of the half-cycles at these times, the resulting total exposure values are $\delta_A = 1$ and $\delta_W = 0.3$.

The conditions described above lead to four cases to be simulated: 1) full exposure to both precursors; 2) under-exposure to TMA; 3) under-exposure to water; and 4) under-exposure to both precursors. The results for 250 cycles under these conditions are listed in Table 4.2. From data in this table, we see that the growth rate drops by approximately half when the ALD process is starved for one of the precursors and that the growth rate shrinks further when the system is starved for both precursors.

Film density appears unaffected by under-dosing conditions, and there appear to be minor effects on film roughness. Overall, the results are consistent with what we would intuitively expect; likewise, they agree qualitatively with experimental observations, such as those presented in Fig. 2 of [71].

δ_A	δ_W	T^{250}	σ	GPC_T	GPC_M	ρ_{Me}	density
(Torr s)		(nm)	(nm)	(nm/cycle)	(nm/cycle)	(nm^{-2})	(g/cm^3)
10	5	38.4	1.30	0.162	0.134	9.13	3.52
1	5	23.4	1.28	0.097	0.084	5.77	3.55
10	0.3	19.9	1.35	0.086	0.071	14.38	3.51
1	0.3	14.5	1.12	0.057	0.050	9.08	3.52

Table 4.2: *Film properties for under-dosing simulations. In all cases $\phi = 0.5$.*

4.8.5 Stability of the ALD growth process

Returning to Fig. 4.9 and recalling how the surface roughness σ appeared to grow through all 250 ALD cycles, we now examine whether σ will grow indefinitely or if its mean will asymptotically approach an equilibrium value (as a function of cycle number). The mechanism leading to surface roughness is rooted in the nature of the surface reactions: as opposed to some thin-film growth processes (e.g., high temperature epitaxy), no surface diffusion takes place and so the random locations with which precursor molecules react with the growth surface gives rise to the roughening. A surface stabilizing mechanism, however, is created by the numerous TMA reactions taking place on the sloped growth surface (e.g., R1b, R2b, etc.) that have the effect of filling in local depressions in the growth surface. Given these two competing phenomena, the ultimate fate of the surface depends on whether equilibrium is achieved between these effects and whether this equilibrium is stable.

Because of the “filling-in” behavior described above, we expect high-frequency surface features (those spanning relatively few lattice sites) to change rapidly, and for longer wavelength features to evolve more slowly. A means of testing this effect can be had by simply changing M (recall our use of periodic boundary conditions), limiting the wavelength of the lowest-frequency surface features, and then observing the surface roughness dynamics.

As can be seen in Fig. 4.12, the surface roughness evolution does reach an equilibrium value for smaller values of M . As we might expect, the length of time

(number of ALD cycles) and the equilibrium value of σ both increase with M . We note that the curves in this Figure correspond to 3 data sets ($M = 15, 45, 90$), each of which corresponds to the average of 100 simulations, where each simulation consists of 750 ALD cycles. From these simulations, it is unclear if σ for $M = 90$ has reached equilibrium; this question and the general behavior of the system for large M is under investigation.



Figure 4.12: *Surface roughness as a function of cycle number illustrating the dependence on M . For all cases $\delta_A = 5$ and $\delta_W = 2.5$, and each curve is the average of 100 simulations.*

Chapter 5

Pore Transport

5.1 Overview

This chapter begins by giving a historical perspective on Knudsen diffusion discussing some experiments and theories that were conducted and discussed during the early parts of the last century. An analysis of the Knudsen number and its various regimes is described followed by a detailed derivation of the wall collision frequency number. Wall collision numbers for TMA and water are given and a derivation of the molecular flux equations is then presented. This is followed by a discussion of mass balance where the wall collision frequency number is incorporated into the molecular flux equation. This incorporated equation ends up being an ODE boundary value problem and a numerical technique is used where the ODE is discretized along the length of the pore via a collocation method. The system of equations that is generated is then solved using a Newton technique.

Knudsen was able to recognize and demonstrate the concept of diffuse emission from wall surfaces based on a cosine law [55]. The idea that when the mean free path of a gas is much larger than the characteristic apparatus length scale, intermolecular collisions are neglected and molecule wall collision dominate was nothing new during 1909. In 1883 Fleming was able to demonstrate the idea of molecular radiation from an Edison incandescent lamp. An Edison incandescent lamp consisted of a

horseshoe shaped carbon filament held together by copper clamps on platinum wire leads through the glass bulb [89]. When the copper clamps would fail the copper would vaporize and deposit inside the bulb leaving behind an area of no deposition shadowing the horseshow filament loop figure (5.1).

Knudsen developed an apparatus where a surface element is placed inside a spherical glass bulb and that element is vaporized covering the inside of the bulb uniformly. The distribution of the molecules inside the bulb followed the cosine law perfectly. This demonstration provided a basis for current technology as related to thin-film deposition and for the purposes of this work atomic layer deposition.

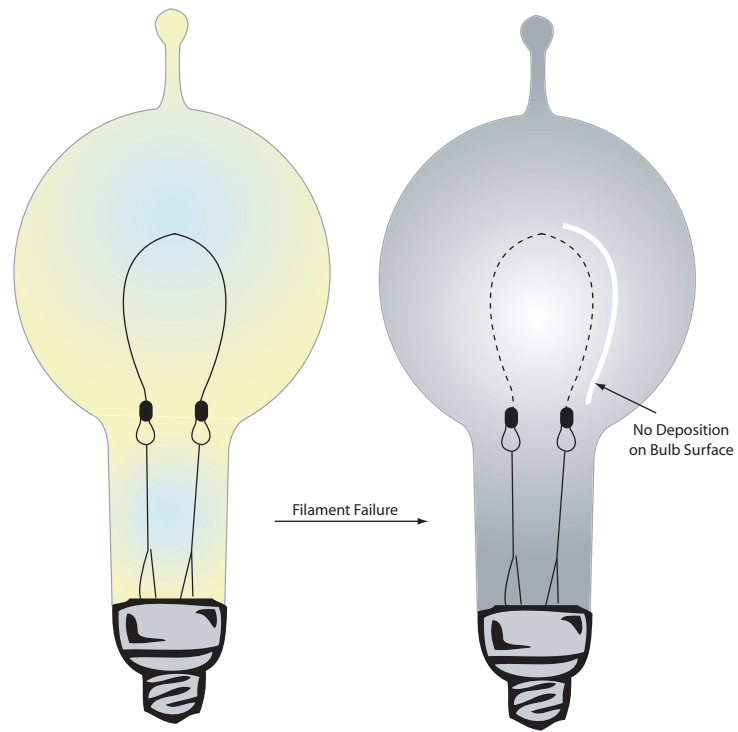


Figure 5.1: Early observation of distribution of filament vaporization

5.2 Knudsen Number

The Knudsen number is a dimensionless number that quantifies rarefaction and is defined as the ratio of the molecular mean-free path, λ , and a characteristic length, in the case of gas transport inside anodic aluminum oxide nanopores the characteristic length is the pore radius, r .

$$Kn = \frac{\lambda}{r} \quad (5.1)$$

with the mean-free path defined using kinetic theory as:

$$\lambda = \frac{k_b T}{\sqrt{2} \pi d^2 p} \quad (5.2)$$

k_b = Boltzmann Constant

T = Temperature

p = Pressure

d = Diameter of gas particle

The mean free path changes many orders of magnitude as a function of temperature and pressure for a particular gas. As an example, the mean free path of air in table (5.1) shows the magnitude change as a function of the vacuum range at room temperature.

The Knudsen number can be divided into four flow regimes:

1. $Kn < 0.01$
2. $0.01 < Kn < 0.1$
3. $0.10 < Kn < 3.0$

Vacuum Range	Pressure	λ
Ambient Pressure	1 atm	7×10^{-6} cm
Low Vacuum	1 torr	5×10^{-3} cm
Medium Vacuum	1 millitorr	5 cm
High Vacuum	10^{-6} torr	50 m
Ultra High Vacuum	10^{-9} torr	50 km

Table 5.1: Mean-free path values for air at room temperature and different pressures

4. $Kn > 3.0$

where each flow regime is modeled differently figure (5.2). The first flow regime is continuum flow where you have no rarefaction effects and gas flow can be modeled using Navier-Stokes equations in their common form. The second flow regime is the slip-flow regime where gas flow can be modeled using the Navier-Stokes equations with slip-flow boundary conditions. The third flow regime is transition flow and the flow is analyzed using the Boltamann equation. The fourth flow regime is free molecular flow where the gas is rarefied and intermolecular collisions an be neglected and this flow regime can be analyzed by modeling individual molecules. For a representative nanopore with pressure at 0.01 torr and pore diameter of 50 microns, we find the Knudsen number $Kn \approx 1000$ which clearly indicates that the gas is rarefied and molecule wall collisions dominate.

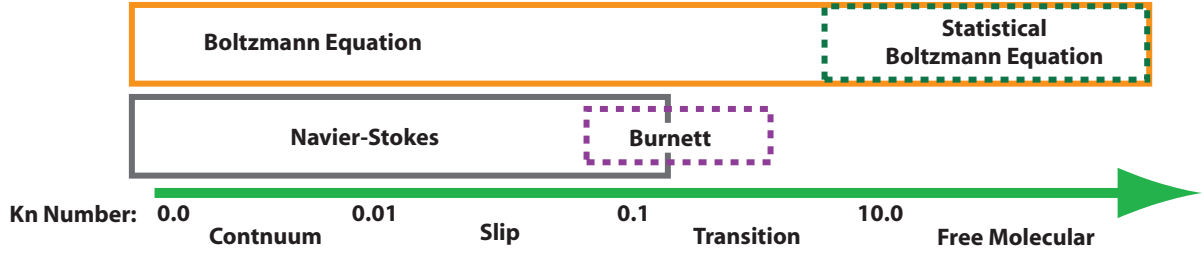


Figure 5.2: Modeling approach for different Knudsen Numbers [78]

5.3 Wall Collision Number

As mentioned when the Knudsen number is greater than 3, gas is considered rarefied and surface collisions dominate. These surface collisions have a potential to undergo a chemical reaction if the chemistries are correct. It is therefore important to determine the number of molecules that collide with a surface. The derivation is based on the kinetic theory of gases which has the following assumptions [84]:

1. In a gas there is a large number of molecules and the mean free path of the molecules is much greater than a characteristic length meaning the molecular ensemble occupies a negligible volume and there behavior is treated statistically.
2. The molecular ensemble has a wide distribution of speeds and can move in any direction with equal probability.
3. The collisions between a molecule and wall are elastic.
4. The individual molecules in the molecular ensemble are considered identical.

We begin our derivation by first assuming that there is a portion of a surface that has a collision area, A . We will consider this area to be a plane. We also consider a molecule that has a velocity v . Furthermore, this molecule for the purposes of flow through a cylindrical pore in the z -direction has a component velocity v_z normal to A . During a time interval Δt the molecule travels a length $v_z \Delta t$. If we assume that the molecule will collide with the surface within $v_z \Delta t$ in time Δt then this length multiplied by the collision area will give volume, $Av_z \Delta t$. If we define the number density n of the gas as N/V then the number of molecules of the gas contained in the volume $Av_z \Delta t$ is:

$$nAv_z \Delta t \quad (5.3)$$

The velocity of the gas follows a velocity probability distribution, $f(v_z)$ and thus the total number of molecules that collide, Z , with a surface area during a time interval:

$$Z = nA\Delta t \int_0^\infty v_z f(v_z) dv_z \quad (5.4)$$

We can relate the change in momentum, Δp , during a collision by applying an assumption of the kinetic theory of gases that the molecule collides with the surface elastically. In elastic collision the velocity of the molecule is conserved but the direction of the molecule is reversed after the collision. Thus the total momentum lost by all colliding particles and gained by the wall is two times the initial momentum.

$$\Delta p = Z(2mv_z) \quad (5.5)$$

therefore:

$$\Delta p = 2mnA\Delta t \int_0^\infty v_z^2 f(v_z) dv_z \quad (5.6)$$

The microscopic state, momentum, can be related to the macroscopic state, pressure, by the relationship:

$$P = \frac{\Delta p}{A\Delta t} = 2mn \int_0^\infty v_z^2 f(v_z) dv_z \quad (5.7)$$

We can apply a further simplification by introducing the mean-square speed of the molecules $\langle v_z^2 \rangle$, by using the following relationship:

$$\langle v_z^2 \rangle = \int_0^\infty v_z^2 f(v_z) dv_z = \frac{1}{2} \int_{-\infty}^\infty v_z^2 f(v_z) dv_z \quad (5.8)$$

$$P = mn \langle v_z^2 \rangle \quad (5.9)$$

Rewriting pressure using the ideal gas law and number density in terms of number of moles and Avogadro's number

$$\frac{nRT}{V} = m \frac{nN_A}{V} \langle v_z^2 \rangle \quad (5.10)$$

canceling volume, moles and merging mass and Avagadro's number to attain molecular mass we arrive at a relationship that links speed of a molecule to mass and temperture:

$$\frac{RT}{M} = \langle v_z^2 \rangle \quad (5.11)$$

By using the second assumption of the kinetic theory of gases and utilizing the Pythagorean theorem relating the square of the velocity to the square of its components we realize that the average component velocities are equivalent and thus:

$$\langle v^2 \rangle = \langle v_x^2 \rangle + \langle v_y^2 \rangle + \langle v_z^2 \rangle = 3 \langle v_z^2 \rangle \quad (5.12)$$

accordingly arriving at the relation for the velocity root mean square, v_{RMS} :

$$\langle v^2 \rangle = \frac{3RT}{M} \rightarrow v_{RMS} = \sqrt{\frac{3RT}{M}} \quad (5.13)$$

To determine the actual velocity distribution, $f(v_z)$, we create a distribution function $F(v)$, which is equivalent to the product of the distribution of the component velocities, $f(v_i)$ where $i = x, y$ or z .

$$F(v_x, v_y, v_z)dv_x dv_y dv_z = F(v)dv \quad (5.14)$$

where

$$F(v)dv = f(v_x)dv_x f(v_y)dv_y f(v_z)dv_z \quad (5.15)$$

We take the derivative of equation (5.15) with respect to a component velocity, v_i and exercising the chain rule:

$$\frac{\partial F}{\partial v_i} = \frac{dF}{dv} \frac{\partial v}{\partial v_i} = \frac{dF}{dv} \frac{\partial}{\partial v_i} \sqrt{v_x^2 + v_y^2 + v_z^2} = \frac{dF}{dv} \frac{v_i}{v} \quad (5.16)$$

Substituting for the definition for F :

$$\frac{1}{v_i} \frac{\partial}{\partial v_i} (f(v_x)f(v_y)f(v_z)) = \frac{1}{v} \frac{dF}{dv} \quad (5.17)$$

Because the component partial derivatives all equate to the same term we can equate the left hand side of equation (5.17) to some constant. For convenience, the constant equates to $-k$:

$$\frac{f(v_y)f(v_z)}{v_x} \frac{\partial f(v_x)}{\partial v_x} = \frac{f(v_x)f(v_z)}{v_y} \frac{\partial f(v_y)}{\partial v_y} = \frac{f(v_x)f(v_y)}{v_z} \frac{\partial f(v_z)}{\partial v_z} = -k \quad (5.18)$$

Dividing equation (5.18) by the definition of F , results in a separable, first order differential equation:

$$\frac{1}{f(v_i)v_i} \frac{\partial f(v_i)}{\partial v_i} = -k \quad (5.19)$$

Which can be rewritten as:

$$\frac{\partial f(v_i)}{f(v_i)} = -kv_i dv_i \quad (5.20)$$

Integrating both sides:

$$f(v_i) = I e^{-kv_i^2/2} \quad (5.21)$$

The integrating constant, I , can be determined by realizing that the integral of the probability distribution over the entire region of space is equal to 1:

$$\int_{-\infty}^{\infty} f(v_i) dv_i = I \int_{-\infty}^{\infty} e^{-kv_i^2/2} dv_i = 1 \quad (5.22)$$

The solution is obtained by realizing that the integral has a gaussian form and thus has the following solution:

$$\int_{-\infty}^{\infty} e^{-cx^2} = \frac{\sqrt{\pi}}{\sqrt{c}} \quad (5.23)$$

resulting:

$$I \sqrt{\frac{2\pi}{k}} = 1 \rightarrow I = \sqrt{\frac{k}{2\pi}} \quad (5.24)$$

Substituting into equation (5.21):

$$f(v_i) = \sqrt{\frac{k}{2\pi}} e^{-kv_i^2/2} \quad (5.25)$$

The value of k is determined by looking at equation (5.13), we introduce the Boltzmann constant:

$$k_B = \frac{R}{N_A} \rightarrow \langle v^2 \rangle = \frac{3k_B T}{m} \quad (5.26)$$

We introduce the kinetic energy:

$$\langle E \rangle = \frac{m \langle v^2 \rangle}{2} = \frac{3k_B T}{2} \quad (5.27)$$

If we apply equation (5.15):

$$F(\mathbf{v}) = f(v_x)f(v_y)f(v_z)$$

and substitute equation (5.25):

$$F(v) = \left(\frac{k}{2\pi}\right)^{3/2} \prod_{i=x,y,z} e^{-kv_i^2/2} \quad (5.28)$$

Substituting equation (5.28) into equation (5.27):

$$\langle E \rangle = \frac{3mk^{3/2}}{2(2\pi)^{3/2}} \prod_{i=x,y,z} \int_{-\infty}^{\infty} v_i^2 e^{-kv_i^2/2} dv_i \quad (5.29)$$

Simplify using equation (5.23):

$$\langle E \rangle = \frac{3m}{2k} \quad (5.30)$$

substituting in equation (5.27) and solving for k:

$$k = \frac{m}{k_B T} \quad (5.31)$$

We arrive at the final form of the velocity distribution, this distribution is known as the Maxwell-Boltzmann velocity distribution:

$$f(v_i) = \left(\frac{m}{2\pi k_B T}\right)^{1/2} e^{-mv_i^2/2k_B T} \quad (5.32)$$

By substituting this velocity distribution into equation (5.4) and integrating, we obtain an expression for the frequency of molecular bombardments per unit area time:

$$Z = \frac{1}{4} n \sqrt{\frac{8k_B T}{\pi m}} \quad (5.33)$$

If molecular collisions with the surface result in a reaction, then it is more convenient to express the wall collision number in terms of partial pressure. As we have noted $n = N/V =$ molar density or concentration, C , and through ideal gas the partial pressure, p_i , where i is either TMA or water is related to concentration through

$p_i = C_i RT$. As the gas diffuses along the length of the pore, and if molecular bombardments with the pore surface results in a reaction the partial pressure of the gas will vary along the length of the pore therefore the partial pressure of the gas is a function of both the discrete length, s and time, t where $p_i = p(s, t)$ we can express the wall collision number with the partial pressure through this relationship and write:

$$Z = \frac{1}{4} \frac{p_i}{RT} \sqrt{\frac{8kT}{\pi m}} \quad (5.34)$$

Thus the wall collision number per unit area time is function of the partial pressure $Z(p_i)$.

5.4 Wall Collision Number of TMA and Water

The system of interest in this work is of the deposition of aluminum oxide via atomic layer deposition of trimethyl aluminum and water. Based on reactor condition presented [22] of $P = 0.01$ Torr, monomer pressure $P_o = 760$ Torr and $T = 500$ K we arrive at:

$$Z_{TMA} = 1.85 \times 10^4 \frac{\text{molecules}}{\text{sec nm}^2}$$

$$Z_{Water} = 3.70 \times 10^4 \frac{\text{molecules}}{\text{sec nm}^2}.$$

5.5 Distribution of Molecules Post Collision

In the previous section, we calculated the wall collision frequency of molecules based on a Maxwell velocity distribution in the Knudsen regime. We are now interested in the dynamics of the molecules after they collide with a wall.

5.5.1 Macrostates and Microstates

When understanding the dynamics of an ensemble of molecules the concept of a state needs to be understood. If we assume that the dynamics of the molecules are constrained in an isolated system, where neither energy nor work is exchanged with its surroundings we can arrive at the following definitions for a macrostate and a microstate [54, 58]:

Definition 1

Macrostate: In classical thermodynamics, a macrostate of a gas system is described by thermodynamic variables such as pressure, volume, and energy. The values of these variable are the concerted behavior of i molecules in a gas system there are three important properties of a macrostate:

- 1. A macrostate represents the overall behavior of the system*
- 2. Some macrostate properties, N , remain constant, such as pressure or temperature.*
- 3. Not all macrostate properties are fixed, for example in a given volume the number of molecules in a specific location can change, i.e. during diffusion processes. These free macrostates are defined as, $\{\alpha\}$.*

Definition 2

Microstate: If there exists i molecules in a gas system the discrete property of each molecule specifies the gas system. For gas molecules the properties of interest are position and momentum. For an isolated system many microstates can exist. Take

for example the spin state of individual atoms in the system, where the microstate is the spin orientation of an atom having either \uparrow or \downarrow spin where \uparrow or \downarrow is equally probable. If we consider a checkerboard where each square of the board is an atom with a random spin orientation the configuration of this board represents a microstate. Due to the randomness in the spin orientation, there are many unique configurations for the checkerboard. Each of these unique configurations is a unique microstate.

Statistical mechanics provides a bridge between macrostates and microstates. Based on the above definitions, we can state that for any macrostate there are many complementary microstates. The number of different microstates corresponding to a macrostate is called the weight of the macrostate and is expressed as $\Omega = \Omega(N, \{\alpha\})$. For a given macrostate all microstates are equally probable.

5.5.2 Second Law of Thermodynamics

We take the concept of the microstate further through entropy. Entropy, S , is a measure of randomness or more precisely the spread of energy. When a system instantaneously changes out of equilibrium entropy increases as does the randomness in the system. Similarly, if we take a look at Ω , if a system instantaneously changes out of equilibrium the system will proceed towards a maximum value of Ω where $\Omega = \Omega(N, \{\alpha\})$. A connection between S and Ω is further made if we consider two isolated systems. The total entropy of the isolated systems, $S_{tot} = S_1 + S_2$, while the total number of microstates, $\Omega_{total} = \Omega_1 \Omega_2$. Based on the above arguments Boltzmann

[54] concluded that the entropy of a thermodynamic system at equilibrium is:

$$S = k_B \ln \Omega \quad (5.35)$$

This is called the statistical second law of thermodynamics or Boltzman's entropy, and a consequence of this statement is that systems evolve towards equilibrium because equilibrium is the most likely state.

5.5.3 Detailed Balance

In an equilibrium state [17, 39, 65] surmised that if a process is at equilibrium then the reverse process is equally likely. This concept is known as a detailed balance and is defined as:

$$\gamma_{mn} P_m = \gamma_{nm} P_n \quad (5.36)$$

where γ_{ij} is the transition probability from state i to state j and P_i is the probability of the system in state i [98]. The concept of a detailed balance as argued by [17] can be illustrated figure (5.3), where we define particle states A and B and we define reverse states A_r and B_r . States A and A_r and states B and B_r possess the exact same properties except for a reversal in momentum. If we apply the detailed balance in terms of number particles per second, N , that transition from one state to another and apply the definition of an equilibrium state we arrive at the following relationship:

$$N(A \rightarrow B) = N(B_r \rightarrow A_r) \quad (5.37)$$

where the number of particles that transition from A to B is equivalent to the number of particles that transition from A_r to B_r . Furthermore, the particles that

collide with a surface is proportional to $\cos(\theta)$ [17, 39, 54, 62, 98, 99] and thus based on detailed balance the scattered particles have a distribution proportional to $\cos(\theta)$.

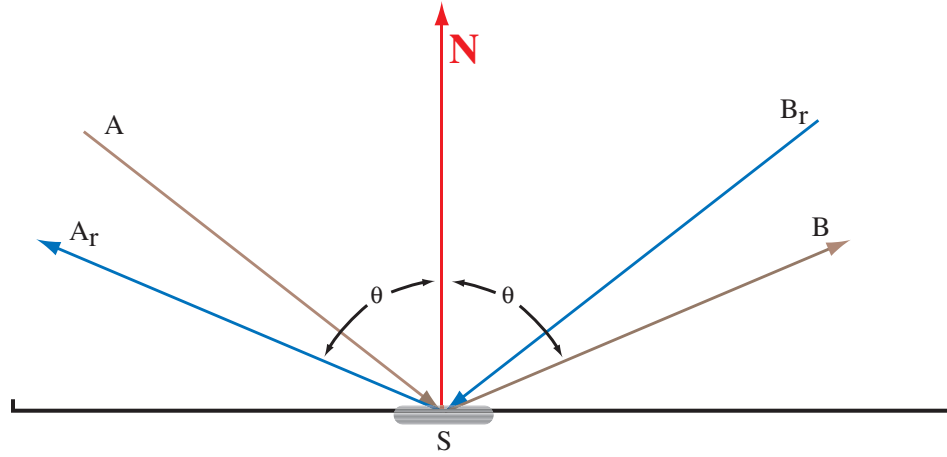


Figure 5.3: Detailed balance using Knudsen argument [99]

5.5.4 Second Derivation of Cosine Distribution

The above argument assumes that the number of particles that collide with a surface is equivalent to the number of particles that scatter after a surface event and that the probability of finding a particle in state A is equivalent in finding a particle in state A_r which can be false if surface reactions take place. A better argument of the scattering event following a cosine distribution [64] begins by considering a closed area C figure (5.4.left) within which there exists two differential surface elements A and B forming part of the boundary of C . The distance of A and B based on a local coordinate system with an origin at O has distances of d_1 and d_2 . The distance between A and B is L . Over some time a number of molecules strike A isotropically which we call an incoming molecular flux to A , F^i . A contribution to the incoming molecular flux is from surface element B . A straight line connecting A and B forms an angle relative to a normal at d_1 or d_2 which we call θ_A or θ_B . The outgoing flux from A or B is designated as F_o and is a function of distance from the origin and θ , $F_o(d_{1,2}, \theta_{A,B})$. We define a solid angle from A subtended by surface element B as figure (5.4.middle):

$$\Omega_B = \frac{B \cos(\theta_B)}{L^2} \quad (5.38)$$

We define a solid angle from B subtended by surface element A as figure (5.4.right)

$$\Omega_A = \frac{A \cos(\theta_A)}{L^2} \quad (5.39)$$

The flux of molecules striking B from A is:

$$F_{A \rightarrow B}^i = F_o(d_1, \theta_A) A \Omega_B = F_o(d_1, \theta_A) A \frac{B \cos(\theta_B)}{L^2} \quad (5.40)$$

The flux of molecules striking A from B is:

$$F_{B \rightarrow A}^i = F_o(d_2, \theta_B) B \Omega_A = F_o(d_2, \theta_B) B \frac{A \cos(\theta_A)}{L^2} \quad (5.41)$$

Applying the argument of isotropy and homogeneity requires $F_{A \rightarrow B}^i$ to be equivalent to $F_{B \rightarrow A}^i$. Because the terms are functions of different independent quantities the terms are equivalent to a constant:

$$\frac{F_o(d_1, \theta_A)}{\cos \theta_A} = \frac{F_o(d_2, \theta_B)}{\cos \theta_B} = \kappa. \quad (5.42)$$

and thus the outgoing flux is independent of location:

$$F_o = \kappa \cos(\theta) \quad (5.43)$$

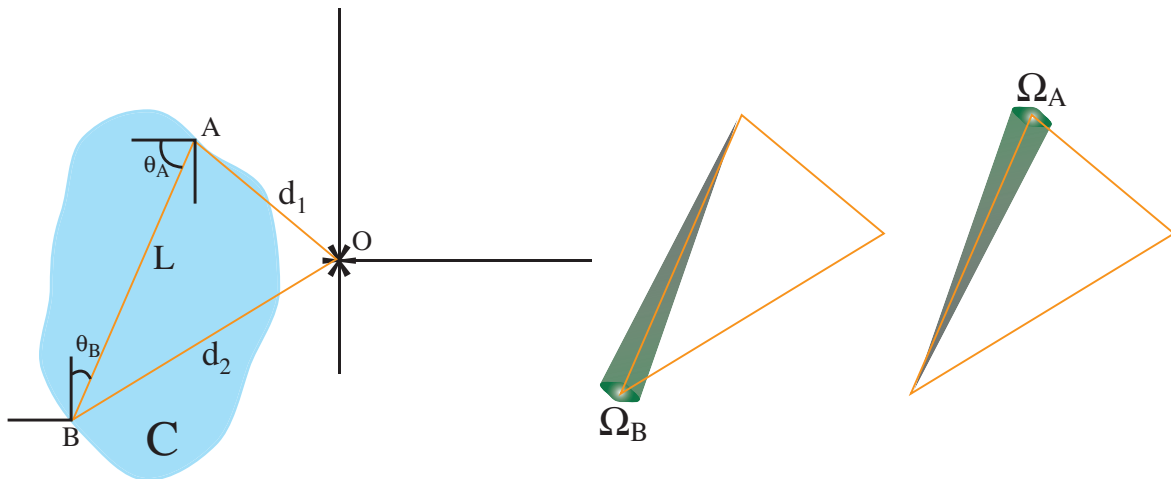


Figure 5.4: Second argument for Cosine Distribution

5.6 Flux Derivation

Based on the Knudsen number from the previous section for TMA and water and the characteristic length of the nanopore, we can treat our precursor gases as being highly rarefied. Here intermolecular collisions can be neglected and the molecules are engaged in an operation of random walks and statistical change of directions with the pore surface due to wall collision events. Thus, a transport diffusion occurs in a non-equilibrium state where a particle diffuses from one side of the pore to the opposite side under a concentration gradient and therefore, a chemical potential.

For transport diffusion, the general relationship for flux is followed as:

$$\text{Flux} = (\text{Particle Mobility}) * (\text{Driving Force})$$

The particle mobility describes the mobility of a diffusing particle in a media and has larger values for gases and smaller values for liquids. Particle mobility is referred to as the diffusivity, D and has units:

$$D = \frac{\text{distance}^2}{\text{time}}$$

The driving force for diffusion related transport is the existence of a concentration gradient. Gradient is the variation of a property, concentration, pressure, number of moles, as a function of distance. Ultimately we want to model the gas dynamics inside a nanopore by taking into account the flux of gasses and the collision of these gases with the pore walls. Collisions with pore wall was discussed earlier we now present a model of the gas transport.

We begin by considering a volume element figure 5.5 inside a nanopore that has cross sectional area πr^2 and thickness ΔS . We first consider the gas entering one side of this volume element. The mass transport of these molecules is called the flux, J and is proportional to the molecular density of the gas and mean velocity of gas, v . For a rarefied gas the flux of the molecules is a function of the wall

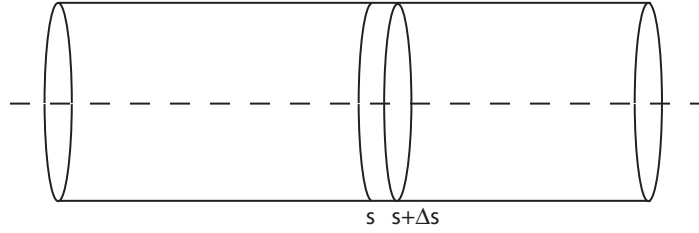


Figure 5.5: Differential Volume

collision number. As a molecule strikes a wall the outgoing flux of the molecules follows a cosine distribution, thus during diffusion the location of the molecules is not fixed and thus is a free macrostate. The location of the molecules as mentioned above is based on a detailed balance where a molecule changes states based on a transition probability. The transition probability during a diffusion event is the probability that a molecule entering a volume element proceeds through the volume element without returning to its original location. The transition probability is a function of the volume geometry, i.e. long circular cylinder. As the mass transport of the molecules moves across the surface area of the volume element the flux is then equivalent to:

$$J = wAZ \quad (5.44)$$

J = Molecular flux [molecules/ l^2t]

Z = Wall collision number

A = cross sectional area

w = Dimensionless transition factor

for a cylinder the cross sectional area is πr^2 where r is the radius of the cylinder.

The radius is a function of the cylindrical axial position by substituting for the wall collision number equation (5.33) where the number density is also a function of the axial position the flux entering the differential element at s becomes:

$$J_s = \frac{1}{4} w \pi r_s^2 \sqrt{\frac{8k_B T}{\pi m}} n_s \quad (5.45)$$

and the flux existing the differential element at $s + \Delta s$ is:

$$J_{s+\Delta s} = \frac{1}{4} w \pi r_{s+\Delta s}^2 \sqrt{\frac{8k_B T}{\pi m}} n_{s+\Delta s} \quad (5.46)$$

The net flux across the volume element is the change in flux across the volume element

$$J_{net} = \frac{1}{4} \pi r_s^2 w \sqrt{\frac{8k_B T}{\pi m}} (n_{s+\Delta s} - n_s) \quad (5.47)$$

for a long straight tube the transition probability is [17]:

$$w_{cylinder} = \frac{8r(s)}{3\Delta s} \quad (5.48)$$

Substituting and re-writing the change in number density as Δn

$$J_{net} = \frac{1}{4} \pi r_s^2 \frac{8r(s)}{3} \sqrt{\frac{8k_B T}{\pi m}} \frac{\Delta n}{\Delta s} \quad (5.49)$$

simplifying and writing in differential form by taking the limit as $\Delta s \rightarrow 0$:

$$J_{net} = \pi r_s^2 \left(\frac{2}{3} r(s)\right) \sqrt{\frac{8k_B T}{\pi m}} \frac{dn}{ds} \quad (5.50)$$

If we consider the flux to be in moles not molecules, and consider the rate of change of gas concentration rather than molecular concentration the flux, or net change in the mole number of molecules per unit time, becomes:

$$J_{net} = \pi r(s)^2 \left(\frac{2}{3}r(s)\right) \sqrt{\frac{8k_B T}{\pi m}} \frac{dc}{ds} \quad (5.51)$$

If we implement the definition of diffusivity with D begin equivalent to:

$$D = \left(\frac{2}{3}r(s)\right) \sqrt{\frac{8k_B T}{\pi m}} \quad (5.52)$$

and the flux can be written as:

$$J_{net} = -\pi r(s)^2 D \frac{dc}{ds} \quad (5.53)$$

The negative sign is due to the fact that molecular flow occurs from regions of higher concentrations to regions of lower concentration. The above equation is known as Fick's first law. In terms of partial pressure of individual species equation (5.53) can be written as:

$$J_{net} = -\frac{\pi r(s)^2}{RT} D \frac{dp_i}{ds} \quad (5.54)$$

5.7 Knudsen Diffusion

We now consider the transport of species, TMA or water, across a cylindrical pore by applying a species balance over a differential area. We define a pore with dimensionless axial coordinates $0 \leq s \leq 1$, where 0 and 1 are the pore mouths figure (5.6). The precursor accumulation rate over time t , $0 \leq t \leq \tau$ per pore cross sectional area is:

$$\frac{\pi r(s, t)^2}{RT} \frac{\partial p_i}{\partial \tau} \quad (5.55)$$

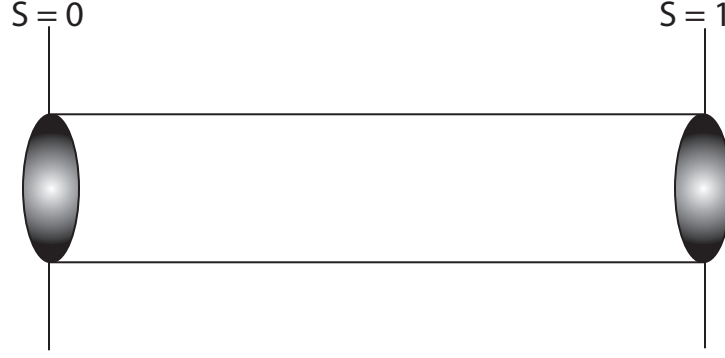


Figure 5.6: Constituent nanopore with dimensionless axial coordinates

which is equivalent to the species flux per pore cross sectional area over the length of the pore and time:

$$\frac{\partial}{\partial s} \frac{\pi r(s, t)^2}{RT} D \frac{\partial p_i}{\partial s} \quad (5.56)$$

and the consumption of the species within the pore cross sectional area over the length of the pore and time:

$$\pi r(s, t)^2 \Gamma(p_i, s) \quad (5.57)$$

where Γ is the instantaneous rate of consumption of the species. Thus the complete material balance across the pore using equations (5.55, 5.56, 5.57):

$$\frac{\pi r(s, t)^2}{RT} \frac{\partial p_i}{\partial \tau} = \frac{\partial}{\partial s} \frac{\pi r(s, t)^2}{RT} D \frac{\partial p_i}{\partial s} - \pi r(s, t)^2 \Gamma(p_i, s) \quad (5.58)$$

We apply a simplification by realizing that ALD is a cyclical process, and to average the complete Knudsen diffusion over the species (half) cycle, giving a local precursor dosage $\delta_i(s)$ as a function of spatial position along the pore:

$$\delta_i(s) = \int_0^{\tau_i} p_i(s, t) dt \quad (5.59)$$

$$C_i(\delta_i(s)) = \int_0^{\tau_i} \Gamma_i(p_i(s, t)) dt \quad (5.60)$$

The resulting ODE boundary value problem, subject to a specified exposure level at each end of the pore is given by:

$$\frac{d}{ds}\left(\frac{r(s)^2}{RT}D\right)\frac{d\delta_i}{ds} - \pi r(s)^2 C_i(\delta_i(s)) = 0 \quad (5.61)$$

Subject to pore entrance boundary conditions

B.C. 1

$$\delta_i(0) = \delta_i^0$$

B.C. 2

$$\delta_i(1) = \delta_i^1$$

and the update to the deposition thickness profile after each full deposition cycle with n = cycle number:

$$r^n(s) = r^{n-1} + GPC^{n-1}(s) \quad (5.62)$$

5.8 Review of Knudsen Transport Models

There are multiple models available to study the transport of rarefied gas at high Knudsen numbers the following section provides a brief historical review of expressions as related to rarefied flows through long tubes. The important distinction between the different models is the treatment of particles after a collision. The treatment of particles post-collision is determined by a scattering kernel. The scattering kernel is a probabilistic function that describes the episode of a particle that collides with a wall at some position x and velocity v_{in} and after some time $t = \tau$ resurfaces at relatively the same x but with velocity v_{out} . If we consider the entire

time domain the kernel can be written as:

$$W(v_{in} \rightarrow v_{out}; x, t) = \int_0^\infty W(v_{in} \rightarrow v_{out}; x, t, \tau) d\tau \quad (5.63)$$

Some of those models that are currently in place include:

1. Knudsen Description
2. Clousing Integral
3. Random Billiard Model
4. Kinetic Transport and Reaction Model (KTRM)
5. Ballistic Transport and Reaction Model (BTRM)

we give a brief treatment of each of these methods followed by a description of a transmission probability based on scribing the pore circumference.

5.8.1 Knudsen, Smoluchowski and Dushman

In Knudsen's description of rarefied gas flow, Knudsen modeled the flow of gas in a tube of radius r , tube circumference s , length S and arbitrary cross sectional area A connecting two vessels at low pressures p_1 and p_2 .

$$J = \frac{8}{3} \left(\frac{2}{\pi}\right)^{0.5} \frac{A^2}{sS} \frac{1}{(2r)^{0.5}} (p_1 - p_2) \quad (5.64)$$

for a long tube:

$$J = \frac{42\pi^{0.5}}{3} \frac{r^3}{S} \frac{1}{d^{0.5}} (p_1 - p_2) \quad (5.65)$$

and a long tube with a circular opening:

$$J = \left(\frac{\pi}{2}\right)^{0.5} \frac{r^2}{(2r)^{0.5}} (p_1 - p_2) \quad (5.66)$$

Smoluchowski [86] argued that Knudsen's expression was incorrect and that the flux through a long tube should actually be:

$$J = \frac{1}{2(2\pi)^{0.5}} \frac{A}{S} \frac{1}{d^{0.5}} (p_1 - p_2) \quad (5.67)$$

$$A = \int_s \int_{-\pi/2}^{+\pi/2} \frac{1}{2} \rho^2 \cos(\theta) d\theta ds \quad (5.68)$$

where A is the cross sectional area of the tube, ρ represents a chord of the cross sectional area which forms an angle θ normal at a volume element ds .

Dushman [24] was the first to generalize an expression that related the rarefied flow of gas through a cylinder of arbitrary length. Dushman rewrote equation (5.64) as:

$$J = \frac{(p_1 - p_2)}{w'} \quad (5.69)$$

with w' being equivalent to:

$$w' = \frac{3}{4(2\pi)^{0.5}} \frac{S(2r)^{0.5}}{r^3} \quad (5.70)$$

and rewrote (5.66) as:

$$J = \frac{(p_1 - p_2)}{w''} \quad (5.71)$$

with w'' being equivalent to:

$$w'' = \left(\frac{2}{\pi}\right)^{0.5} \frac{1}{r^2} (2r)^{0.5} \quad (5.72)$$

Dushman considered w' and w'' as a resistance to flow and that the total resistance to flow would be:

$$w = w' + w'' \quad (5.73)$$

where

$$J = \frac{p_1 - p_2}{w' + w''} \quad (5.74)$$

5.8.2 Clausing Integral

Clausing had an issue with the Knudsen description of rarefied gas flow is its limitation to geometries with high aspect ratios and he considered Dushman's expression as a "rough approximation" [18] Clausing used known kinetic expressions to generalize equation (5.45, 5.64) to the form equation (5.44), for the flow of gas in a tube of diameter $2r$ and length S connecting two vessels at low pressures. Where J is the number of molecules per second entering the second volume; Z is the incidence rate which is the number of gas molecules striking the wall per area equation (5.33), A is the cross sectional area of the tube and w is the transmission probability that a molecule entering from the left volume element reaches the right volume element without having returned to the left volume element. Clausing deduced an expression for rarefied gas flow for a tube of any length based on a rigorous solution from an integral equation which refers to geometrical probabilities [18]. For a circular tube of length S Clausing gave the following equation for w :

$$w(S) = w_{ns}(S) + \left(\frac{2}{r}\right) \int_0^S w_{es}(S-s)n(s)ds \quad (5.75)$$

where w_{ns} is the probability a molecule will not collide with a wall as it passes through the tube, $w_{es}(S-s)$ is the probability that an emitted molecule from position s in the tube exits the tube directly without a subsequent collision. $n(s)$ is

the flux density striking the wall given by the Clausius integral equation [60]:

$$n(s) = n_o\left(\frac{r}{2}\right)w_{sr}(s) + \int_0^S n(s')w_{rr}(s-s')ds' \quad (5.76)$$

where n_o is the pore mouth boundary condition, w_{sr} is the probability that a molecule upon entering the pore will strike a differential area with length that of the circumference of the pore at position s and $w_{rr}(s-s')$ is the probability that a molecule will strike a second differential area with length that of the circumference of the pore at position s' from the differential area at s .

5.8.3 Random Billiard Model

This model [37] differentiates two scales: a macroscale which describes the pore geometry and the microscale which describes the pore surface features. An assumption in this model is that the total energy, hamiltonian, between a gas particle and a wall follows a billiard ball type collision where the interaction is based on the geometry of the wall/billiard table. Figure[5.7] describes the model where a particle performs a macrocollision at some point x with velocity v_{in} and based on the microgeometry the particle performs a series of random billiard type motion and exits the microgeometry at x' with some velocity v_{out} . The probability kernel for this system is:

$$W(v_{in} \rightarrow v_{out}; x, t) \quad (5.77)$$

with v_{out} being a function of x and V_{in} .

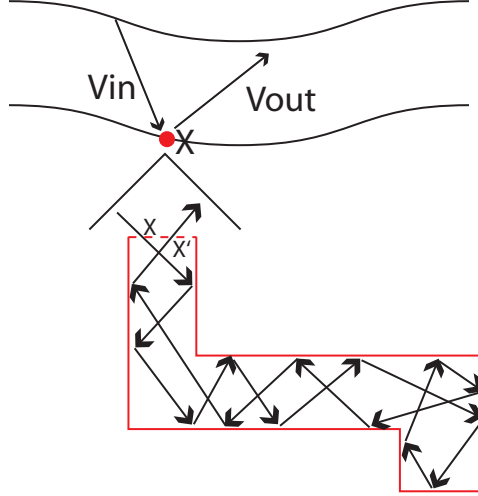


Figure 5.7: Random Billiard Description

5.8.4 KTRM

The Kinetic Transport and Reaction Model (KTRM) [42] is based on the Boltzmann transport equation to solve for the probability of finding a molecule of a specific specie with some velocity, v , at some time t at some position s with in an area ds . This probability is the kinetic density $f_i(s, v, t)$. The dimensionless transport equation in terms of the kinetic density can be written as:

$$\frac{\partial f_i}{\partial t} + v \cdot \nabla f_i = \frac{1}{Kn} Q_i(f) \quad (5.78)$$

where Q_i is the collision operator typically the KTRM is used to model transient conditions at the equipment scale.

5.8.5 BTRM

The ballistic transport and reaction model (BTRM) [94, 13] has been used to model deposition processes at steady state. The model follows the Clausing

integral equation where the total flux of a species arriving at some local position s is equivalent to the flux of molecules entering the flow system and the flux of molecules arriving from a scattered source, s' and from species being generated. Overall the expression can be written as:

$$\eta^{a,t}(s) = \eta^{a,1}(s) + \int_0^r q(s, s')[\eta^{a,t}(s') + R] \quad (5.79)$$

where $q(s, s')$ is the differential probability for a molecule leaving position s to arrive at s' . The transmission probability contains the geometric information needed to solve the transport part of the BTRM where $q(s, s')$ can be calculated using figure (5.4) where your arrival location, s is point B and your re-emission source, s' is point A . The transmission probability then becomes:

$$q(s, s') = q(A, B) = -\frac{\cos(\theta_A)\cos(\theta_B)}{||L||^2} \quad (5.80)$$

5.8.6 Novel Approach for Determining Transmission Probability

If we consider a point spatially located at x in a circular cylinder a differential element around that point, a “ring“, can be established with its length equivalent to the circumference of a circle with a local radius $r(s)$. On this surface there exists a differential area dA . This differential area represents a scattering source that arrives at a differential element dA' spatially located at s' forming a ring with a length equivalent to the circumference of a circle with local radius $r(s')$ figure (5.8). However the differential element dA' is equally likely to be anywhere on the circumference of the circle between 0 and π . The vector S can be calculated:

$$\vec{S} = (r'\cos\theta - s)i + (r'\sin\theta - r)j + (z' - z)k \quad (5.81)$$

the normal vector n is determined to be:

$$\vec{n} = \frac{d\vec{S}}{dr} \quad (5.82)$$

therefore the cos of the angle ω is simply:

$$\cos(\omega) = \frac{\vec{n} \cdot \vec{S}}{||n|| ||S||} \quad (5.83)$$

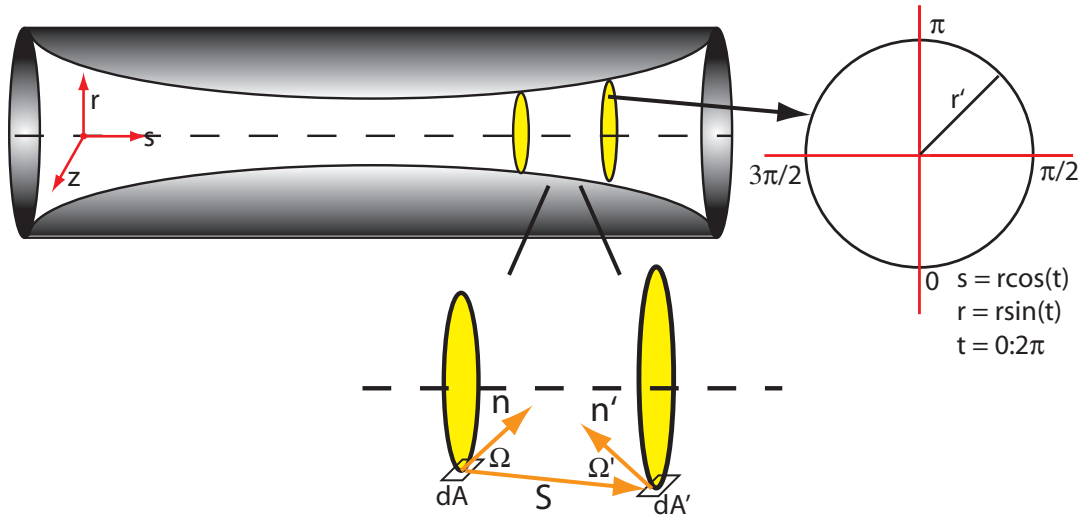


Figure 5.8: Schematic for Determining $q(s,s')$

5.9 Method of Weighted Residuals

The solution to 5.61 can be determined numerically by discretizing the ODE along the length of the pore. The method of weighted residuals (MWR) approximates the actual solution of the differential equation while maintaining the original operator [14]. The approximate solution is chosen by defining a functional form of the solution where the approximate solution is sought from a finite-dimensional

space [14], where this space is characterized by a set of basis functions. Therefore the approximate solution or trail function can be written as:

$$\tilde{\delta} = \sum_{i=1}^N a_i \phi_i(s) \quad (5.84)$$

where a_i are scalars and $\phi_i(s)$ are the set of basis functions. In MWR the problem is to determine a_i such that $\tilde{\delta}$ is a good approximation to δ . The substitution of the trail function into equation 5.61 results in the determination of the residual. The residual is solved in discrete locations within the spatial boundary conditions. There are multiple techniques within the MWR such as the sub-domain method and the Galerkin method but the method that is chosen for this work is the collocation method. In this method the discrete locations within the spatial boundary conditions are known as the interior collocation points and are determined by the roots of an N^{th} order shifted orthogonal polynomial. The collocation method attempts to minimize the residual by forcing it to pass through zero at the collocation points. The choice of the basis function should be such that the N^{th} order function is orthogonal to all lower ordered functions. Examples of the basis function include the Jacobi, Chebyshev, and Legendre polynomials. To describe the MWR processes using the collocation method we take equation 5.61 for either the TMA exposure or for the water exposure and write it as:

$$\frac{d^2\delta}{ds^2} + \frac{3}{r(s)} \frac{d\delta}{ds} - \frac{C(\delta(s))}{\beta r(s)} = 0 \quad (5.85)$$

where β is a constant equivalent to:

$$\beta = \frac{2}{3RT\pi} \left[\frac{8kT}{\pi m} \right]^{.5} \quad (5.86)$$

To determine the interior collocation points the shifted Legendre polynomial is chosen if we choose three interior collocation points the roots of the third order Legendre polynomial are: 0.1127, 0.5, and 0.8872 plus our two boundary values at 0 and 1. The three interior basis functions are:

$$\phi_0(s) = 1 \quad (5.87)$$

$$\phi_1(s) = 2s - 1 \quad (5.88)$$

$$\phi_2(s) = 6s^2 - 6s + 1 \quad (5.89)$$

the approximate solution becomes

$$\tilde{\delta} = \sum_{i=0}^2 a_i \phi_i(s) = a_0 + 2a_1s - a_1 + a_26s^2 - a_26s + a_2 \quad (5.90)$$

substituting the approximate solution into 5.61 for each interior collocation points results in a series of linear equations which can be solved by a Newton-Raphson method where the consumption term comes from the Monte Carlo simulation. The actual solution was determined by utilizing a specialized discretization toolbox [6]. The Jacobian for the Newton-Raphson method has a solution of order-N, $O(N)$, were the diagonals, the MC simulators, are the hardest to solve.

Chapter 6

Results and Conclusions

6.1 Overview

In this section we present the results of our multiscale model as related to the pore radius as a function of the spatial position. The ALD reactor type that is used in depositing aluminum oxide in anodic aluminum is a flow type reactor. As mentioned, the dynamics of the reactor exposes the substrate separately where the leading edge is exposed first and the trailing edge is exposed last. Therefore, film uniformity is a function of the saturation dose. To explore the different geometries that are possible the pore is initially discretized across the length of the pore and at each collocation point a lattice based Monte Carlo object is created. The length of the pore is one micron and the initial pore diameter across the length of the pore is at $20nm$. The pore is open in both ends where the two pore mouths are classified as the right mouth or left mouth and are open to vacuum Figure [6.1]. The initial exposure across the length of the pore is a function of the pore mouth boundary conditions, if a precursor is entering the pore from only one side the initial exposure profile is assumed to fall linearly to zero across the length of pore or if the precursor enters both ends of the pore then the initial exposure profile is assumed to be parabolic with the minima at the center of the pore set to zero. Recipes are generated for each ALD cycle giving the TMA and water exposure at each end of

the pore where the exposure is measured in one thousandths of a langmuir. The langmuir is a unit of exposure used in surface physics and has units pressure time. A system of equations based on the collocation method of weighted residuals is solved via a Newton-Raphson method to equate the exposure level at each collocation point which is translated to the total number of Monte Carlo iterations for the TMA deposition and water deposition. The result of the atomistic model produces a growth per cycle at that models collocation point which is used to upgrade that particular spatial pore radius. The simulation continues until the desired number of cycles is completed. The number of cycles that were chosen for the simulations were dictated on the fact that we did not want to close the pore mouths and thus generate a physical pore radius profile that could be measured experimentally. We

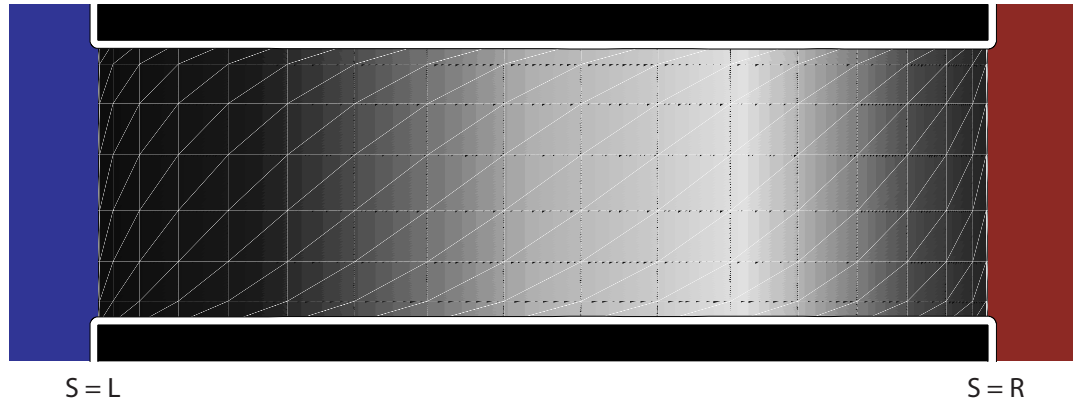


Figure 6.1: The Initial Pore

now present the results of these simulations:

6.1.1 Recipe 1

The pore mouths are exposed for 120 cycles where the right pore mouth is exposed to 3 one thousandths of a langmuir of both TMA and water. The Left side of the pore is open to vacuum. Using this recipe we see that the pore radius

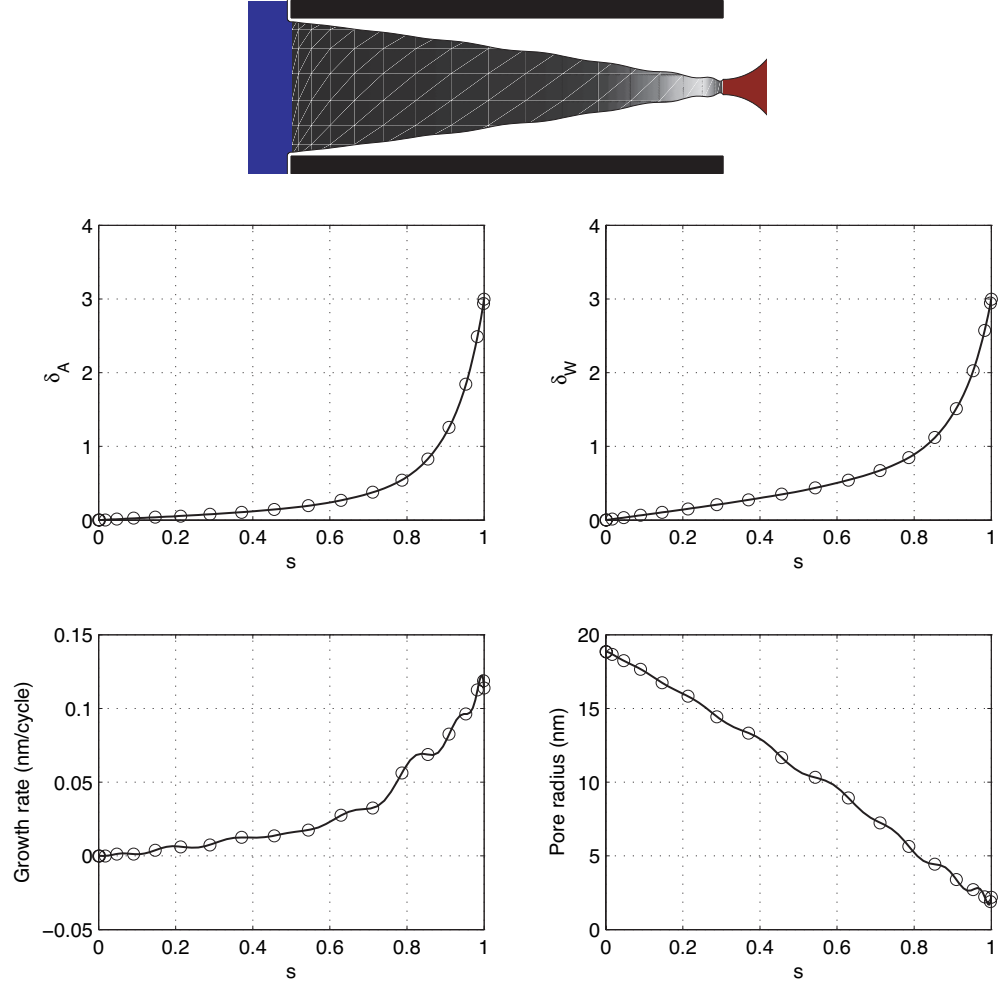


Figure 6.2: Right pore mouth exposed

figure [6.2] at the right side of the pore is nearly closed off while at the left side of the pore we see a very slight accumulation this is also seen in the growth rate across the pore where there is a high growth at the right side of the pore and it

eventually falls to zero at the left side of the pore. The exposure of TMA δ_A falls off exponentially across the pore as does the exposure of water δ_W . However water is capable of diffusing further along the pore due to its higher diffusivity. Physically the precursors are reacting first at the leading edge of the pore and as the precursor molecules react they starve the pore of precursor towards to the tail edge.

6.1.2 Recipe 2

The pore mouths are exposed for 120 cycles where the left pore mouth is exposed to 3 one thousandths of a langmuir of both TMA and water. The right side of the pore is open to vacuum. This process is the mirror opposite of the previous process. Using this recipe we see that the pore radius figure [6.3] at the left side of the pore is nearly closed off while at the right side of the pore we see a very slight accumulation this is also seen in the growth rate across the pore where there is a high growth at the left side of the pore and it eventually falls to zero at the right side of the pore. The exposure of TMA δ_A falls off exponentially across the pore as does the exposure of water δ_W . However water is capable of diffusing further along the pore due to its higher diffusivity. Physically the precursors are reacting first at the leading edge of the pore and as the precursor molecules react they starve the pore of precursor towards to the tail edge.

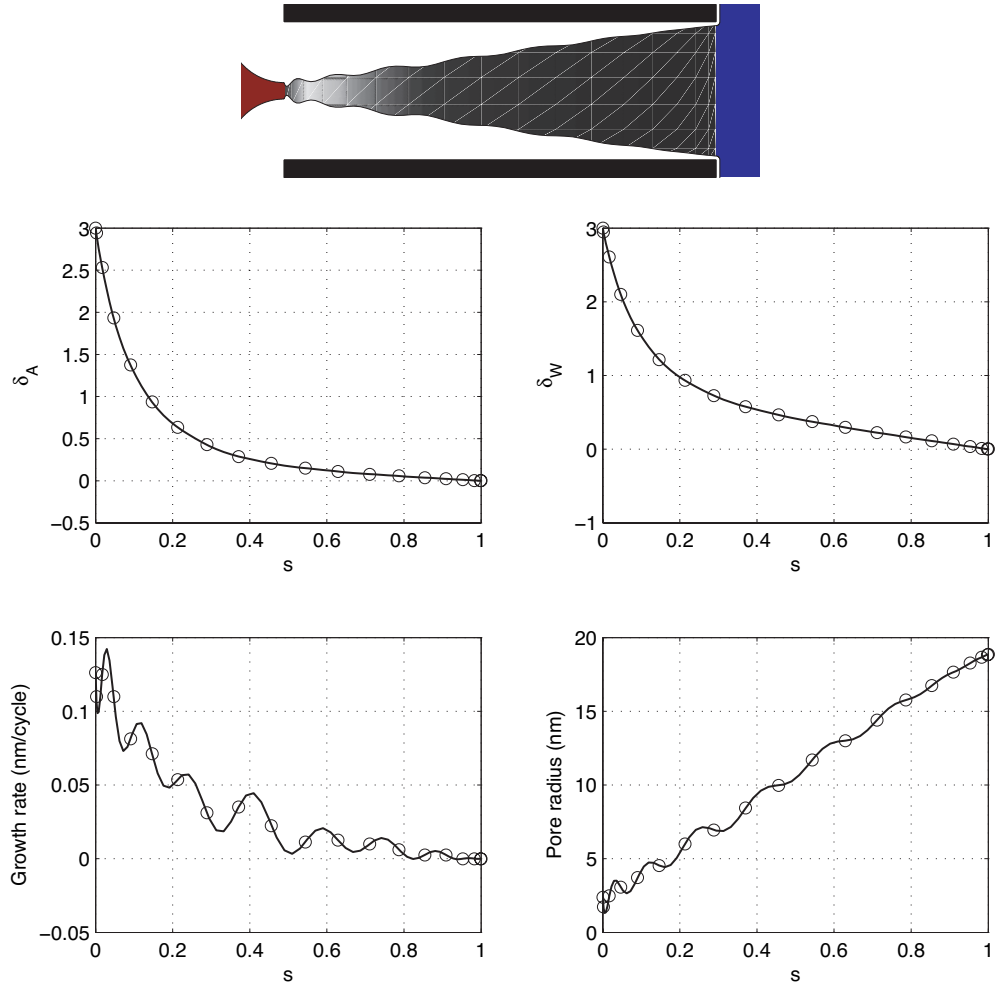


Figure 6.3: Left pore mouth exposed

6.1.3 Recipe 3

The pore mouths are exposed for 125 cycles where the left and right pore mouths are exposed to 3 one thousandths of a langmuir of both TMA and water. Using this recipe we see that the pore radius figure [6.4] profile is the addition of the

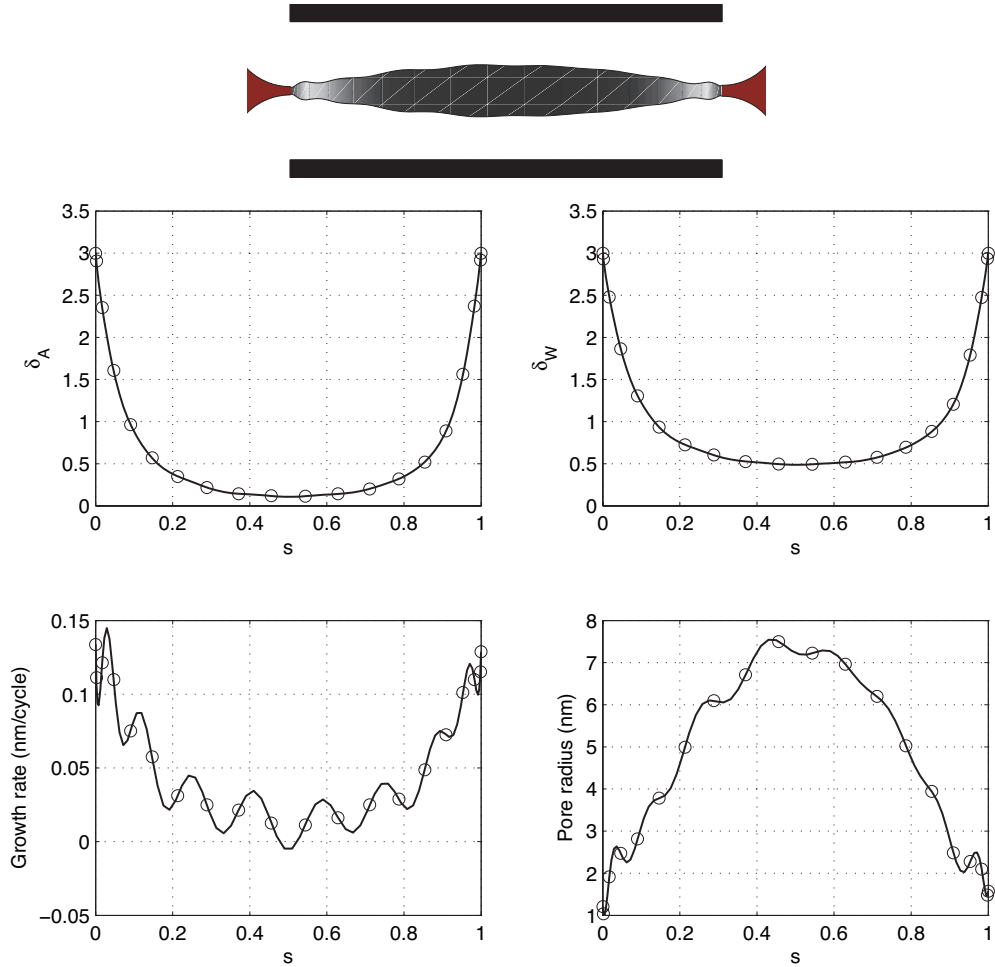


Figure 6.4: Left pore mouth exposed

results of recipe 1 and recipe 2 where both pore mouths have a very high growth rate and high precursor exposures while the center region of the pore has minimal exposure to TMA and water.

6.1.4 Recipe 4

The pore mouths are exposed for 100 cycles where the left pore mouth is exposed to 3 one thousandths of a langmuir of water and the right side of the pore mouth is exposed to 3 one thousandths of a langmuir of TMA. In this process we

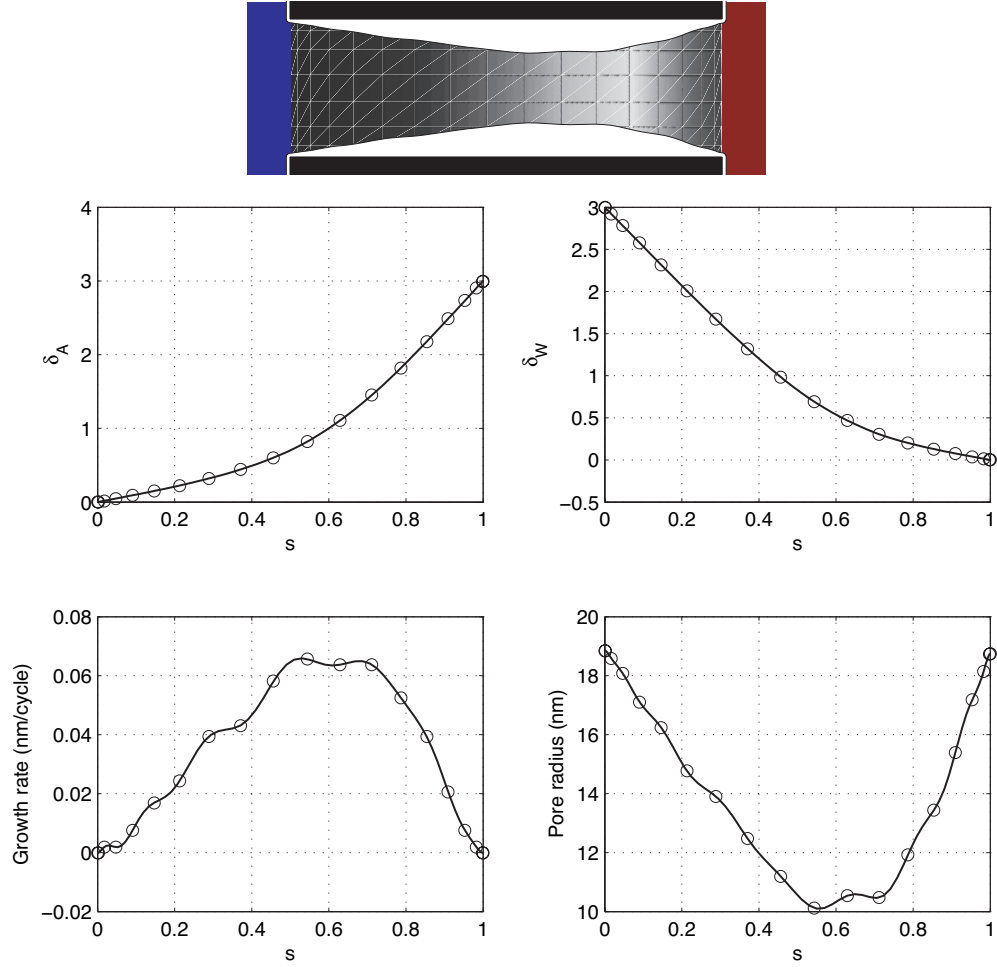


Figure 6.5: TMA exposed to right and water left

have split the precursor exposure to the opposite ends of the pore for 150 cycles. Using this recipe we see that the pore radius figure [6.5] is smaller at the center of the pore but shifted towards the right. The exposure of TMA δ_A falls off across the pore

as does the exposure of water δ_W from there pore mouths. Physically TMA reacts with a hydroxylated surface, water can diffuse further along the pore but starves the opposite end of the pore. This results in a unhydroxylated surface towards the opposite pore mouth, where TMA will be exposed to. During the TMA exposure TMA will diffuse along the length of the pore and only react once the hydroxylated surface appears. Thus the aluminum film is thicker towards the center of the mouth and non existent at the mouths.

6.1.5 Recipe 5

The pore mouths are exposed for 150 cycles where the right pore mouth is exposed to 3 one thousandths of a langmuir of TMA and the right side of the pore mouth is exposed to 3 one thousandths of a langmuir of water. This process is the mirror opposite of the previous process. In this process we have split the precursor exposure to the opposite ends of the pore 150 cycles. Using this recipe we see that the pore radius figure [6.6] is smaller at the center of the pore but shifted towards the left. The exposure of TMA δ_A falls off across the pore as does the exposure of water δ_W from there pore mouths. Physically TMA reacts with a hydroxylated surface, water can diffuse further along the pore but starves the opposite end of the pore. This results in a unhydroxylated surface towards the opposite pore mouth, where TMA will be exposed to. During the TMA exposure TMA will diffuse along the length of the pore and only react once the hydroxylated surface appears. Thus the aluminum film is thicker towards the center of the mouth and non existent at

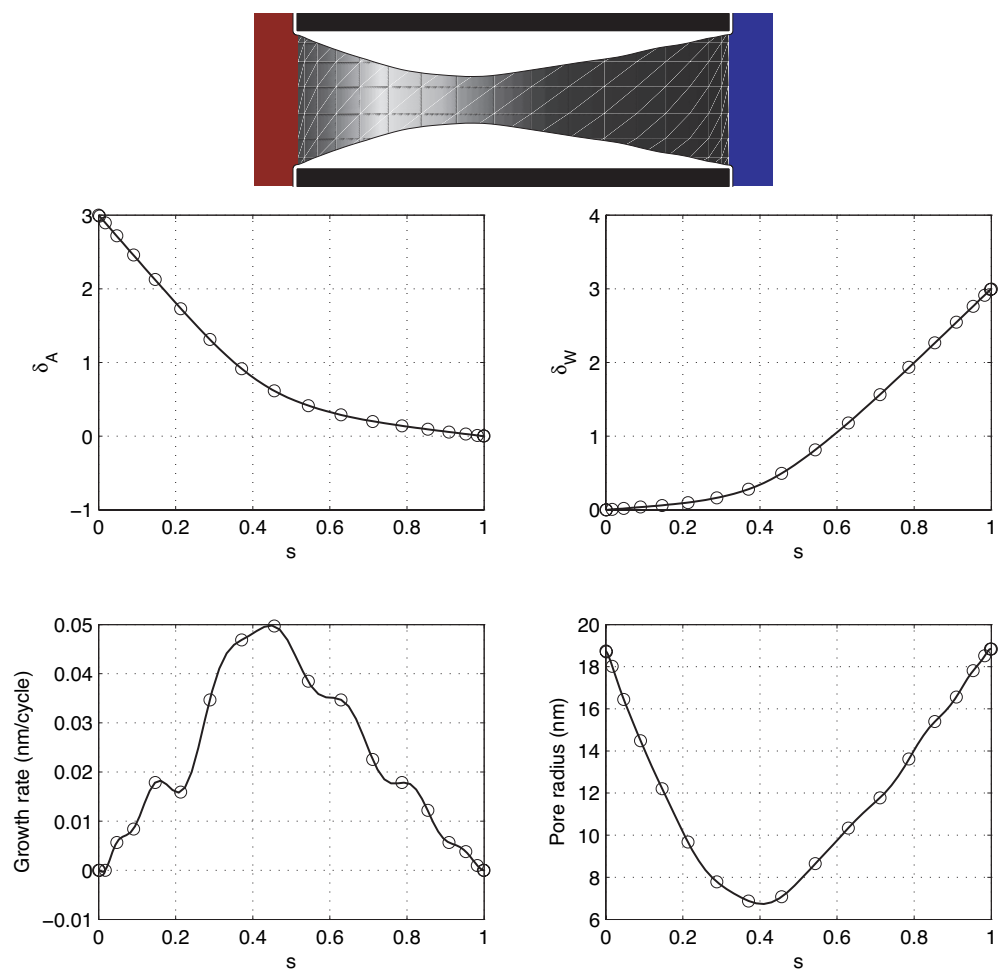


Figure 6.6: TMA exposed to right and water left

the mouths.

6.1.6 Recipe 6

The pore mouths are exposed for 300 cycles where the pore mouths are exposed to recipe 3 for 100 cycles then exposed to to recipe 1 for 100 cycles followed by 100 cycles of recipe 2. This process results in pore wall thickness being conformal between the pore mouths. Using this recipe we see that the pore radius figure [6.7]

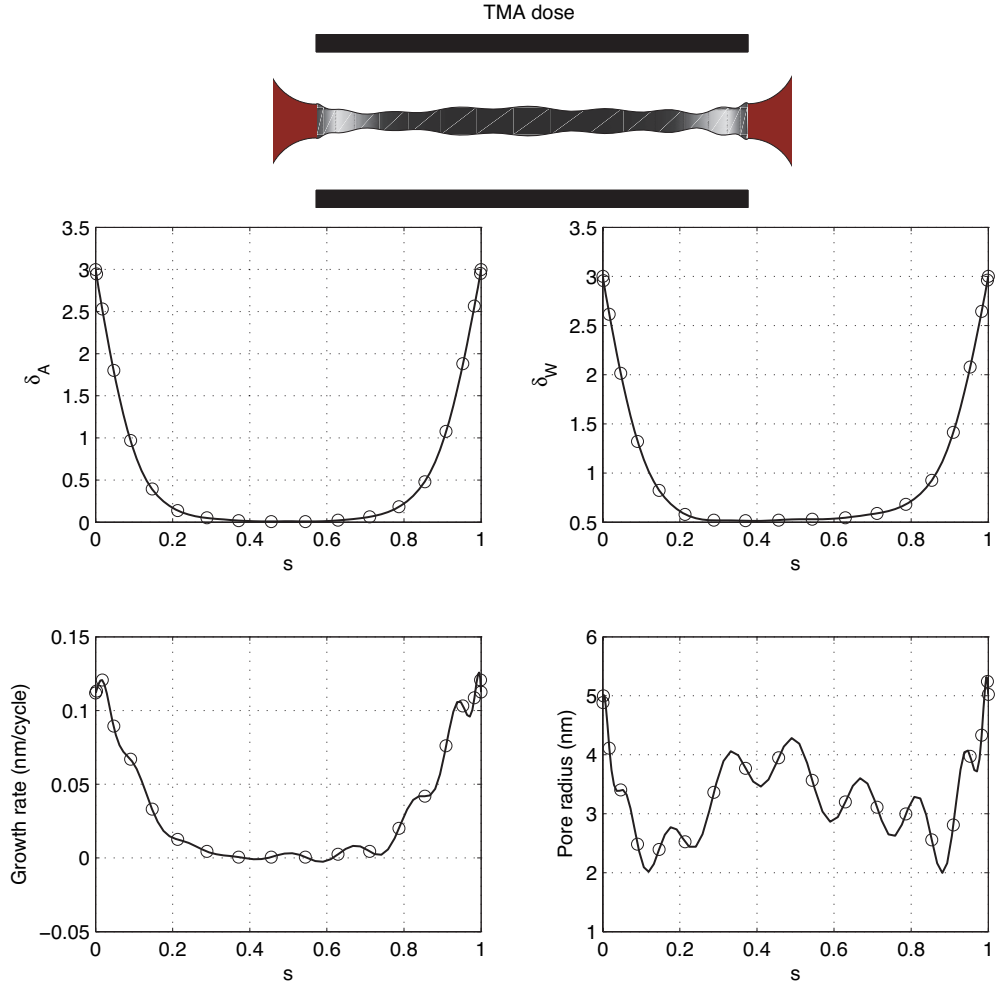


Figure 6.7: Sequential exposure

is within 2.5 and 4 nm between the pore mouths. We also see the TMA and water exposures and growth rates are also near constant. Physically the first 100 cycles the precursors are reacting first at the leading edge of the pore mouths starving the center region while during the next 200 cycles the center region gets thicker while the pore mouths remain relatively the same resulting in a high aspect ratio conformal film.

6.1.7 Collocation Points

Throughout the recipes 20 collocation points were chosen to generate solutions for the problem however it is interesting to note how changing the number of collocation points affects the physical representation of the system. The ALD recipe that was used was recipe 6 throughout the experiment with the number of collocation points tested at 5, 10, and 15 Figure [6.8, 6.9,6.10]. Based on the results of recipe 6 we would expect a conformal film with a near constant growth rate between the pore mouths however at 5 collocation points we see a parabolic growth rate. As we increase the number of collocation points our physical representation come closer to the results seen in recipe 6. This phenomenon is due to the nature of the collocation points. The points are not equally spaced but are weighted towards the end points and overall are symmetric. Thus at lower collocation points accurate physical representation is possible at the pore mouths but not at the center region of the pore. We also note at high collocation points a wave like pattern exists between the points. This pattern is due to the stochastic nature of the model more specifically to the

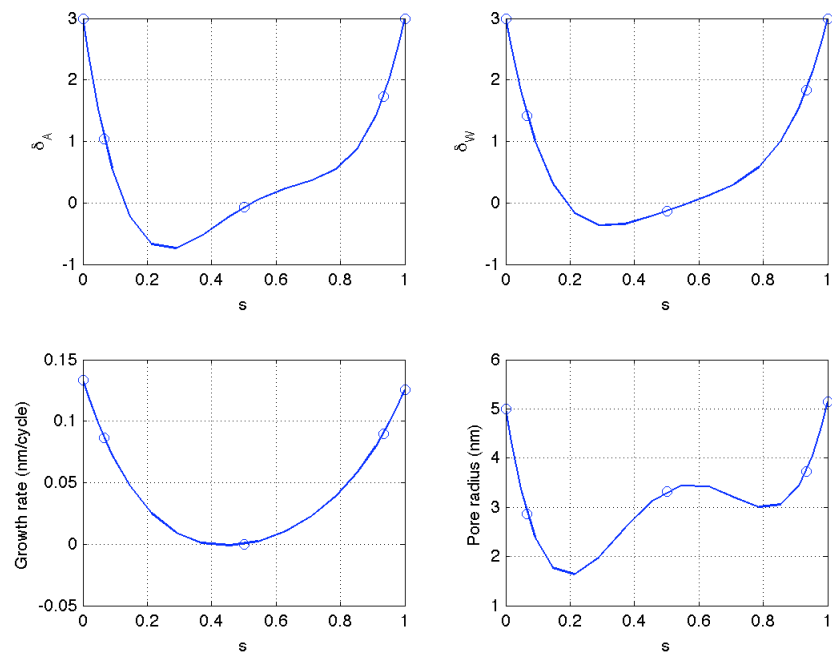


Figure 6.8: Recipe 6 at 5 collocation points

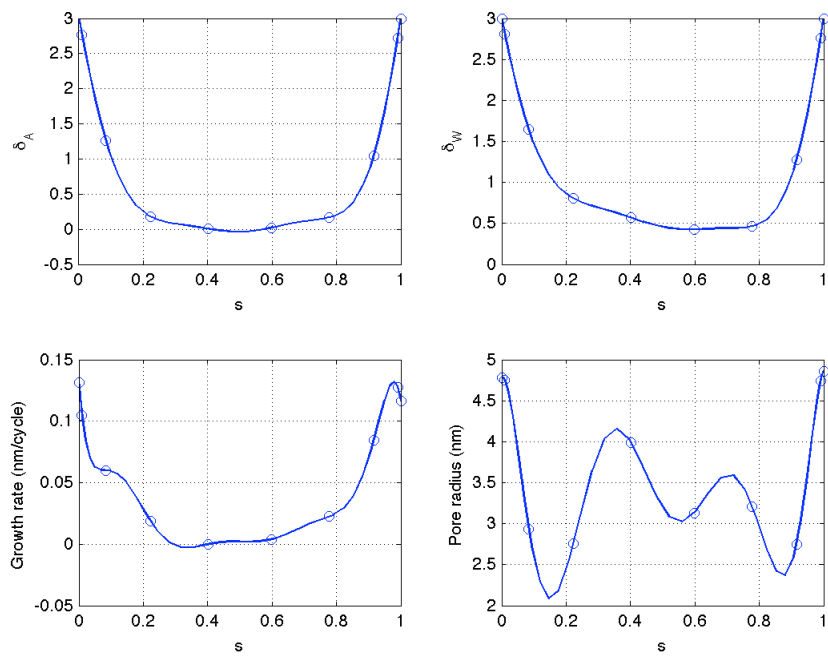


Figure 6.9: Recipe 6 at 10 collocation points

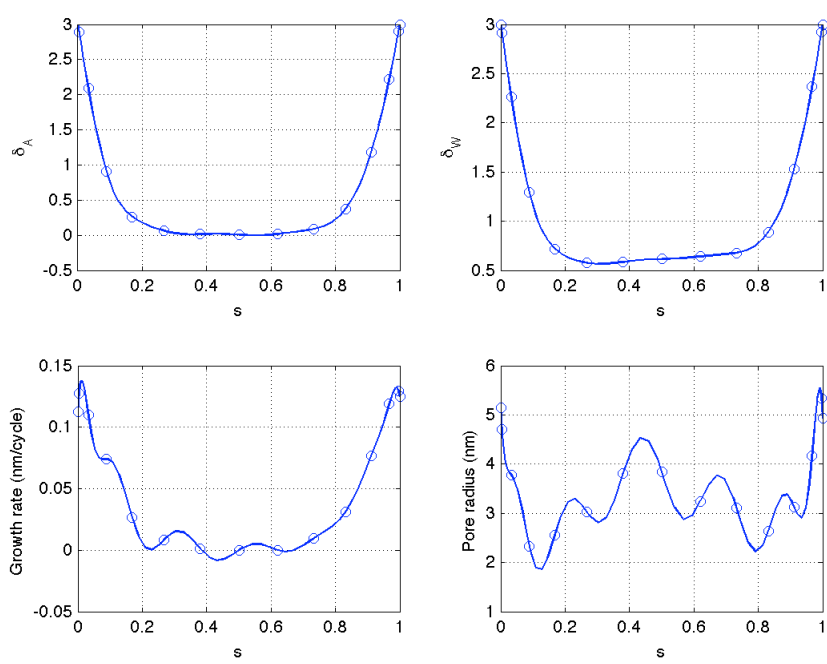


Figure 6.10: Recipe 6 at 15 collocation points

atomistic scale Monte Carlo simulation and to the fact a high order polynomial is used to fit the data. As we increase the number of collocation points the Monte Carlo objects begin to influence each other and thus a wave like patten appears. There is no physical interpretation for this wave like pattern, in order to negate the stochastic aspect of this simulation and to achieve a more physically accurate pore radius profile, multiple simulations for the same recipe are run and the average pore radius profile is computed. This was tested using recipe 3 which was run 10 times for 90 cycles at 5, 10, 20, 30 collocation points.

At 5 collocation points Figure[6.11] the curves produced after 10 simulation runs are smooth and the average profile does not deviate much from the simulated results.

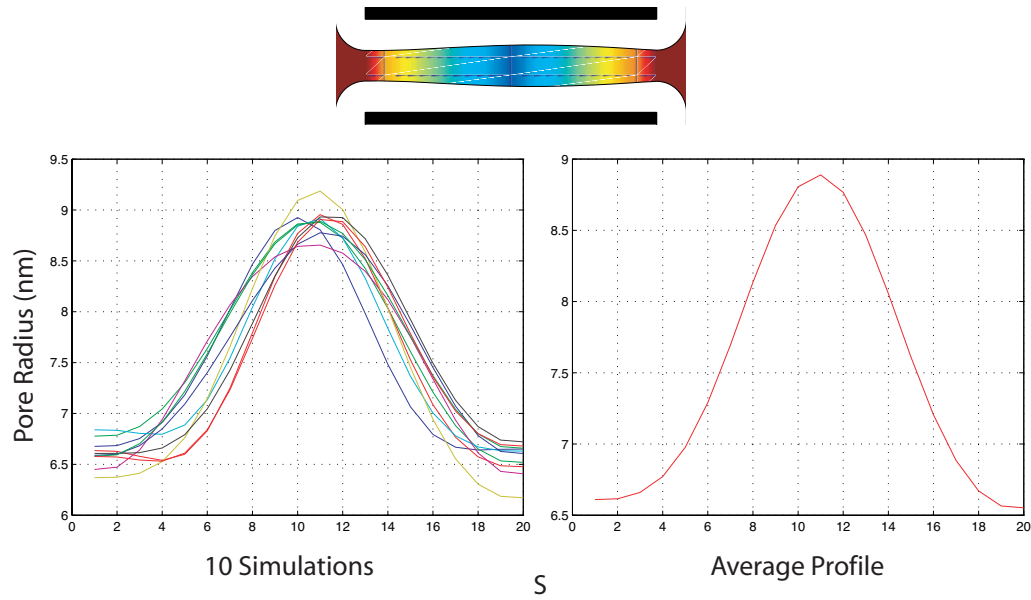


Figure 6.11: Recipe 3 at 5 collocation points and 10 runs

At 10 collocation points Figure[6.12] the curves produced after 10 simulation

runs start exhibiting the wave patterns and a smooth average profile is produced.

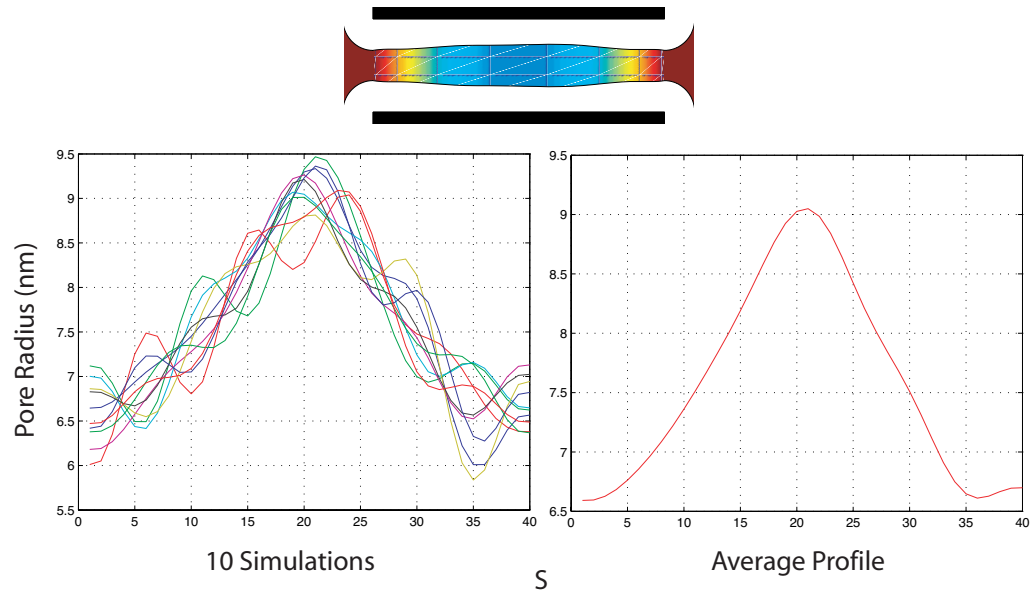


Figure 6.12: Recipe 3 at 10 collocation points and 10 runs

At 20 collocation points Figure[6.13] the curves produced after 10 simulation runs exhibit heavy wave patterns and a smooth average profile is produced.

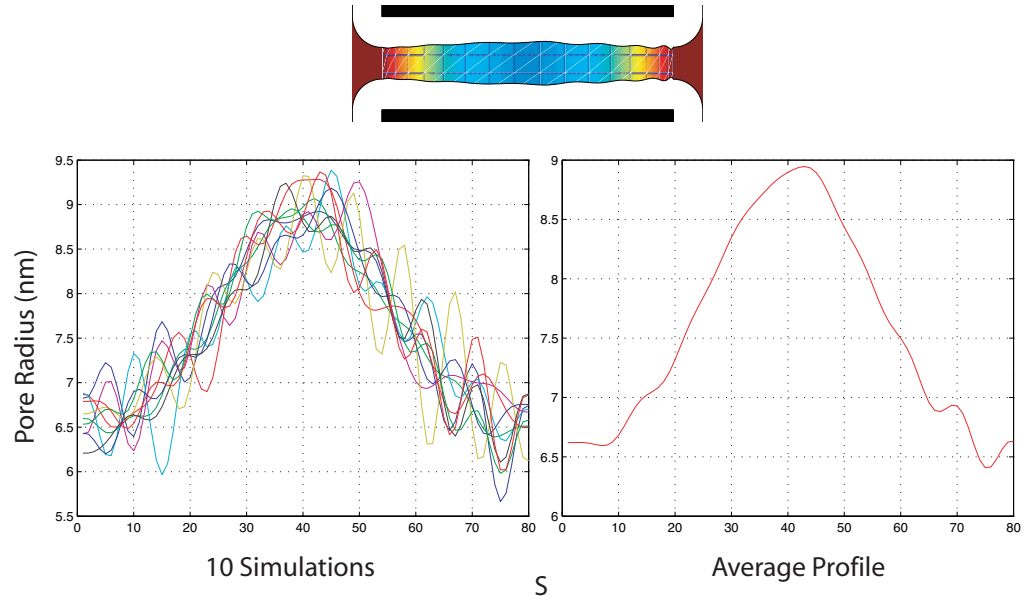


Figure 6.13: Recipe 3 at 20 collocation points and 10 runs

To negate the effects further, it can be seen Figure [6.14,6.15,6.16] that the exposure of TMA as a function of the spatial position along the pore converge to a steady state solution as you increase the number collocation points over ten runs.

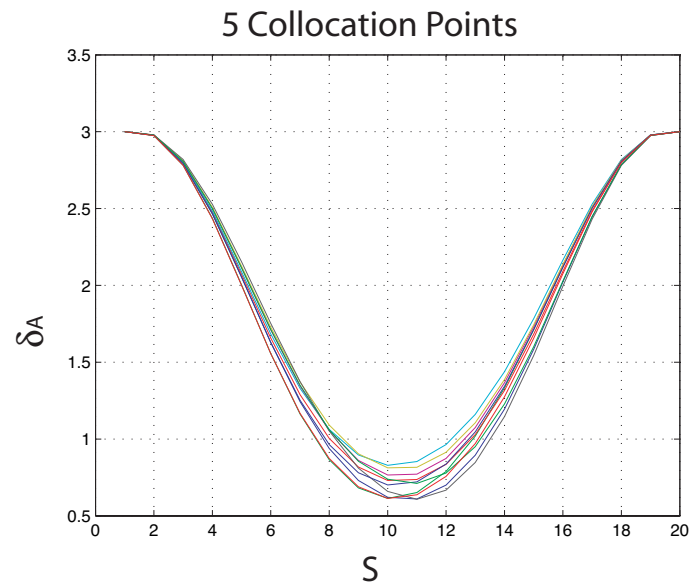


Figure 6.14: TMA exposure over 5 collocation points after 10 runs.

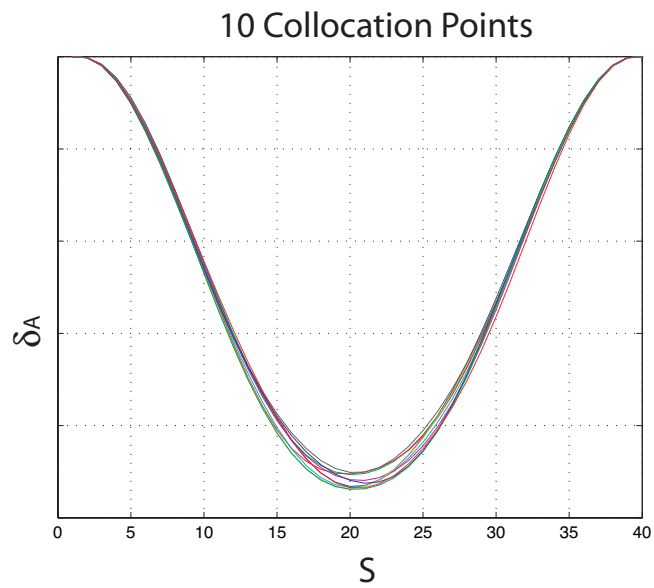


Figure 6.15: TMA exposure over 10 collocation points after 10 runs.

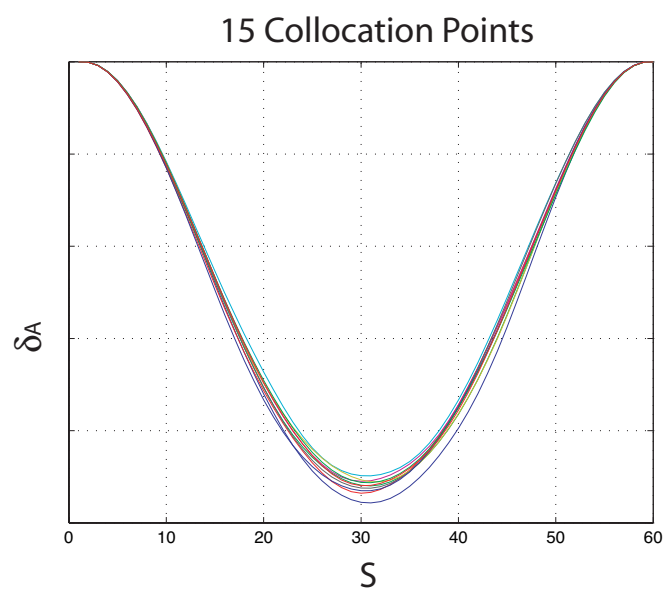


Figure 6.16: TMA exposure over 15 collocation points after 10 runs.

Chapter 7

Summery of Dissertation

Atomic Layer Deposition (ALD) is a thin film deposition process in which the growth surface is exposed to reactive precursor gases in an alternating fashion. A characteristic of the surface adsorption and reaction mechanisms is that they are normally self-limiting, allowing for atomically accurate control of lm thickness and uniform deposition over complex surface topographies.

A novel application in the use of ALD is for the control of pore diameters in high aspect ratio nanopores. Aluminum forms a porous oxide called anodic aluminum oxide (AAO) when anodized in an acidic electrolyte. The most relevant property of AAO is that the pores are very uniform in both pore length and pore diameter and are arranged in an hexagonal pattern. The pores are almost parallel and can either be open at one end or opened at both ends [20].

The use of AAO as a scaffold for the creation of nanostructured catalytic membranes (NCM) has garnered much academic research due to its advantages over typical reactor designs. The NCM combines two processes, chemical reaction and the separation of the resulting product simultaneously thus reducing the overall size of the typical catalytic reactor and the cost of operations [15]. The NCM is created by first producing a two mouth AAO where atomic layer deposition is utilized to tune the pore diameter in order to control the residence time for the reactant and

to provide filtration capabilities this is followed by the deposition of the catalytic support and the deposition of the catalyst layer. A typical NCM material map can be considered as follows: the pore size is reduced by the ALD of aluminum oxide, the catalytic support is created by the ALD of titanium oxide and the catalyst layer is formed by the ALD of vanadium oxide.

In this work a novel method to control the pore shape profile for the pore shrinking step in the AAO to NCM step is modeled where trimethyl aluminum and water precursors are used. Inherently, the ALD of AAO is characterized by a slow and a faster time scale where film growth is on the order of minutes and hours and surface reactions are near instantaneous. Likewise there are two length scales: film thickness and composition on the order of nanometers and pore length on the order of microns. The surface growth is modeled in terms of a lattice Monte Carlo simulation while the diffusion of the precursor gas along the length of the pore is modeled as a Knudsen diffusion based transport model.

In this work, A 2-dimensional lattice Monte Carlo simulation approach was developed to study the growth of ALD Al_2O_3 films and to assess the effects local growth surface structure and composition have on the surface reactions that can take place. Despite having few fitted parameters (and essentially none when operated with sufficiently large dose levels δ_A and δ_W), good qualitative and quantitative agreement was found between simulator predictions and the experimental measurements of ALD surface species dynamics during each half cycle of the ALD process [22]. Similarly, good simulator agreement was found with experimentally observed growth-per-cycle (GPC) and surface methyl ligand concentration of [77],

and measurements of film roughness and density of [71].

The surface model was coupled with a boundary value problem and solved via a Newton-Raphson method where the consumption term comes from the Monte Carlo simulation. The actual solution was determined by utilizing a specialized discretization toolbox [6]. The Jacobian for the Newton-Raphson method has a solution of order-N, $O(N)$, where the diagonals, the MC simulators, are the hardest to solve.

The pore profile was controlled by the exposure level of the precursors at the pore mouths. In the case of symmetric boundary conditions TMA and water are exposed to both pore mouths and a void remains inside the nanopore due to precursor starvation. With asymmetric boundary conditions, the exposure of TMA and water are split between the pore mouths where deposition occurs in the center of the pore and not at the mouths. This is due to the lack of reactive sites at the boundary conditions. Utilizing both types of boundary conditions a uniform film can be created by alternating between asymmetric and symmetric boundary conditions. Numerically, as the density of the collocation points increased the stochastic nature of the problem resolved itself.

Chapter 7

Future Work

Proposed research in the area of pore size control for anodic aluminum oxide nanopores include:

1. Verification of model: The modeling approach for this work can be verified experimentally by taking the output of the model based on the recipe chosen and recreate it in the lab environment. An AAO pore is exposed to the recipe and using TEM or other verification tools the pore radius profile can be determined.
2. Research different material systems to deposit inside AAO pores including the deposition of aluminum nitride (AlN) from TMA and ammonia (NH_3)
3. Modify Monte Carlo simulation to account for the curvature of a cylindrical pore where the lattice parameter based on curvature may hinder surface growth
4. Model knudsen diffusion where one pore mouth is sealed and where you have complex geometries such as the corners of the sealed mouth.
5. Research ALD as a nanomanufacturing tool where film shapes of complex structures are controlled e.g. new energy storage solutions that were recently proposed.

Bibliography

- [1] <http://www.rubloffgroup.umd.edu/>.
- [2] <http://www.indiana.edu/~hightech/fpd/papers/ELDs.html>.
- [3] http://www.anl.gov/techtransfer/pdf/Profile_AA0_07.pdf/.
- [4] <http://www.isr.umd.edu/Labs/CACSE/A-Team/mdpsas/>.
- [5] R. Adomaitis. Development of a multiscale model for an atomic layer deposition process. *Journal of Crystal Growth*, 25:115, 2010.
- [6] A.P. Alivistos. Semiconductor clusters, nanocrystals, and quantum dots. *Science*, 271:933, 1996.
- [7] L. Bardotti. Diffusion and aggregation of large antimony and gold clusters deposited on graphite. *Surface Science*, 74(367):267, 1995.
- [8] C.C. Battaile and D.J. Srolovitz. Kinetic monte carlo simulation of chemical vapor deposition. *Annu. Rev. Mater. Res*, 32:297, 2002.
- [9] F. Besenbacher and et. al. Reforming design of a surface alloy catalyst for steam. *Science*, 279:1913, 1998.
- [10] M.T. Bohr, R.S. Chau, T. Ghani, and K. Kistry. The high-k solution. *IEEE Spectrum*, 2007.
- [11] T.S. Cale, M.O. Bloomfield, and M.K. Gobbert. Two deterministic approaches to topography evolution. *Surf. Coatings. Tech.*, 201:8873, 2007.
- [12] M.A. Celia and W.G. Gray. *Numerical Methods for Differential Equations*. Prentice Hall, 1992.
- [13] C.C. Chen, J.H. Chen, and C.G. Chao. Post-treatment method of producing ordered array of anodic aluminum oxide using general purity commercial (99.7) aluminum. *Japanese Journal of Applied Physics*, 44:1529, 2005.
- [14] S. Cho, N. Walther, S. Nguyen, and J. Hupp. Anodic aluminium oxide catalytic membranes for asymmetric epoxidation. *Chem. Commun.*, page 5331, 2005.
- [15] A. Armaou Y. Lou Christofides, P. D. and A. Varshney. Control and optimization of multiscale process systems. *Birkhauser Control Engineering Series*, 42:5548, 2009.
- [16] P. Clausing. *Ann. Physik*, 4:533, 1930.

- [17] P. Clausing. The flow of highly rarefied gases through tubes of arbitrary length. *The Journal of Vacuum Science and Technology*, 8(5):636, 1971.
- [18] F.A. Cotton and G. Wilkinson. *Basic Inorganic Chemistry*, page 88. Wiley, New York, 1976.
- [19] N. Coombs D. AlMawlawi and M. Moskovits. Magnetic properties of fe deposited into anodic aluminum oxide pores as a function of particle size. *Journal of Applied Physics*, 70(8):4421, 1991.
- [20] P. Deltour, J.L. Barrat, and P. Jensen. Fast diffusion of a lennard-jones cluster on a crystalline surface. *Physical Review Letters*, 78(24):4597, 1997.
- [21] A.C. Dillon, A.W. Ott, J.D. Way, and S.M. George. Surface chemistry of al₂o₃ deposition using al(ch₃)₃ and h₂o in a binary reaction sequence. *Surface Science*, 322:230, 1995.
- [22] A.C. Dillon, M.B. Robinson, M.Y. Han, and S.M. George. *J. Electrochem. Soc.*, page 537.
- [23] S. Dushman. *Production and Measurement of High Vacuum*. J. Franklin Inst., 1922.
- [24] V. Dwivedi and R. Adomaitis. Multiscale simulation and optimization of an atomic layer deposition process in a nanoporous material. *ECS Transactions*, 25:115, 2009.
- [25] S.D. Elliot and J.C. Greer. Simulating the atomic layer deposition of alumina from first principles. *J. Mater. Chem.*, 14:3246, 2004.
- [26] D. Wu et al. *Solid State Electronics*, 49:193, 2005.
- [27] G.V. Anikeev et. al. *Inorganic Materials*, 39:1062, 2003.
- [28] J. Kim et. al. *Chem. Phys.*, 78:733, 2003.
- [29] J.S. Lee et. al. *J. Cryst. Growth*, 254:443, 2003.
- [30] L. Hiltunen et. al. *Mater. Chem. Phys.*, 28:379, 1991.
- [31] M. Ritala et. al. *J. Phys. IV*, 9:1021, 1999.
- [32] M. Titta et. al. *Mater. Res. Bull.*, 33:1315, 1998.
- [33] P.D. Ye et al. *Appl. Phys. Lett.*, 83:180, 2003.
- [34] R. Kuse et. al. *Journal of Applied Physics*, 94(10):6411, 2003.
- [35] V.E. Drozd et. al. *Appl. Surf. Sci.*, 83:591, 1994.

- [36] R. Feres and G. Yablonsky. Knudsen's cosine law and random billiards. *Chemical Engineering Science*, 59:1541, 2004.
- [37] K. Forsgren. *CVD and ALD of Group IV and V Oxides for Dielectric Applications*. PhD thesis, ACTA Universitatis Upsaliensis Uppsala, 2001.
- [38] W. Gaede. *Ann. Physik*, 41:289, 1913.
- [39] M.A. Gallivan. *Modeling and Control of Epitaxial Thin Film Growth*. PhD thesis, California Institute of Technology, 2003.
- [40] M.K. Ghosh and C.H. Choi. *Chemical Physics Letters*, 426:365, 2006.
- [41] M. Gobbert and T.S. Cale. A kinetic transport and reaction model and simulator for rarefied gas flow in the transition regime. *J. Comput. Phys.*, 213:591, 2006.
- [42] Roy G. Gordon. A kinetic model for step coverage by atomic layer deposition in narrow holes or trenches. *Chemical Vapor Deposition*, page 73.
- [43] E. Granneman, P. Fischer, D. Pierreux, H. Terhorst, and P. Zagwijn. Batch ald: Characteristics, comparison with single wafer ald, and examples. *Surf. Coatings. Tech.*, 201:8899, 2007.
- [44] R. Gupta and W.G. Willis. Nanometer spaced electrodes using selective area atomic layer deposition. *Appl. Phys. Lett.*, 90:253102, 2007.
- [45] K. Toyoda H. Kumagai and et. al. *Jpn. J. Appl. Phys., Part 1*, 32:6137, 1993.
- [46] G.S. Higashi and C.G. Fleming. *Appl. Phys. Lett.*, 55:1989, 1963.
- [47] R. Huang and A.H. Kitai. *J. Electron. Mater.*, 22:215, 1993.
- [48] A. Javey, H.Kim, M.Brink, and Date-Modified = 2010-02-17 11:45:23 -0500
Journal = Nature Mater. Pages = 241 Title = Q.Wang, Date-Added = 2010-02-17 11:44:41 -0500.
- [49] J.Elam, Z.A. Sechrist, and S.M. George. Zno/al₂o₃ nanolaminates fabricated by atomic layer deposition: growth and surface roughness measurements. *Thin Solid Films*, 414:43, 2002.
- [50] P. Jensen. Growth of nanostructures by cluster deposition. *Review of Modern Physics*, 71(5):1695, 1999.
- [51] D. Johnson. Kinetic monte carlo: Bare bones and a little flesh. Lecture Notes, 2001.
- [52] D.M. King, J.A. Spencer, X. Liang, L.F. Hakim, and A.W. Weimer. Atomic layer deposition on particles using a fluidized bed reactor with in situ mass spectrometry. *Surf. Coatings. Tech.*, 201:9163, 2007.

- [53] Charles Kittel and Herbert Kroemer. *Thermal Physics*. WH Freeman, 2nd edition, 1980.
- [54] M. Knudsen. *Ann. Physik*, 75:128, 1909.
- [55] H. Kumagai and K. Toyoda. *Appl. Surf. Sci.*, 82/83:481, 1994.
- [56] L Lecordier. *In-situ and combinatorial approaches to Atomic Layer Deposition for process and materials optimization in a cross-flow wafer-scale reactor*. PhD thesis, University of Maryland, 2008.
- [57] M. Leskela and M. Ritala. *J. Phys. IV*, (5):937.
- [58] M. Leskela and M. Ritala. Atomic layer deposition chemistry: Recent development and future challenges. *Angew. Chem. Int. Ed.*, 42:5548, 2003.
- [59] G. Levi, M. De Simon, and J.C. Helmer. Use of the clausius's equation to evaluate the pumping action of molecular gaede pumps. *Vacuum*, 46(4):357, 1995.
- [60] J.W. Lim and S.J. Yun. *Solid-State Lett.*, 7:F45, 2004.
- [61] Franz Mandl. *Statistical Physics*. Wiley, 2nd edition, 2002.
- [62] G. Mazaleyrat, A. Esteve, L. Jeloaciaca, and M. Djafari-Rouhani. A methodology for the kinetic monte carlo simulation of alumina atomic layer deposition onto silicon. *Comp. Mat. Sci.*, 33:74, 2005.
- [63] S.L. Miller. Insights into the second law of thermodynamics from anisotropic gas-surface interactions. *Found. Phys.*, 37:1660, 2007.
- [64] R.A. Millikan. Coefficients of slip in gases and the law of reflection of molecules from the surfaces of solids and liquids. *The Physical Review*, 22(1), 1923.
- [65] M.C. Mitchell. *Molecular Physics*, 99:1831, 2001.
- [66] A.J. Mukopadhyay. *Physical Review B*, 73:115330, 2006.
- [67] Charles B. Musgrave and Roy G. Gordon. Precursors for atomic layer deposition of high-k dielectrics. *Future Fab International*, 18:126–128, 2005.
- [68] A.K. Myers-Beaghton and D.D. Vvedensk.
- [69] L. Niinisto. *Mater. Sci. Eng.*, page 29.
- [70] A.W. Ott. Atomic layer controlled deposition of al₂o₃ films using binary reaction sequence chemistry. *Appl. Surf. Sci.*, 107:128, 1996.
- [71] G. Oya, M. Yoshida, and Y. Sawada. Growth of ??al₂o₃ films by molecular layer epitaxy. *Appl. Phys. Lett.*, 51:1143, 1990.

- [72] M. Ritala et. al. P.I. Räsänen. *J. Mater. Chem.*, 12:1415, 2002.
- [73] M.J. Prokhorskii, A.D. Fofanov, L.A. Aleshina, and E.A. Nikitin. Structure of amorphous oxide Al_2O_3 : Results of a molecular-dynamics experiment. *Crystallography Reports*, 49:631–634, 2004.
- [74] Rikka L. Puurunen. *Applied Physics Reviews*, (121301):1–52.
- [75] R.L. Puurunen. *Appl. Surf. Sci.*, 245:6, 2005.
- [76] R.L. Puurunen. Correlation between the growth-per-cycle and the surface hydroxyl group concentration in the atomic layer deposition of aluminum oxide from trimethylaluminum and water. *Appl. Surf. Sci.*, 245:6–10, 2005.
- [77] W.E. Stewart R.B. Bird and E.N. Lightfoot. *Transport Phenomena (Revised Second Edition ed.)*. John Wiley and Sons, 2007.
- [78] M. Ritala. Advanced a.l.e processes of amorphous and polycrystalline films. *Appl. Surf. Sci.*, 112:223, 1997.
- [79] M. Ritala and et. al. *Science*, 288:319, 2000.
- [80] M. Ritala and J. Niinistö. Industrial applications of atomic layer deposition. *ECS Transactions*, 25(8):641, 2009.
- [81] C. J. Mundy S. Balasubramanian and M.L. Klein. *J. Phys. Chem. B*, 102:10136, 1998.
- [82] U. Schroeder S. Jakschik and et. al. *Thin Solid Films*, 425:216, 2003.
- [83] R.A. Serway. *College Physics*. Brooks/Cole, 2009.
- [84] K. Seshan. *Handbook of Thin-Film Deposition Processes and Techniques*. Noyes Publications, 2002.
- [85] M.V. Smoluchowski. *Ann. Physik*, 4(33):1559, 1910.
- [86] S. Sneek. Nanotechnology in northern europe. 2007.
- [87] T. Suntola and M. Simpson. *Atomic Layer Epitaxy*. Blackie, Chapman and Hall, 1990.
- [88] W. Steckelmacher. *Rep. Prog. Phys.*, 49:1083, 1986.
- [89] J.E. Sundgren. *Prog. Solid St. Chem.*, 22:237, 1993.
- [90] Suntola. Us pat. 4,058,430. Patent, 1977.
- [91] C.X. Song S.Y. Wu, L.X. Yang and W.B. Wang. *Acta Phys. -Chim. Sin.*, 22(11):1393, 2006.

- [92] M. Tomellini and M. Fanfoni. Mean field approach for describing thin film morphology: 2. adatom life time. *Journal of Physics: Condensed Mater*, 18:4219, 2006.
- [93] G.B. Raupp T.S. Cale. Free molecular transport and deposition in cylindrical feature. *J. Vac. Sci. Technol. B*, 8:649, 1990.
- [94] A.P. Baraban V.E. Drozd and et. al. *Appl. Surf. Sci.*, 82:583, 1994.
- [95] R. Vincent. A theoretical analysis and computer simulation of the growth of epitaxial films. *Proceedings of the Royal Society of London. Series A, Mathematical and Physical*, 321(1544):53, 1971.
- [96] R.G. Vranka and E.L. Amma. *Journal of the American Chemical Society*, 89:3121, 1967.
- [97] D.F. Walls. *Physical Review A*, 18(4):1622, 1978.
- [98] E.P. Wenaas. Equilibrium cosine law and scattering symmetry at the gas-surface interface. *The Journal of Chemical Physics*, 54(1):376, 1971.
- [99] Y. Widjaja and C.B. Musgrave. *Appl. Phys. Lett.*, 80(18):3304, 2002.
- [100] S. Yang W.S. Jeon and et. al. *J. Electrochem. Soc.*, 149:C306, 2002.
- [101] K.H. Sung W.T. Cho and et. al. *Korean Che. Soc.*, 24:1659, 2003.
- [102] G. Xiong, J. Elam, H. Feng, and et. al. Effect of atomic layer deposition coatings on the surface structure of anodic aluminum oxide membranes. *J. Phys. Chem. B*, 109:14059, 2005.
- [103] C.S. Park-et. al. Y. Kim, S.M. Lee. *Appl. Phys. Lett.*, 71:3604, 1997.
- [104] S.J. Yun, K. Lee, and J. Skarp. Dependence of atomic layer-deposited Al_2O_3 films characteristics on growth temperature and Al precursors of $\text{Al}(\text{CH}_3)_3$ and AlCl_3 . *J. Vac. Sci. Technol. A*, 15(6):2993–2997, 1997.